Batch Adsorber Analogue Model for Rapid Screening of Large Adsorbent Databases for Post - Combustion CO_2 capture

by

Vishal Subramanian Balashankar

A thesis submitted in partial fulfillment of the requirements for the degree of

Master of Science.

in

CHEMICAL ENGINEERING

Department of Chemical and Materials Engineering

University of Alberta

Abstract

A simplified proxy model based on a well-mixed batch adsorber for vacuum swing adsorption (VSA) based CO_2 capture from dry post-combustion flue gas is presented. A graphical representation of the model output allows for the rationalization of broad trends of process performance. The results of the simplified model are compared with a detailed VSA model that takes into account mass and heat transfer, column pressure drop and column switching, in order to understand its potential and limitations. A new classification metric to identify whether an adsorbent can produce CO_2 purity and recovery that meet current US Department of Energy (US-DOE) for post-combustion CO_2 capture and to calculate the corresponding parasitic energy is developed. The model, which can be evaluated within a few seconds, showed a classification Matthews Correlation Coefficient (MCC) of 0.77 compared to 0.39, the best offered by any traditional metric. The model was able to predict the energy consumption within 15 % accuracy of the detailed model for 83 % of the adsorbents studied. The developed metric and the correlation are then used to screen NIST/ARPA-E database to identify promising adsorbents for CO_2 capture applications. More than hundred thousand adsorbents from carbon capture materials database (CCMDB) are then screened for the high performing adsorbents using BAAM. The effects of key adsorbent characteristics on the process performance are also studied. A detailed model optimization is then conducted to validate the BAAM's predictions. The characteristics of an ideal adsorbent are then found by a parametric study using the non-linearity plot (NLP).

Keywords: CO_2 capture, vacuum swing adsorption, adsorbent screening, process optimization, simplified model.

Preface

This thesis is an original work of Vishal Subramanian Balashankar under the supervision of Dr. Arvind Rajendran.

Chapter 2 of this thesis has been submitted as V. Subramanian Balashankar, A. K. Rajagopalan, R. De Pauw, A. M. Avila, and A. Rajendran, "Analysis of a Batch Adsorber Analogue for Rapid Screening of Adsorbents for Post-Combustion CO_2 capture", *Ind. Eng. Chem. Res.* A. K. Rajagopalan, R. De Pauw and A. M. Avila developed the modeling framework and showed the potential of the model for adsorbent screening. I was responsible for validating with a detailed model, data collection, analyzing the results, building a classification tool and developing an approach to find the minimum energy consumption and screening the NIST/ARPA-E database as well as the manuscript composition. A. Rajendran was the supervisory author and was involved with the concept formation and manuscript composition.

Chapter 3 of this thesis will be submitted for publication as V. Subramanian Balashankar, and A. Rajendran, "Applications of Batch Adsorber Analogue Model for a large-scale adsorbent screening", *Ind. Eng. Chem. Res.* I was responsible for all the research and analysis pertaining to this chapter as well as the manuscript composition. A. Rajendran was the supervisory author and was involved with the concept formation and manuscript composition.

To my parents

முயற்சியும் பயிற்சியும் இருந்து விட்டால்
வானம் தொட்டு விடும் தூரம் தான்!

"With hard work and practice, the sky really is the limit!"

- Dr. M. S. Udayamurthy

Acknowledgements

I would like to first convey my sincere thanks and gratitude to Dr. Arvind Rajendran for accepting and allowing me to pursue my Master's thesis under his supervision. Arvind has been instrumental in shaping me as a researcher and always been a great support to me during the course of my graduate studies. His passion towards the research and the sound chemical engineering knowledge drive me to push myself harder and move out of my comfort zone. The interactions and discussions with him during regular individual and group meetings over the past two years helped me grow as a person. I thoroughly enjoyed working under Arvind. Thank you, Arvind for all your support and guidance.

I am sincerely thankful to Dr. Vinay Prasad and greatly appreciate the discussions that I had with him during the key stages of this project. Special thanks to Dr. Petr Nikrityuk and I very much enjoyed working under him as a teaching assistant for CHE 314: Heat Transfer course. Thanks to Dr. Ying Tsui and Kelly Maher of the Faculty of Engineering, University of Alberta. It was great working with them for the Faculty of Engineering Graduate Research Symposium.

I am greatly thankful to Dr. Anantharaman and Dr. Arunagiri who served as great mentors during my undergrad studies at NIT Trichy. Their teachings and support helped me develop a passion for chemical engineering research.

I acknowledge the funding from the National Science and Engineering Research Council (NSERC) of Canada, NSERC CREATE program in CO_2 capture, and Canada First Research Excellence Fund through the University of Alberta Future Energy systems.

Thank you to my colleagues at Laboratory for Advanced Separation Processes (LASP), Ashwin, Gokul, Nagesh, Nick, Tai, Rafael and Libardo. I thoroughly enjoyed all our conversations during coffee and lunch breaks, group meetings and glad to learn about different cultures, and greatly appreciate your guidance and support during my thesis.

Thank you to Sushmitha and Katta for being great friends and a pillar of support to me when needed, travelling through my ups and downs for the last two years in Edmonton. I am thankful to Kirubakaran, Gautam, Amritha, Harish, Sathish, Anish, Saraswathi, Ankit, Ananthan,

Rachana, Rahul, Shruthi, Rakshith, Kathic and Meenakshi for making my life at Edmonton memorable and enjoyable and making me feel at home. Thank you to my amazing friends from undergrad, Barry, Vishal, Harish, Pranav, Sivakumar, Lala, Ashwin, Gokul and Anurag for being supportive all these years. Special thanks to my "roomie" and a close friend, Rishi for serving as a great moral support to me and a source of encouragement during difficult times.

Finally, I would like to thank my amma and appa for their great support, encouragement, motivation and unbroken trust for everything that I do in my life. Special thanks to my aachi, Sudha chithi, Ramani chithapa and all my relatives for their kindness and constant support and encouragement.

Vishal SUBRAMANIAN BALASHANKAR
Edmonton 2019

Contents

List of Tables

List of Figures

List of Symbols

Roman symbols

b	adsorption equilibrium constant for high energy site [m^3 mol^{-1}]
C	fluid phase concentration [mol m^{-3}]
d	adsorption equilibrium constant for low energy site [m^3 mol^{-1}]
En	energy consumption [kWh_e tonne of CO_2 cap.$^{-1}$]
F	adsorbent figure of merit [$molkg^{-1}$ or $mol^3J^{-1}kg^{-2}$ or -]
k	adiabatic constant [-]
M	molecular weight [g mol^{-1}]
N	number of moles [mol]
P	total pressure [bar]
Pu	purity [%]
q^*	equilibrium solid phase loading [mol kg^{-1}]
Q	outlet molar flow rate [mol s^{-1}]
r	Eucledian distance of a purity-recovery point on the Pareto front from the origin
R_g	Universal gas constant [Pa m^3 mol^{-1} K^{-1}]
Re	recovery [%]
S	selectivity
t	time [s]
T	temperature [K]
ΔU	internal energy [J mol^{-1}]
v	velocity [m s^{-1}]
V	column volume [m^3]
W	vacuum pump work done [J]
WC	working capacity [mol m^{-3} or mol kg^{-1}]
w	adsorbent mas [kg]
y	mole fraction [-]

Greek symbols

α	state at the end of adsorption step [-]
β	state at the end of blowdown step [-]
δ	state at the end of evacuation step [-]
ϵ	bed voidage [-]
η	vacuum pump efficiency [%]
γ	state at the end of light product pressurization step [-]
ρ	particle density [kg m^{-3}]

Abbreviations, subscripts and superscripts

ADS	adsorption
BLO	blowdown
class	classification
detailed	detailed model
EVAC	evacuation
fluid	fluid phase
H	high
i	index of species
INT	intermediate
LPP	light product pressurization
max	maximum
min	minimum
scaled	linear regression fit energy
solid	solid phase
total	fluid phase + solid phase

Acronyms

ASU	air separation unit
BAAM	batch adsorber analogue model
CCS	carbon capture and storage
CEZ	cation exchanged zeolites
CSS	cyclic steady state
DOI	digital object identifier

FVM	finite volume method
GA	genetic Algorithm
GCMC	Grand canonical Monte Carlo
GPU	graphics processing unit
IEA	International Energy Agency
IZA-SC	International Zeolite Association - Structure Commission
IGCC	integrated gasification combined cycle
IPCC	Intergovernmental Panel for Climate Change
MCC	Matthew's correlation coefficient
MD	molecular dynamics
MOF	metal organic framework
NIST	National Institute of Standards and Technology
NLP	non-linearity plot
ODE	ordinary differential equation
PDE	partial differential equation
PPN	porous polymer network
PPM	parts per million
PSA	pressure-swing adsorption
VSA	vacuum-swing adsorption
TSA	temperature-swing adsorption
ZIF	zeolitic imidazolate frameworks

Chapter 1

Introduction

1.1 General Introduction

Our continued reliance on fossil fuels for meeting the energy demands, since the industrial revolution, has resulted in a huge increase in global greenhouse gas (GHG) emissions. Enough scientific resources now support the claim that anthropogenic CO_2 emissions are responsible for altering the climate systems and causing climate change [8–10]. Climate change is real and happening across all continents and oceans. As shown in Fig. 1.1, the increase in the global CO_2 concentration has a direct relationship with the increase in the median global surface temperature. The global CO_2 concentration remained lower than 300 parts per million (PPM) for more than hundreds of thousands of years until 1910. With the endless exploitation of fossil fuels, at present, the global CO_2 concentration stands close to 408 PPM as measured at Mauna Loa Observatory, Hawaii (NOAA-ESRL). At this rate, it is also predicted that the earth gets warmer by 0.2 °C per decade [10].

The world leaders from close to 200 countries convened in Katowice, Poland for climate change conference to chart out a landmark global climate deal in December 2018 [11]. The consensus was reached among the leaders after two weeks of intense talks and discussions on the guidelines for implementing the Paris Climate Agreement 2015. This marks an important milestone in our actions and commitments to combating climate change and global warming. It was agreed on the Paris agreement that the countries that were part of the deal would take actions to limit the temperature rise of the century below 2 °C. Also, Intergovernmental Panel on Climate Change (IPCC) recently rolled out a special report on the impacts of 1.5 °C global warming and mitigation pathways [10]. The report highlighted that to restrict the global temperature rise to 1.5 °C over pre-industrial levels, a 45% emissions reduction over 2010 levels must be achieved by 2030. This would mean that a drastic change in our energy usage is imminent.

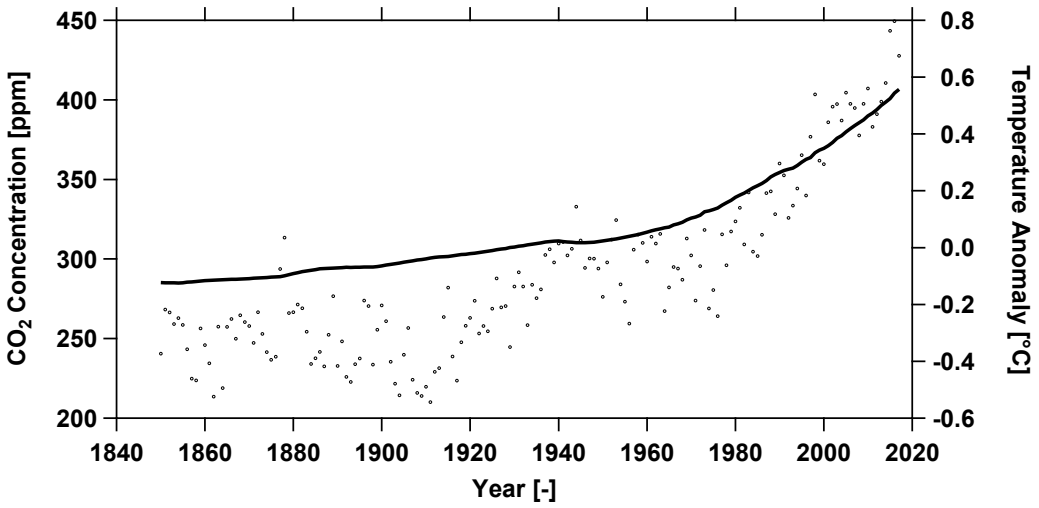

Figure 1.1: Plot showing the increase in global CO_2 concentrations ("−"), and the median global surface temperatures ("○") relative to 1961-1990 baseline average temperatures from 1850 to 2017. Source: CO_2 concentration data from 1850-1958 and 1959-2017 are obtained from the Antarctic ice core samples [4] and Mauna Lao observatory-Hawaii [5], respectively. Temperature anomaly data published by the Met Office Hadley Centre [6].

Electricity production constitutes the bulk portion of the CO_2 emitted to the atmosphere [8]. Majority of the electricity comes from the coal-fired power plants [7, 12]. Many of the advanced countries including Canada have already begun to phase out the existing coal-fired power plants in their commitment to switch to more cleaner fuels for the power generation. However, it puts forth an immense challenge in meeting our immediate energy requirements without having to use fossil fuels for producing electricity. In this regard, carbon capture and sequestration (CCS) provides an imperative solution which allows the continued use of fossil fuels without affecting the atmosphere. In CCS, the CO_2 from the large point sources is concentrated, compressed and transported to the CO_2 storage sites where it is sequestered permanently in deep aquifers. The studies from the International Energy Agency (IEA) [13] and IPCC [10] indicate clearly that the large-scale deployment of CCS is vital for meeting the Paris climate targets. CCS allows the sustainable use of coal for the power generation thereby serving as a clean source of energy.

The Global CCS institute recently came up with a comprehensive report on the global status of CCS for the year 2018 [14]. According to the report, there are 23 large-scale CCS facilities in operation or under construction with 28 pilot and demonstration-scale facilities across the world. These projects accounted for capturing close to 43 MtPa of CO_2. SaskPower's Boundary Dam 3 CCS Facility (BD3) is the world's first large-scale post-combustion carbon capture power plant located in Estevan, Saskatchewan. This facility recently reached the record milestone of capturing two - million tonnes of CO_2 in March, 2018 [15]. With Houston commencing the

world's large-scale operation of post-combustion CO_2 capture Petra Nova facility in January 2017, we see the acceptance of carbon capture technology is slowly but steadily increasing with people realizing the benefits of CCS [14]. These are the instances of carbon capture applied to the coal fired power plants. Shell Quest Carbon Capture and Storage is an example of industrial CCS which captured and stored more than two million tonnes of CO_2 [16].

1.2 Carbon capture from coal-fired power plants

In coal-fired power plants, the pulverized coal is burnt at high temperatures and pressures to produce steam which drives the turbine to produce electricity. As illustrated in Fig. 1.2, there are four technological-pathways in which CO_2 capture can be implemented in the coal-fired power plants. The post-combustion CO_2 capture is the simplest of all and it carries an advantage that it can be retrofitted to the existing power plant without much modifications to the design of the power plant. The flue gas stream coming from the power plant contains 12 to 15 % of CO_2 at the atmospheric pressure with temperatures around 40 °C. In post-combustion CO_2 capture, CO_2 is selectively removed from the flue gas and the captured CO_2 is sequestered underground or used for other applications.

The pre-combustion carbon capture works on the principle of converting coal to the "synthesis-gas" in the gasifier and further application of water - gas shift reaction to produce CO_2 and H_2. CO_2 is then captured in the CO_2 capture unit and H_2 is combusted to produce electricity. This is implemented as an integrated gasification combined cycle (IGCC) in the power plants. Unlike the flue gas stream coming from the post-combustion unit, the feed stream after the water-gas shift reaction is relatively concentrated with CO_2 (35-55%) with pressures more than 20 bar and temperatures ranging from 200 °C to 300 °C. This mode of carbon capture needs to be accounted for during the design and construction of the power plants. And, it is more expensive when compared to post-combustion. In oxyfuel-combustion, the purity oxygen, obtained from the cryogenic air separation unit (ASU), is used for the combustion of coal. Due to the introduction of high pure oxygen in the boiler, the combustion product is majorly CO_2 and is directly compressed and stored underground. This type of technology is still in the demonstration stages. However, there is a higher energy penalty associated with separating O_2 from the air. The underlying idea behind the chemical looping combustion is to avoid the mixing of N_2 with the combustion products. The oxygen is separated from the air in the oxidising reactor by reacting the metal with O_2. The oxygen is then supplied as the metal oxides to the reactor which reacts and forms H_2O and CO_2.

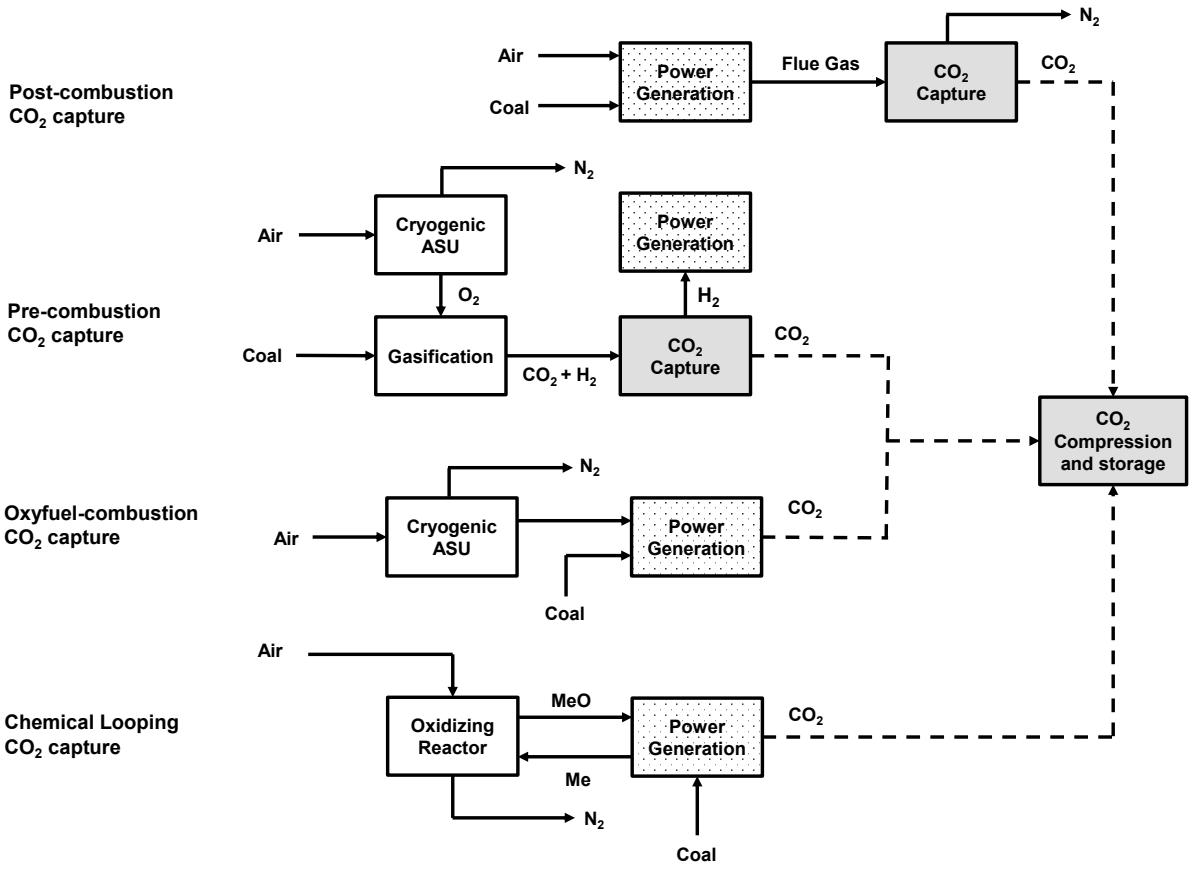

Figure 1.2: Schematic diagaram of different modes of capturing CO_2 [7].

In all of the modes of CO_2 capture systems described above, a gas separation in one form or the other exists: CO_2 from CO_2/N_2 in the flue gas (post-combustion), CO_2 from CO_2/H_2 (pre-combustion), and O_2 from air (oxyfuel combustion and chemical looping). The widely used separation technique for the post-combustion CO_2 capture is using aqueous amine solutions viz. monoethanolamine (MEA), tertiary methyldiethanolamine [17]. This type of separation process using liquid solvents is termed as absorption. In an absorption process, the flue gas stream is sent to the absorber for scrubbing with aqueous amine solutions. The solvent physically or chemically reacts with CO_2 from the flue gas. The 'rich' solvent, which is concentrated with CO_2, is further regenerated using steam for reuse in the stripper. The aqueous solvent consists of close to 70 % of water which involves energy-intensive regeneration. Owing to some of the limitations with this technology, many alternate separation techniques are looked into. One of the most important contenders is the adsorption processes.

1.3 Adsorption based CO_2 capture

1.3.1 Introduction to Adsorption

Adsorption based separation processes work by exploiting the differences in the affinities of different components at distinct pressure levels, towards a porous sorbent [18]. The physical adsorption (or physisorption) is characterized by the week inter-molecular forces such as van der Waals and electrostatic forces between the sorbate and the sorbent whereas there is a formation of chemical bond between them in the case of chemical adsorption (or chemisorption). Most of the separation processes fall in the category of physical adsorption. The amount of gas adsorbed onto an adsorbent, at a given pressure and temperature, is given by the equilibrium isotherm curve. Adsorption is an exothermic process and the measure of the strength of bonding between a sorbent and a sorbate is given by the heat of adsorption. In desorption, the adsorbate molecules are removed from the adsorbent by changing the state variables. The adsorption and desorption processes are usually repeated in cycles for separating different gas mixtures.

1.3.2 Cyclic Adsorption Processes

When the feed containing CO_2 and N_2 is fed to a column packed with an adsorbent, CO_2 is preferentially adsorbed onto the adsorbent at the high pressure, P_{ADS} and temperature, T. This is shown as q_{ADS} in Fig. 1.3. The highly selective component CO_2 is called as heavy component, and N_2 as the lighter component. The stream coming out of the adsorption step is referred to as the raffinate product and it is majorly N_2. Once the column is completely saturated, it is regenerated by either altering the pressure or temperature. At low pressure, P_{DES} or high temperature, T_{DES}, CO_2 affinity to the adsorbent is lower and this attribute is put into use for removing CO_2 from the column by reducing the pressure from P_{ADS} to P_{DES} or increasing the temperature from T_{ADS} to T_{DES}. The former case is called as the pressure swing adsorption (PSA) process while the latter is referred to as temperature swing adsorption (TSA). If the process is cyclic between the atmospheric pressure and lower vacuums, it is called as vacuum swing adsorption (VSA) process. PSA processes have shorter cycle times, and hence have higher productivity when compare to TSA. However, in cases when CO_2 isotherm is rectangular implying that very low vacuum levels have to be applied for desorption, TSA process is preferred. Also, Inventys recently developed an innovative VeloxoTherm process for CO_2 capture application which is claimed to be 40 to 100 times faster than the conventional TSA systems. The company also claims it just takes US \$15 for capturing one tonne of CO_2 from the industrial flue gas streams [19]. There is also a combined pressure and temperature swing adsorption (P/TSA) in which both temperature and pressure changes. There are two fundamental mechanisms of

separation: equilibrium competitive adsorption and kinetic selectivity based on size exclusion. Most of the separations in CO_2 capture application is equilibrium based.

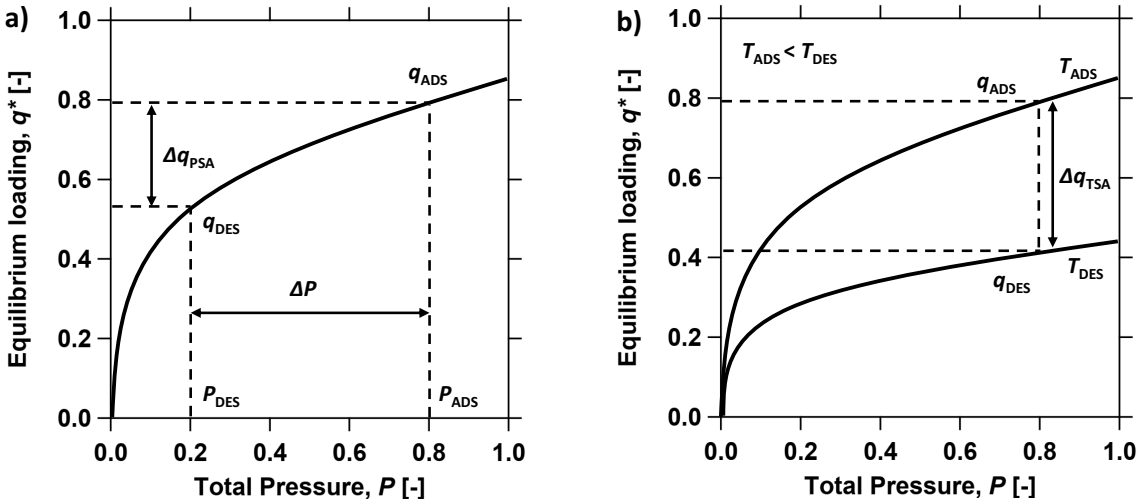

Figure 1.3: Qualitative description of a) pressure swing adsorption (PSA) process, and b) temperature swing adsorption (TSA) on an isotherm.

P/VSA is a transient dynamic process, which unlike other common mass transfer unit operations, achieve a pseudo-steady state, also referred to as a cyclic steady state (CSS). The adsorption process is said to have reached CCS when the concentration, pressure and temperature profiles across the column do not vary for a consecutive number of cycles. A typical PSA system consists of all/some of adsorption, pressurization, rinse/purge, depressurization and pressure equalization steps. The different arrangement of these steps results in a unique PSA cycle. In one end, there are simpler 3-step PSA cycles consisting of blowdown, pressurization and adsorption steps. In the other end, there are complex PSA cycles which allow more control over the movement of the adsorption and desorption fronts in the column, resulting in the desired output. Our in-house detailed model, that is used to predict the adsorption column dynamics for a given PSA cycle configuration, solves coupled partial differential equations of mass, momentum and heat balances with cyclic boundary conditions [3]. It is a non-isothermal and nonisobaric model which is robust and rigorous. The set of partial differential transport equations are discretised spatially and the resulting ordinary deferential equations are solved numerically using the finite volume method (FVM). This detailed model has been validated and studied with the pilot plant studies for Zeolite-13X as the adsorbent [20].

1.3.3 Criticality of Adsorbent Selection

The selection of a right adsorbent is critical for an adsorption based CO_2 separation process. There are variety of materials such as zeolites, activated carbons and metal organic frameworks (MOFs) that are available for carbon capture. Following are some of the important characteristics when it comes to adsorbent selection [21, 22]:

- **CO_2 Adsorption Capacity**: CO_2 adsorption capacity is one of the important adsorbent characteristics as it governs the size of the column. Higher CO_2 adsorption capacity is usually considered desirable resulting in a smaller column with greater process performance.
- **CO_2 Selectivity**: Selectivity is the relative measure of the affinity of an adsorbent towards CO_2 over N_2. Generally higher selectivity is preferred for higher process performance.
- **Mechanical Stability**: An ideal sorbent should have high resistance to variation in pressure and temperature, vibrations and higher volumetric flow rate inside the column.
- **Inertness to Contaminants**: SO_x, NO_x, H_2O and other impurities negatively affect the CO_2 adsorption. And, it becomes vital to pretreat the flue gas for these contaminants.
- **Process Performance**: An ideal adsorbent should possess the ability to produce higher CO_2 purity & recovery with lower energy consumption when employed in a P/VSA process.

Apart from these metrics, the lower manufacturing costs, adsorption/desorption kinetics , economical operation and mild regeneration conditions are also important parameters when it comes to adsorbent selection. While the above-mentioned characteristics are for an ideal adsorbent, the recent studies have shown that the simpler metrics such as adsorption capacity, selectivity and working capacity do not really predict the process performance [2, 23]. For a post-combustion CO_2 capture process, the ability to separate CO_2 from the flue gas solely governs the choice of an adsorbent. Thus, an adsorbent is assessed primarily by its performance to deliver high CO_2 purity and recovery with lower energy consumption.

1.4 Thesis Objectives and Outline

The primary objective of this thesis is to develop a simplified-proxy model for a VSA process based post-combustion CO_2 capture and use it to screen for the high performing adsorbents from the leading material databases dedicated to adsorption based carbon capture. This thesis comes befittingly at a time when there is a phenomenal development in the metalloorganic chemistry giving rise to a huge number of real and hypothetical adsorbents thereby creating a need for computationally easier tools for rapid screening. The thesis is structured into two parts. The first part extensively deals with the development, modeling and analysis of the simplified-proxy model. The last section of the first part and the entire second part focuses on the results of analysis of screening of the adsorbents from the large material databases.

Some of the key objectives addressed in this work are:

- To simplify the overall design of an adsorption process and develop simplified metrics to compute the key process performance indicators with limited adsorbent information.
- To validate the developed model with the corresponding detailed model to understand its merits and demerits.
- To demonstrate the application of the developed model for a large-scale adsorbent screening.

Chapter 1 gives an overview of global warming while stressing on the need for CCS and introduces the different ways of capturing CO_2 in coal-fired power plants. Some of the basic concepts of adsorption and cyclic adsorption processes are also discussed.

Chapter 2 details the mathematical modeling and analysis of a batch adsorber analogue model (BAAM) for a 4-step VSA cycle with light product pressurization (LPP). This chapter begins with a literature review on the existing screening metrics for CO_2 capture application and also throwing light on where exactly BAAM sits amidst them. The extensive modeling framework of BAAM is provided along with the key assumptions. The working of BAAM is first illustrated by a set of four adsorbents and the results obtained are then compared with the detailed model studies for the validation. A parametric study is then performed using BAAM to understand the trends of key performance indicators and compared with the detailed optimization process studies. A classification model based on BAAM is developed to see if an adsorbent has the potential to satisfy US-DOE purity/recovery targets and the methods to find the parasitic energy consumption was illustrated. The potential of the model in adsorbent screening is described by screening a large experimental adsorbent database maintained by NIST. And, the chapter concludes with the merits and demerits of BAAM.

Chapter 3 presents the applications of BAAM for a large-scale adsorbent screening. The analysis and trends of key performance indicators are explored for more than hundred thousand adsorbents from the carbon capture materials database (CCMDB). This chapter also gives a study of the key adsorbent characteristics viz., selectivity and heat of adsorption in predicting the process performance. This chapter also presents the detailed model study of top candidates from the BAAM's study and also serves as a validation to BAAM's predictions. A parametric study using the non-linearity plot (NLP) is then performed to look out for the characteristics of an ideal adsorbent. The chapter concludes with the summary of the work and key findings.

Chapter 4 concludes with the summary and key findings from chapter 2 and chapter 3, and recommendations for the future work.

Chapter 2

Analysis of a Batch Adsorber Analogue for Rapid Screening of Adsorbents for Post-Combustion CO_2 Capture [1]

2.1 Introduction

Carbon capture and sequestration (CCS), wherein CO_2 emitted from the large point sources is captured, transported and sequestered underground at high pressures, is a promising technology to combat global warming [7, 12]. Coal-fired power plants constitute a major source of CO_2 emissions and hence are an obvious choice for implementing carbon capture and storage (CCS) technologies. Post-combustion carbon capture, where CO_2 is concentrated from a flue gas which consists of $\approx$ 15% CO_2 and the rest being N_2, O_2 and H_2O, carries an advantage that it can be retrofitted to existing coal-fired power plants. Absorption, using aqueous amines such as monoethanolamine (MEA), is the current technology for scrubbing CO_2 from the flue-gas at large scales [7]. However, due to some of the limitations posed by this process such as, the energy intensive solvent regeneration and the corrosive nature of the solvent, there is a need for the development of alternative technologies for CO_2 capture [24]. In this regard adsorption based CO_2 capture, that use solid sorbents, has shown potential for reducing the parasitic energy consumption [3, 24–26].

The choice of an adsorbent is critical to the design of a pressure swing adsorption (PSA),

[1] This chapter has been submitted to *Ind. Eng. Chem. Res.*

vacuum swing adsorption (VSA), or a temperature swing adsorption (TSA) process [27,28]. With significant developments being made in the organometallic chemistry, the number of adsorbents being developed has seen a dramatic growth in recent years [21, 22, 29]. Hence, it becomes a challenging task when many adsorbents such as Metal Organic Frameworks (MOFs), Zeolites and activated carbons are to be screened for the selection of the best adsorbents for the CO_2 capture process [30].

Several approaches have been suggested for adsorbent screening in the literature. Harlick and Tezel suggested the use of working capacity, which is given by the difference in equilibrium loading between feed and desorption pressures [31]. Snurr's group, in an experimental study, screened 14 MOFs based on the increasing CO_2 adsorption capacity at 0.1 bar pressure [32]. Krishna et al. ranked a group of zeolites and MOFs based on experimental breakthrough time [33]. In another study, Krishna proposed the separation potential that combines selectivity and uptake capacity as a metric for screening MOFs [34]. Lin et al. screened thousands of zeolite and zeolitic imidazolate framework structures based on the parasitic energy load imposed on the power plant using a hybrid pressure-temperature swing adsorption cycle [35]. Berger et al. developed a simplified method, for a temperature swing adsorption process, to estimate the parasitic energy and used it to screen over 4 million zeolites and zeolitic imidazolite frameworks and found few promising adsorbents with lower energy consumption [36].

Most of the above-mentioned studies use simple metrics that can be easily calculated based on adsorption isotherm measurements. On the one hand, these metrics are convenient especially when large databases of adsorbents are to be screened. On the other hand, many recent studies that compared the efficacy of these metrics with detailed process simulations have demonstrated their poor reliability [1, 2]. The alternative to these approaches is the use of detailed full-scale process simulations combined with optimization. Here, a detailed model of P/V/TSA system is considered and is optimized to evaluate the best performance that can result from using a certain adsorbent. This detailed approach has been studied by Haghpanah who compared the performance of different carbons and later with Zeolite 13X [37]. Hasan et al. combined material characterization and process optimization to screen the adsorbents based on the cost of capture and compression [38]. The group of Mazzotti employed this approach for pre-combustion CO_2 capture [39]. Snurr, and co-workers have studied these approaches for screening materials using a two-staged process [40]. Nikolaidis et al. compared the performance of Zeolite 13X and Mg-MOF-74 in an integrated two-stage P/VSA process for post-combustion CO_2 capture [41]. Rajagopalan et al. demonstrated that detailed models are more reliable compared to simple screening metrics [2]. Khurana and Farooq in a series of papers have explored this approach and concluded that process optimization is essential for a reliable screening [1, 42].

Detailed process-optimization based screening is perhaps the most reliable approach for adsor-

bent screening. However, it is rather computationally demanding and requires the development of sophisticated numerical schemes and the availability of parallel computing power [3]. There are no straightforward design methods for cyclic adsorption processes, especially when the adsorption isotherm is non-linear, and when mass and heat transfer effects play an important role. Hence, these processes have to be simulated for 100s or 1000s of cycles before this cyclic steady state performance can be calculated for a given set of operating conditions. Repeating this for 1000s of combinations of operating conditions can be computationally very expensive. Our experience indicates that running multi-objective optimization of simple VSA processes could take upto a few days on multi-core desktop workstations. Scaling such approaches for screening material databases that contain hundreds of thousands of adsorbents is indeed a daunting task. Hence, there exists a need for models that are complex enough to capture the essential dynamics of the process; while also simple enough for rapid computation.

Maring and Webley proposed a simplified model (referred in this work as MW model) for rapid screening of adsorbents [23]. In this model, a well-mixed adsorber was considered with no spatial gradients of the intensive process variables. Hence, the model equations of a PSA system, that are coupled algebraic-partial differential equations, were reduced to coupled algebraic-ordinary differential equations. Further, they also proposed an approach to arrive at a cyclic steady state without having to simulate the cycle multiple times. These two simplifications meant that the MW model can be solved rapidly (in the order of a few seconds) compared to several minutes that is required for the solution of detailed PSA models. The MW model was further used to select adsorbents and to identify the key-features of ideal adsorbents. A similar approach has been discussed by Zhao *et al.* [43]. It is important to note that the key mechanism of separation in adsorption is to change operating conditions in order to "position" the concentration fronts in the column to favor high purity and recovery. In the MW model there is no mechanism to achieve this as spatial gradients are completely eliminated. Hence the MW model will give identical results to a detailed model only under specific conditions. Although the model has been used in the literature, there has been no study that validates the MW model with the detailed process models.

The objective of the current work is to extend the MW model to a different cycle configuration and to develop a graphical design method. The model is compared with a detailed VSA model in order to understand its advantages and limitations. Then, the model is used to compare the performances of 4 adsorbents and illustrate the graphical approach of the process design. A classification model to identify whether a certain adsorbent can provide $Pu_{CO_2} \geq 95\%$ and $Re_{CO_2} \geq 90\%$, a target that is set by the US Department of Energy for CO_2 capture, is developed. Further, a simple approach to estimate the parasitic energy consumption is developed and validated. Finally, this approach is used to screen adsorbents from the NIST/ARPA-E

adsorbent database to identify the potential materials for the post-combustion CO_2 capture.

At the outset, it is important to stress that the goal of the model, both MW and the current one, is **not** to represent the dynamics of the actual VSA process. In fact, as shown by Maring and Webley and in this work, the assumptions made will not allow a suitable description. Instead, the target is to develop a "reliable proxy" that can be calibrated using detailed models in order to enable rapid evaluation of a large number of adsorbents.

2.2 Batch Adsorber Analogue Model (BAAM)

The model that is considered in this work is based on the framework developed by Maring and Webley [23] with a few modifications. In order to differentiate the two approaches, we will refer to the current model as the batch adsorber analogue model (BAAM).

2.2.1 Assumptions

A batch adsorber filled with solid adsorbents is considered for developing the model equations. The mass of the adsorbent is taken to be 1 kg, and the volume of the column needed to accommodate the adsorbent is computed based on the bed porosity and adsorbent density. The bed voidage (ϵ) is considered to be 0.37. The simplified mathematical model is based on the following assumptions:

- The column is well-mixed and homogeneous, meaning that concentration, pressure and temperature gradients, both axial and radial, are absent across the column.
- The fluid phase behaves ideally.
- Heat effects are not considered and the column is isothermal.
- There is no mass transfer resistance, i.e., the equilibrium between the gas and solid phase is instantaneous.
- The adsorbent properties and bed voidage are uniform throughout the column.

The key difference between the BAAM and MW model is the assumption of isothermality. Although heat effects are important, for a particular cycle configuration that is considered here (description given in the following section), the heat effects seem to play a lesser role in deciding the cyclic steady state performance [1]. Evidence for this comes from experimental measurements from a pilot plant containing $\approx$ 80 kg of adsorbent [20]. It was observed that during the initial periods, the bed temperatures increased by $\approx 60^\circ$ C above the feed temperature, and then

dropped to $< 10^{\circ}$ C above the feed temperature, once the system reached the cyclic steady-state. The second observation arises from detailed optimization studies that revealed that models with the assumption of isothermality yielded comparable results to those that accounted for heat effects [1]. As will be shown later, the assumption of isothermal conditions also allows for a simplified graphical representation that could aid in the easy understanding of the process. The assumption related to mass transfer resistance also deviates from reality. Real systems do have finite mass transfer rates. Although many of the systems that have been studied for post-combustion CO_2 capture separate CO_2 and N_2 on the basis of their equilibrium properties, mass transfer rates have a major impact on achievable purity/recovery and the process productivity.

2.2.2 Cycle Configuration and Mathematical Model

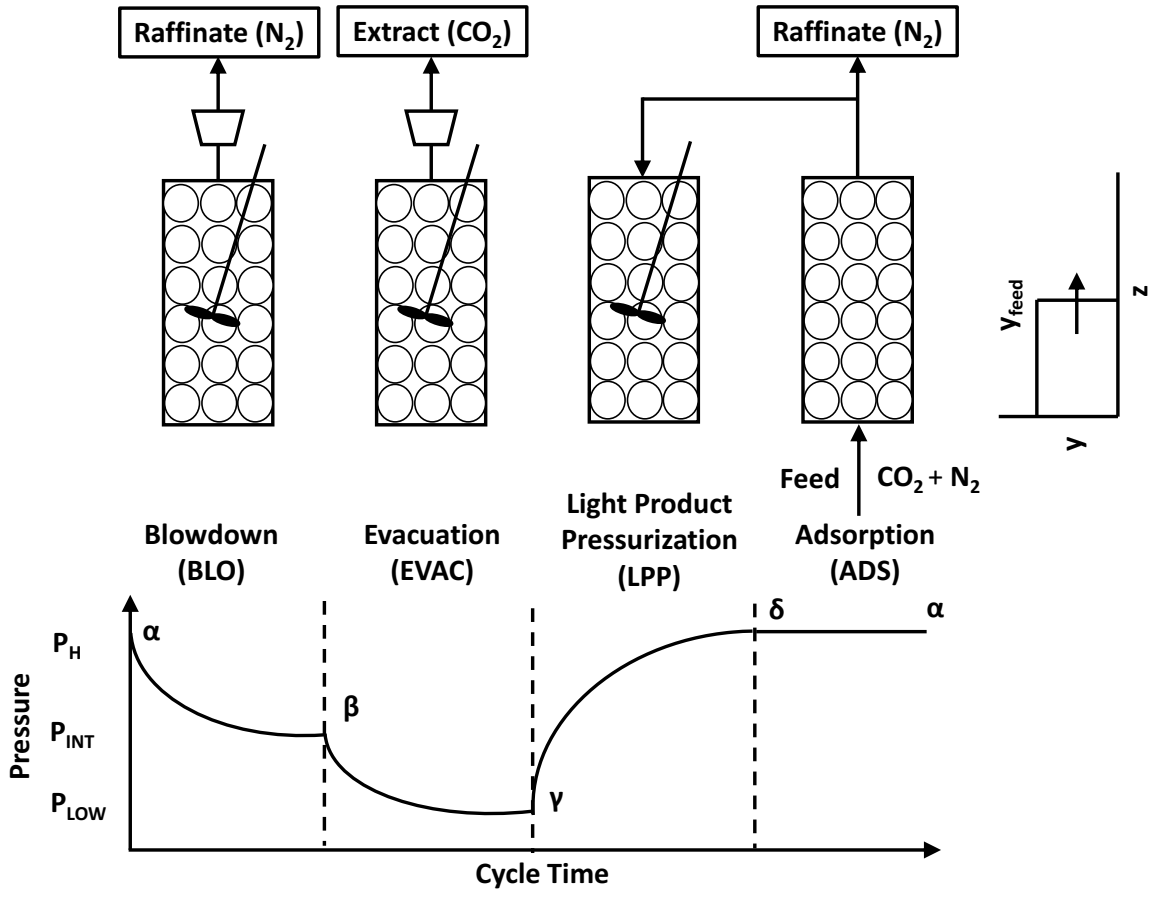

Figure 2.1: Schematic of a 4-step VSA cycle with light product pressurization (LPP).

Haghpanah et al. evaluated complex VSA cycles for the post-combustion CO_2 capture with Zeolite 13X as the adsorbent and the 4-step VSA cycle with light product pressurization (LPP) was

shown to be the best-performing cycle in terms of least energy consumption while guaranteeing high CO_2 purity and recovery [44]. Further, this cycle was also demonstrated experimentally at a pilot-scale to produce $94.8 \pm 1\%$ CO_2 purity and $89.7 \pm 5.6\%$ CO_2 recovery, thereby achieving US-DOE target in a single-stage [20]. The BAAM is developed for a 4-step VSA cycle with LPP which comprises adsorption, blowdown, evacuation and light product pressurization steps. The schematic of this cycle is shown in Fig. 2.1.

The total number of moles of a species 'i' in the column, $N_{i,\text{total}}$, is given by the sum of the number of moles of species 'i' in fluid phase, $N_{i,\text{fluid}}$, and in the solid phase, $N_{i,\text{solid}}$.

$$N_{i,\text{total}} = N_{i,\text{fluid}} + N_{i,\text{solid}} \tag{2.1}$$

where,

$$N_{i,\text{fluid}} = \frac{P y_i V \epsilon}{\mathrm{R_g} T} \tag{2.2}$$

$$N_{i,\text{solid}} = w q_i^* \tag{2.3}$$

In Eqs. 2.1 to 2.3, P, T and y_i are the fluid phase total pressure, temperature and fluid phase composition of species 'i' respectively, V and ϵ refer to the column volume and its voidage, $\mathrm{R_g}$ denotes the universal gas constant, w is the mass of the adsorbent and q_i^* is the equilibrium solid phase loading of species 'i' which is given by a suitable isotherm expression as below:

$$q_i^* = f(P, T, y_i) \tag{2.4}$$

Since isothermal conditions are considered, once the operating temperature is fixed, only two intensive variables P and y_i need to be specified in order to calculate the $N_{i,\text{fluid}}$ and $N_{i,\text{solid}}$. In the system studied, the feed consists of two components, CO_2 - the strongly adsorbing component and N_2 - the weakly adsorbing component. A brief description of each step of the PSA cycle is given below.

1. Blowdown (BLO) ($\alpha \rightarrow \beta$): The batch adsorber is initially saturated with the feed composition ($y_{\mathrm{CO_2}}^{\text{feed}}$) at high pressure P_H. This is referred to as state α, also illustrated in Fig. 2.1. In blowdown step, vacuum is applied to the column thereby reducing the pressure from P_H to an intermediate pressure, P_INT. The aim of this step is to remove the weakly adsorbing component (N_2) from the column, leaving the bed concentrated with strongly adsorbing component (CO_2). This step can be modeled by writing the mass balances around the batch adsorber that result in the following two ordinary differential equations (ODE).

Overall mass balance:

$$\frac{V\epsilon}{\mathrm{R_g}T}\frac{dP}{dt} + w\left(\frac{dq_{\mathrm{CO_2}}^*}{dt} + \frac{dq_{\mathrm{N_2}}^*}{dt}\right) = -Q \tag{2.5}$$

Component mass balance:

$$\frac{V\epsilon}{\mathrm{R_g}T}\frac{dPy_{\mathrm{CO_2}}}{dt} + w\frac{dq^*_{\mathrm{CO_2}}}{dt} = -Qy_{\mathrm{CO_2}} \tag{2.6}$$

where Q refers to the total molar flow rate leaving the column. The above equations can be combined to eliminate Q and t resulting in

$$\frac{dy_{\mathrm{CO_2}}}{dP} = \frac{a_1 y_{\mathrm{CO_2}} - a_2}{f_2 - f_1 y_{\mathrm{CO_2}}} \tag{2.7}$$

where

$$a_1 = \frac{V\epsilon}{\mathrm{R_g}T} + w\left(\frac{\partial q^*_{\mathrm{CO_2}}}{\partial P} + \frac{\partial q^*_{\mathrm{N_2}}}{\partial P}\right) \tag{2.8a}$$

$$a_2 = \frac{y_{\mathrm{CO_2}}V\epsilon}{\mathrm{R_g}T} + w\frac{\partial q^*_{\mathrm{CO_2}}}{\partial P} \tag{2.8b}$$

$$f_1 = w\left(\frac{\partial q^*_{\mathrm{CO_2}}}{\partial y_{\mathrm{CO_2}}} + \frac{\partial q^*_{\mathrm{N_2}}}{\partial y_{\mathrm{CO_2}}}\right) \tag{2.8c}$$

$$f_2 = \frac{PV\epsilon}{\mathrm{R_g}T} + w\frac{\partial q^*_{\mathrm{CO_2}}}{\partial y_{\mathrm{CO_2}}} \tag{2.8d}$$

The solution of the Eq. 2.7 gives the gas phase composition, $y_{\mathrm{CO_2}}$, as a function of total pressure, P. The blowdown step is carried out until P_{INT} is reached. The state of the adsorber at the intermediate pressure is labeled as β. Based on states α and β, the number of moles of CO_2 and N_2 removed from the adsorber can be easily calculated with simple mass balance equations. The adiabatic work done by the vacuum pump, that delivers the gas at 1 bar pressure, assuming a constant isentropic efficiency of $\eta = 72$ is given by

$$W_{\mathrm{BLO}} = \int_{N^{\alpha}_{\mathrm{total}}}^{N^{\beta}_{\mathrm{total}}} \frac{1}{\eta}\frac{k}{k-1}\mathrm{R_g}T\left[\left(\frac{1}{P}\right)^{\frac{k-1}{k}} - 1\right] dN \tag{2.9}$$

where k is the adiabatic constant. Note that the value of $\eta = 72$ used in this study is consistent with many theoretical calculations presented in the literature. A few experimental studies that have measured vacuum pump efficiencies at very low pressures report lower values of $\approx 30\%$ [20].

2. Evacuation (EVAC) ($\beta \rightarrow \gamma$): The evacuation step starts from state β and the adsorber is evacuated until the low pressure, P_{LOW}, is reached. The extract product (CO_2) is collected in this step. The state at the end of evacuation step is denoted by γ. The same set of mass balance equations and the work done by the vacuum pump, as described for the blowdown step

is applicable for the evacuation step for a value of pressure ranging from P_{INT} to P_{LOW}. The energy consumption for this step is provided by

$$W_{\mathrm{EVAC}} = \int_{N^{\beta}_{\mathrm{total}}}^{N^{\gamma}_{\mathrm{total}}} \frac{1}{\eta}\frac{k}{k-1}\mathrm{R_g}T\left[\left(\frac{1}{P}\right)^{\frac{k-1}{k}} - 1\right] dN \tag{2.10}$$

3. Light product pressurization (LPP) ($\gamma \rightarrow \delta$): The adsorber which is at low pressure, P_{LOW}, at the end of evacuation, needs to be raised to high pressure, P_{H}. This is achieved by pressurizing the adsorber with the raffinate product from the adsorption step. Note that the adsorption step, as will be described below, will start with the state δ, which is the end of LPP step. Hence, in the LPP step, the adsorber is pressurized using a stream whose composition is $y^{\delta}_{\mathrm{CO_2}}$. This step is assumed to not consume any power. The number of moles (N_{LPP}) needed to pressurize the column from P_{LOW} to P_{H} is calculated by solving the mass balance equations as given in Eqs. 2.11 to 2.12 where $y^{\delta}_{\mathrm{CO_2}}$ is the CO_2 composition in the column at the end of LPP step.

Overall mass balance:

$$\left(N^{\gamma}_{\mathrm{CO_2,total}} + N^{\gamma}_{\mathrm{N_2,total}}\right) + N_{\mathrm{LPP}} = \left(N^{\delta}_{\mathrm{CO_2,total}} + N^{\delta}_{\mathrm{N_2,total}}\right) \tag{2.11}$$

Component mass balance:

$$N^{\gamma}_{\mathrm{CO_2,total}} + N_{\mathrm{LPP}} y^{\delta}_{\mathrm{CO_2}} = N^{\delta}_{\mathrm{CO_2,total}} \tag{2.12}$$

In the above equations, N_{LPP} and $y^{\delta}_{\mathrm{CO_2}}$ are the unknowns which are solved based on the known initial state, γ (end of evacuation step). Note that this step is different from the MW model that considered pressurization with the feed.

4. Adsorption (ADS) ($\delta \rightarrow \alpha$): The column at the state δ represents the initial condition for the adsorption step. The feed is supplied to the column at constant high pressure P_{H} and temperature T^{feed}. This step is modelled differently compared to the other steps. Here, the adsorber is modelled as a standard adsorption column that is originally saturated with the gas as given by state δ. The feed gas is considered to flow through the column like a plug that breaks-through once the column is completely saturated with the feed. The aim here, as it was with the MW model, is to keep the mathematics of the model simple. Under these assumptions, the two mass balances are given by

Overall mass balance:

$$\left(N^{\delta}_{\mathrm{CO_2,total}} + N^{\delta}_{\mathrm{N_2,total}}\right) + N_{\mathrm{feed}} = \left(N^{\alpha}_{\mathrm{CO_2,total}} + N^{\alpha}_{\mathrm{N_2,total}}\right) + N_{\mathrm{raff}} \tag{2.13}$$

Component mass balance:

$$N^{\delta}_{\mathrm{CO_2,total}} + N_{\mathrm{feed}} y^{\mathrm{feed}}_{\mathrm{CO_2}} = N^{\alpha}_{\mathrm{CO_2,total}} + N_{\mathrm{raff}} y^{\delta}_{\mathrm{CO_2}} \tag{2.14}$$

N_{feed} and N_{raff} are calculated by solving the non-linear equations given in Eq. 2.13 and 2.14. At the end of adsorption step, the column reaches state α. Note that the energy consumption during the feed step is not calculated as its contribution is negligible [2, 3].

It is worth noting here that the sequence of steps start and return to state α (beginning of the blowdown step and end of the adsorption step), passing through states β, γ and δ. This avoids the need to repeat the calculations for multiple cycles, thereby significantly reducing the computational time. Further, once the adsorbent properties, feed pressure, composition and temperature are fixed, the model has only 2 design variables, namely, P_{INT} and P_{LOW}. Considering the simplicity of the model, the design space can be quickly scanned.

Performance indicators: CO_2 purity, recovery, energy consumption and working capacity are the performance indicators for the VSA process. Purity is the ratio of the number of moles of CO_2 obtained to the total number of moles obtained in the evacuation step.

$$\text{Purity}, Pu_{\mathrm{CO_2}}\,[\%] = \left(\frac{N^{\beta}_{\mathrm{CO_2,total}} - N^{\gamma}_{\mathrm{CO_2,total}}}{N^{\beta}_{\mathrm{CO_2,total}} - N^{\gamma}_{\mathrm{CO_2,total}} + N^{\beta}_{\mathrm{N_2,total}} - N^{\gamma}_{\mathrm{N_2,total}}} \right) \times 100 \tag{2.15}$$

Recovery is defined as the ratio of total moles of CO_2 collected in the evacuation step to the number of moles of CO_2 in the feed.

$$\text{Recovery}, Re_{\mathrm{CO_2}}\,[\%] = \left(\frac{N^{\beta}_{\mathrm{CO_2,total}} - N^{\gamma}_{\mathrm{CO_2,total}}}{N_{\mathrm{feed}} y^{\mathrm{feed}}_{\mathrm{CO_2}}} \right) \times 100 \tag{2.16}$$

The total-energy consumption is the sum of work done by the vacuum pump in blowdown and evacuation step.

$$\text{Energy}, En \left[\frac{\mathrm{kWh_e}}{\text{tonne } \mathrm{CO_2} \text{ cap.}} \right] = \frac{W_{\mathrm{BLO}} + W_{\mathrm{EVAC}}}{(N^{\beta}_{\mathrm{CO_2,total}} - N^{\gamma}_{\mathrm{CO_2,total}})\mathrm{M_{CO_2}}} \tag{2.17}$$

where $\mathrm{M_{CO_2}}$ is the molecular weight of CO_2. Note that the energy calculated here is in electrical units and hence, the units carry a subscript "e". Since the model assumes instantaneous equilibrium, i.e., a 100% efficient column, the productivity cannot be calculated. In order to obtain an estimate of the amount of adsorbent required, the working capacity can be considered. This quantity is defined as the number of moles of CO_2 from the evacuation step per m^3 of the adsorbent.

$$\text{Working capacity}, WC_{\mathrm{CO_2}} \left[\frac{\text{mol } \mathrm{CO_2}}{\mathrm{m^3} \text{ of adsorbent}} \right] = \frac{N^{\beta}_{\mathrm{CO_2,total}} - N^{\gamma}_{\mathrm{CO_2,total}}}{V(1-\epsilon)} \tag{2.18}$$

In this work, the ODE, given by Eq. 2.8, is solved in MATLAB R2017a using *ode15s* solver with an initial condition of $y_i = y_{CO_2}^{feed}$ at $P = P_H$ with $\Delta P = 0.001$. The coupled non-linear mass balance equations in the LPP and ADS steps, given by Eqs. 2.11 to 2.14, are solved using *fsolve* solver with trust-region-dogleg algorithm. All the simulations reported in this work are computed using the desktop computer with INTEL Core 2.80 GHz processor and 8.00 G B of RAM.

2.2.3 Detailed Model and Process Optimization

The detailed model, that is used to predict the adsorption column dynamics for a given PSA cycle configuration, solves coupled partial differential equations of mass, momentum and heat balances with cyclic boundary conditions [3]. The detailed mathematical equations, corresponding boundary conditions and the simulation parameters are given in the Appendix A. It is a non-isothermal and non-isobaric model which is robust and rigorous. The set of partial differential equations are discretized spatially using a finite volume technique and the resulting ODEs are solved using an inbuilt MATLAB ODE solver. The detailed model has been validated against lab-scale [45] and pilot-scale [20] experimental results.

For the optimization of the VSA process, a genetic-algorithm (GA) that works in conjunction with the detailed model is used. The GA chooses the set of decision variables typically the duration of the various steps, velocity of the feed and pressure levels P_{INT} and P_{LOW} and passes them to the VSA simulator. The dynamics of the process under these conditions is evaluated and the performance at cyclic steady-state conditions is evaluated and returned to the GA. The GA proceeds from one generation to the next by improving the objective functions until no further improvement is possible. Multi-objective optimization problems result in Pareto curves that provide the best trade-off between the various objective functions. Details of this approach have been discussed elsewhere [3].

2.3 Illustration and Validation of the BAAM

In this section, the developed BAAM is illustrated using four adsorbents that have been studied in a previous work [2]. The high pressure, P_{H} is fixed at 1 bar for all the simulations since it has been shown that increasing the adsorption pressure more than 1 bar has a significant effect on the overall energy consumption as the feed, which consists majorly of N_2, has to be compressed to higher pressure [3, 23]. The lower bound of P_{LOW} in this study is set to 0.03 bar, a pressure that was achieved in pilot plant experiments [20]. Due to the isothermal operation of the column, the temperature is taken to be the feed temperature of 298.15 K. Thus, the BAAM cycling between atmospheric pressure and low vacuum pressures at a fixed feed temperature of 298.15 K, is considered for all the simulations. The feed gas stream is considered to be consisting of 15 mol % of CO_2 and 85 mol % N_2 at 1 bar and 298.15 K. In this work, the flue gas is considered to be pre-dried. It is important to highlight that drying of the flue gas is indeed energy intensive and any comparisons to other processes should be made with caution [46].

2.3.1 Process Description

The four adsorbents considered in this study for illustrating the features of the model are two metal-organic frameworks (MOFs), namely, Mg-MOF-74 and UTSA-16, Zeolite 13X, and a variety of coconut-shell activated carbon (CS-AC). The properties of these adsorbents have been given in the previous publication [2].

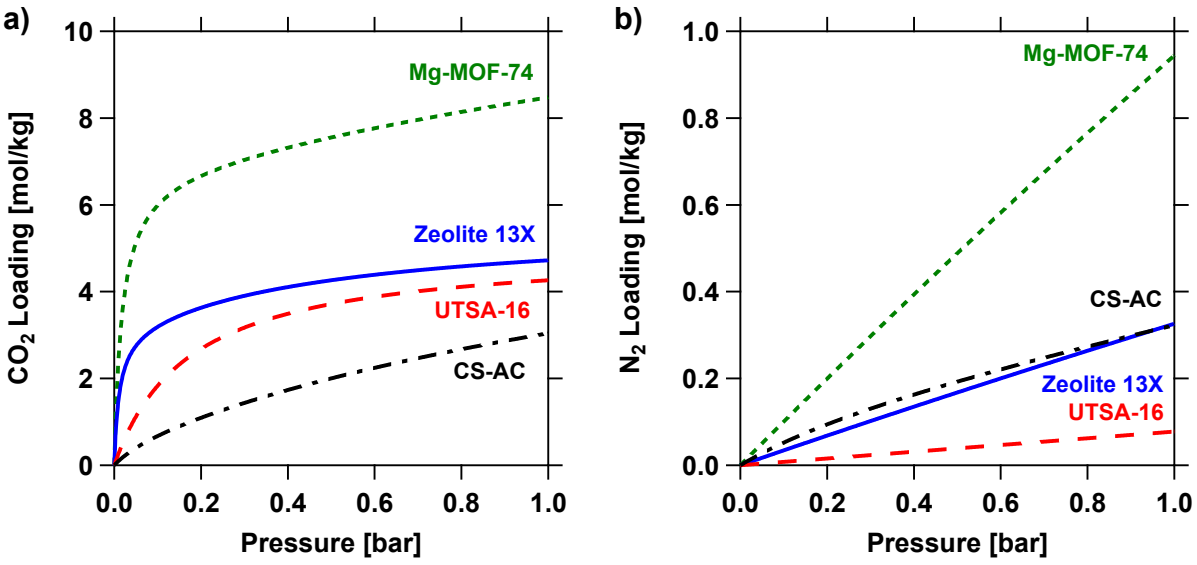

Figure 2.2: Pure component isotherms of a) CO_2 and b) N_2 at 298.15 K for the four adsorbents studied [Reproduced from Rajagopalan et al. [2]].

Table 2.1: Dual-site Langmuir pure-component isotherm parameters of CO_2 and N_2 on the adsorbents considered [2].

Adsorbent	Particle Density [kg/m^3]	Adsorbate	$q_{\mathrm{sb,i}}$ [mol/kg]	$q_{\mathrm{sd,i}}$ [mol/kg]	$b_{0,\mathrm{i}}$ [m^3/mol]	$d_{0,\mathrm{i}}$ [m^3/mol]	$-\Delta U_{\mathrm{b,i}}$ [kJ/mol]	$-\Delta U_{\mathrm{d,i}}$ [kJ/mol]
Mg-MOF-74	588.25	CO_2	6.80	9.90	1.81×10^{-07}	1.06×10^{-06}	39.30	21.20
		N_2	14.00	–	3.45×10^{-06}	–	15.50	–
Zeolite 13X	1130.00	CO_2	3.09	2.54	8.65×10^{-07}	2.63×10^{-08}	36.60	35.70
		N_2	5.84	–	2.50×10^{-06}	–	15.80	–
UTSA-16	1092.00	CO_2	5.00	3.00	6.24×10^{-07}	1.87×10^{-23}	30.60	44.70
		N_2	12.70	–	2.96×10^{-06}	–	9.77	–
CS-AC	799.50	CO_2	0.59	7.51	9.40×10^{-06}	1.04×10^{-05}	25.61	17.55
		N_2	0.16	41.30	1.81×10^{-03}	1.72×10^{-12}	8.67	44.90

The isotherms of CO_2 and N_2 were described using a dual-site Langmuir (DSL) isotherm model:

$$q_i^* = \frac{q_{\mathrm{sb},i} b_i C_i}{1 + b_i C_i} + \frac{q_{\mathrm{sd},i} d_i C_i}{1 + d_i C_i} \tag{2.19}$$

$$b_i = b_{0,i} e^{-\Delta U_{\mathrm{b},i}/\mathrm{R_g}T} \tag{2.19a}$$

$$d_i = d_{0,i} e^{-\Delta U_{\mathrm{d},i}/\mathrm{R_g}T} \tag{2.19b}$$

where q_i^* is the equilibrium solid phase loading corresponding to a fluid-phase concentration of C_i. The constants $q_{\mathrm{sb},i}$, $q_{\mathrm{sd},i}$, b_i and d_i are the equilibrium saturation solid phase loadings and affinity parameters corresponding to the sites 'b' and 'd', respectively. The constants $b_{0,i}$ and $d_{0,i}$ are the pre-exponential factors, $\Delta U_{\mathrm{b},i}$ and $\Delta U_{\mathrm{d},i}$ are the internal energies. Note that 'b' and 'd' refer to the high and low energy sites, respectively. The single component isotherms of CO_2 and N_2 on Mg-MOF-74, Zeolite 13X, UTSA-16 and CS-AC are depicted in Fig. 2.2, and the dual-site Langmuir isotherm parameters that are used to fit the adsorption equilibrium measurements of the same are given in Table 2.1. Note Mg-MOF-74 has the highest CO_2 and N_2 capacity and affinities compared to the other three materials. Zeolite 13X has the next strongest CO_2 affinity. UTSA-16 has a moderate CO_2 affinity but the lowest N_2 affinity. Finally, CS-AC has a low CO_2 affinity but a high N_2 affinity. The extended DSL isotherm model is assumed to describe the competitive nature adequately:

$$q^*_{\mathrm{CO_2}} = \frac{q_{\mathrm{sb,CO_2}} b_{\mathrm{CO_2}} C_{\mathrm{CO_2}}}{1 + b_{\mathrm{CO_2}} C_{\mathrm{CO_2}} + b_{\mathrm{N_2}} C_{\mathrm{N_2}}} + \frac{q_{\mathrm{sd,CO_2}} d_{\mathrm{CO_2}} C_{\mathrm{CO_2}}}{1 + d_{\mathrm{CO_2}} C_{\mathrm{CO_2}} + d_{\mathrm{N_2}} C_{\mathrm{N_2}}} \tag{2.20}$$

$$q^*_{\mathrm{N_2}} = \frac{q_{\mathrm{sb,N_2}} b_{\mathrm{N_2}} C_{\mathrm{N_2}}}{1 + b_{\mathrm{CO_2}} C_{\mathrm{CO_2}} + b_{\mathrm{N_2}} C_{\mathrm{N_2}}} + \frac{q_{\mathrm{sd,N_2}} d_{\mathrm{N_2}} C_{\mathrm{N_2}}}{1 + d_{\mathrm{CO_2}} C_{\mathrm{CO_2}} + d_{\mathrm{N_2}} C_{\mathrm{N_2}}} \tag{2.21}$$

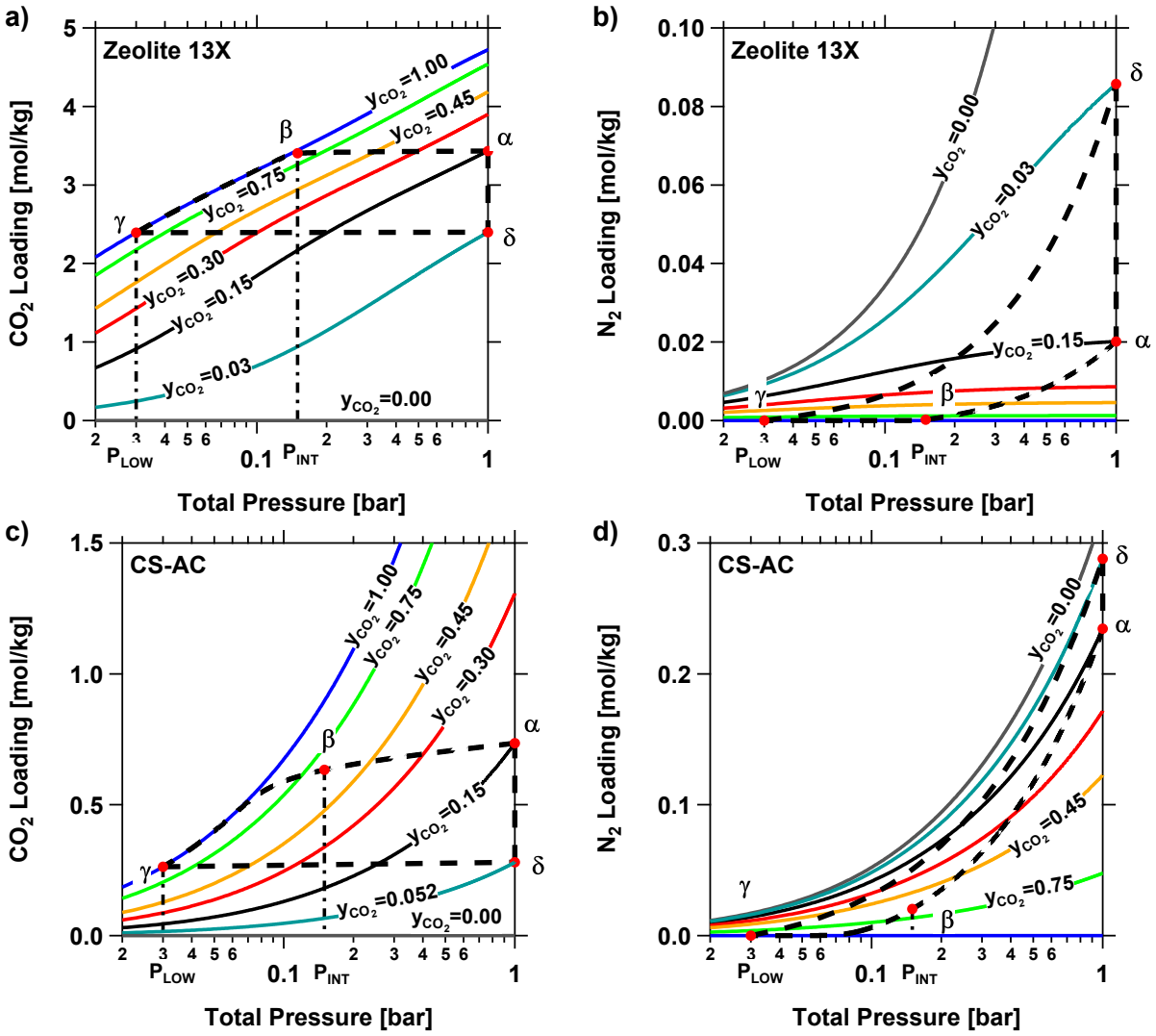

Figure 2.3: Transitions (black dashed lines) of the 4 Step VSA cycle with LPP calculated using the BAAM. a) CO_2 isotherm for Zeolite 13 X; b) N_2 isotherm for Zeolite 13X ; c) CO_2 isotherm for CS-AC; and d) N_2 isotherm for CS-AC.

The BAAM is run for fixed values of $P_{\mathrm{H}} = 1$ bar, $P_{\mathrm{INT}} = 0.15$ bar, $P_{\mathrm{LOW}} = 0.03$ bar, and T^{feed}=298.15 K for the four adsorbents. The calculated results of each step of the cycle are plotted in the respective CO_2 - N_2 competitive isotherm of the two adsorbents in Fig. 2.3. The competitive loadings, for different values of y_{CO_2} calculated from Eqs. 3.1 and 3.2, are plotted as a function of the total pressure. A semilog plot is used in order to illustrate the behaviour at low pressures. In Fig. 2.3, the black dashed line provides solution of the BAAM that are represented as transitions between the different states for Zeolite 13X (Figs. 2.3 a) and b)) and CS-AC (Figs. 2.3 c) and d)). Similar plots for Mg-MOF-74 and UTSA-16 are provided in the Appendix B. The case of Zeolite 13X is discussed first. At state α, the bed is completely

saturated with the feed CO_2 concentration, $y_{CO_2} = 0.15$. During the blowdown step, y_{CO_2} in the column increases as the weakly adsorbing component N_2 is removed from the column and is depicted by moving along the black dashed line in Figs. 2.3 a) and 2.3 b) from α to β. The CO_2 solid phase loading remains almost constant until CO_2 composition in the adsorber becomes $y_{CO_2} \approx 1.00$. Thereafter, in the evacuation step, the CO_2 loading decreases along the pure CO_2 isotherm until the state γ, corresponding to $P_{\mathrm{LOW}} = 0.03$ bar is reached. The LPP step, represented by the transition from γ to δ, is nearly a straight line on the CO_2 isotherm plot that can be identified by the intersection of a horizontal line from state γ, and a vertical line from $P_{\mathrm{H}} = 1$ bar. The adsorption step moves along the vertical line, $P_H = 1$ bar until state α is reached. Similar trends are observed for UTSA-16 and Mg-MOF-74.

In the case of CS-AC (Figs. 2.3 c) and d)) , there is a significant decrease in the CO_2 loading as one moves from α to β. Further, at $P_{\mathrm{INT}} = 0.15$ bar, the CO_2 composition is $y_{CO_2} = 0.65$ compared to $y_{CO_2} \approx 1.00$ in the case of Zeolite 13X. The inferior performance of CS-AC can be explained by observing the transition in N_2 isotherm in Fig. 2.3 d) that indicates that a significant amount of N_2 is left in the column at $P_{\mathrm{INT}} = 0.15$ bar. This observation can be explained by a lower selectivity and a weak CO_2 competition, thereby affecting the CO_2 purity and recovery. Table 2.2 provides the summary of the simulated results for the fixed operating condition. UTSA-16 gives $Pu_{CO_2} > 99.9\%$ and $Re_{CO_2} \approx 80\%$ with the lowest energy consumption of 88.50 kWh_e/tonne CO_2 cap. when compared to the other adsorbents. Mg-MOF-74, Zeolite 13X and UTSA-16 give similar CO_2 purity and recovery values for the given P_{LOW} and P_{INT} but there is a significant difference in energy values. CS-AC shows the worst performance among the four adsorbents considered.

Table 2.2: Performance indicators for $P_{\mathrm{LOW}} = 0.03$ bar, $P_{\mathrm{INT}} = 0.15$ bar and T =298.15 K.

Adsorbent	Pu_{CO_2} [%]	Re_{CO_2} [%]	En [kWh_e/tonne CO_2 cap.]			WC_{CO_2} [mol CO_2/m^3]
			BLO	EVAC	Total	
Mg-MOF-74	99.88	78.23	2.24	95.94	98.18	1750.2
Zeolite 13X	99.96	79.30	1.65	92.49	94.13	1143.0
UTSA-16	99.97	79.97	1.66	86.84	88.50	1674.4
CS-AC	94.42	55.63	19.19	99.49	118.68	297.2

As observed from Fig. 2.3, the transitions for the various steps of the 4-step VSA cycle with LPP, indicate that for materials with high selectivity, a simple approach can be used to estimate the process performance. The blowdown and evacuation transitions start from state α and

move horizontally, i.e., at constant $q^*_{CO_2}$, until $y_{CO_2} = 1.00$ is reached and follow $y_{CO_2} = 1.00$ isotherm until state γ is reached. For the LPP step, the value of $y^{\delta}_{CO_2}$ can be calculated by solving the isotherm expression by enforcing the condition $q^{*\gamma}_{CO2} = q^{*\delta}_{CO_2}$. With all the four states now identified, the purity, recovery, energy consumption and working capacity can be estimated. This approach is similar to those that have been used in the literature [43]. This approach is described separately in Appendix C.

2.3.2 Comparison of BAAM with the Detailed Model

In this section, the results from the BAAM are compared with the results obtained from the detailed model for the case of Zeolite 13X. For a process design of the 4-step VSA cycle with LPP using the detailed model, two pressures (P_{LOW}, P_{INT}), feed velocity (v_{feed}) and step times (t_{BLO}, t_{EVAC} and t_{ADS}) are the typical design variables. In order to compare the product purity and recovery, it is important to understand the impact of these six variables on the process performance. Of the six variables, P_{LOW}, P_{INT}, v_{feed} and t_{ADS} are the most critical ones. In a VSA process, the outlet flows typically drop exponentially as the pressure drops. In this case, if t_{BLO} and t_{EVAC} are kept sufficiently long, this will ensure that the purity and recovery from the process can be treated as the ideal case. In this study, P_{LOW} and P_{INT} are fixed at 0.03 bar and 0.15 bar respectively (as done in the previous section) while, t_{EVAC} and t_{BLO} are set to 200 s. Hence, we are left with t_{ADS} and v_{feed} as the two design variables. A parametric study is then performed by varying t_{ADS} and v_{feed} in the ranges, $0 < t_{\mathrm{ADS}}$ [s] < 180, and $0 < v_{\mathrm{feed}}$ [m/s] < 1.5 and the corresponding CO_2 purity and recovery contours are plotted as a function of t_{ADS} and v_{feed} in Fig. 2.4.

It is observed from Fig. 2.4 a) that the CO_2 purity increases, and approaches close to 100% when t_{ADS} and v_{feed} are high. Under these situations, the CO_2 composition front has the opportunity to completely saturating the bed with the feed and most of the N_2 is removed in the blowdown step. This condition also means that large quantities of CO_2 will be also lost as raffinate product in the adsorption step leading to poor recoveries as seen in the top right corner in Fig. 2.4 b). The design space is then scanned to pick an operating condition from the detailed model which closely corresponds to the CO_2 purity and recovery values predicted from the BAAM. This is shown in red "$*$" in Fig. 2.4. For this case, the energy consumption from the full model is found to be 125.68 kWh_e/tonne CO_2 cap. which is significantly high when compared to the result from the BAAM for Zeolite 13X given in Table 2.2, which is 94.13 kWh_e/tonne CO_2 cap. To understand the differences in energy values, the same exercise was repeated, but now by assuming an isothermal operation and no pressure drop across the column. This required some changes to the operating conditions in order to ensure that the CO_2 purity and recovery are

comparable to the BAAM. The energy-consumption from the detailed model dropped to 108 kWh_e/tonne CO_2 cap. (15% less than the previous case) for the similar values of CO_2 purity and recovery. Assuming zero mass transfer resistance and axial dispersion would further reduce the energy consumption calculated from the detailed model. Summarizing, the BAAM can represent the dynamics of the detailed model only under certain fixed operating conditions, i.e., when the column is fully saturated with the feed and when the key assumptions of the BAAM are enforced on the detailed model. This is a key limitation of the BAAM.

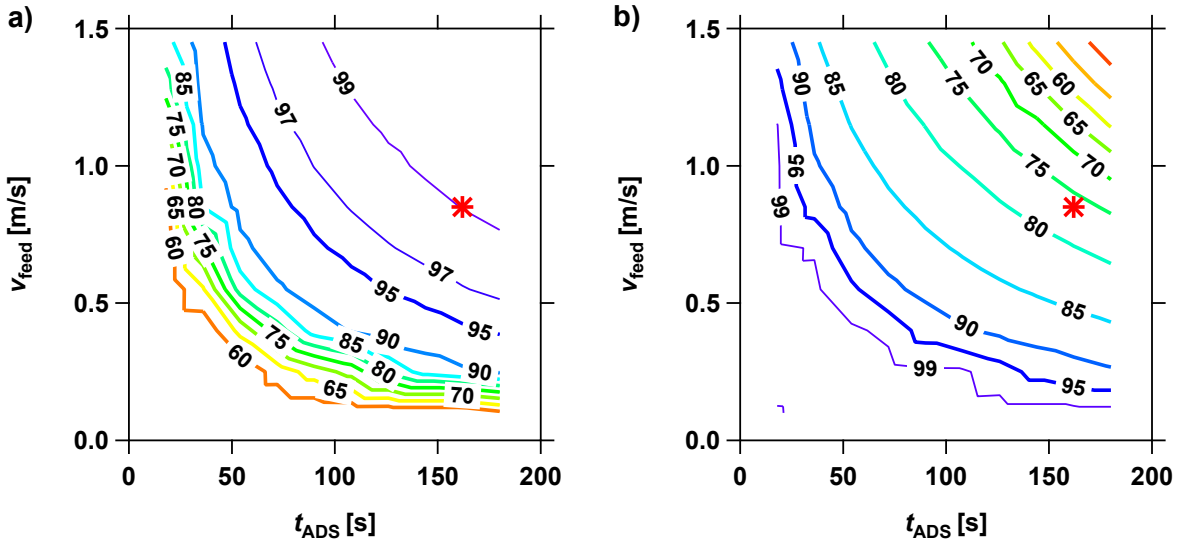

Figure 2.4: Contours of a) CO_2 purity and b) CO_2 recovery plotted as a function of t_{ADS} and v_{feed} from the detailed model for the case of Zeolite 13X. $P_H = 1$ bar, $P_{INT} = 0.15$ bar, $P_{LOW} = 0.03$ bar, $t_{BLO} = t_{EVAC} = 200$ s. The point shown in red $*$ gives Pu_{CO_2} and Re_{CO_2} comparable to the values obtained from the BAAM at $P_H = 1$ bar, $P_{INT} = 0.15$ bar.

2.4 Parametric Study using BAAM

The previous section described the simulated results for a fixed P_{LOW} and P_{INT}. Evaluation of the adsorbents for a fixed operating condition does not guarantee the correct ranking as the optimal performance of an adsorbent might be different from the fixed operating conditions that have been considered. A parametric study is performed for the case of Zeolite 13X by varying P_{LOW} and P_{INT} in the ranges of $0.03 \leq P_{LOW}$ [bar] ≤ 0.1 and $P_{LOW} + 0.01 \leq P_{INT}$ [bar] $\leq P_H - 0.01$ using the BAAM model. The contour plots of each of the performance indicators are generated to study the operating regions giving high product purity and recovery with lower energy consumption and higher working capacity.

Figure 2.5 a) shows that CO_2 purity is dependent on the value of both P_{INT} and P_{LOW}. At a

given P_{INT}, CO_2 purity increases with decreasing P_{LOW}. At a fixed P_{LOW}, CO_2 purity increases with decreasing P_{INT}. In the former case, reducing P_{LOW} increases the working capacity of the sorbent as the non-linear portion of the isotherm is accessed. In the latter case, lowering P_{INT} increases the amount of N_2 that is removed thereby resulting in higher CO_2 purity. A value of $Pu_{\mathrm{CO_2}} \approx 100$ is achieved when P_{INT} is close to its lower bound for a fixed P_{INT}. The CO_2 recovery shows a similar trend for a fixed P_{INT}. However, for a fixed P_{LOW}, P_{INT} has a minimal effect on recovery for $P_{\mathrm{INT}} > 0.15$ bar. From Fig. 2.5a, it can be seen that the amount of CO_2 removed is hardly affected in the range $0.15 < P_{\mathrm{INT}}$ [bar] < 1 and this explains why $Re_{\mathrm{CO_2}}$ is unaffected.

The energy contours are shown in Fig. 2.5 b). For a specific value of P_{H} and $y^{\mathrm{feed}}_{\mathrm{CO_2}}$, the total power consumption [$\mathrm{kWh_e}$] is only a function of P_{LOW}. However, the specific power consumption [$\mathrm{kWh_e}$/tonne CO_2 cap.] depends on the amount of CO_2 recovered in the evacuation step; in other words a function of the recovery. Hence, it comes as no surprise that the contours of the specific-energy resemble that of the recovery, i.e., the specific power consumption is sensitive to P_{LOW} for a fixed P_{INT}, but insensitive to P_{INT} for $P_{\mathrm{INT}} > 0.15$ bar where P_{LOW} is fixed.

The working capacity contours in Fig. 2.5 c) depict the same trend as seen with the recovery contours. Working capacity as high as 1050 mol CO_2/m^3 are achieved at very low pressures. The values of purity and recovery for a fixed value of P_{LOW} and variable P_{INT} are shown in Fig. 2.5 d). It is observed that the best combination of product purity and recovery is achieved when P_{LOW} is at the lowest value. The outermost front in Fig. 2.5 d). will be referred to as the purity-recovery "Pareto curve" for the BAAM model.

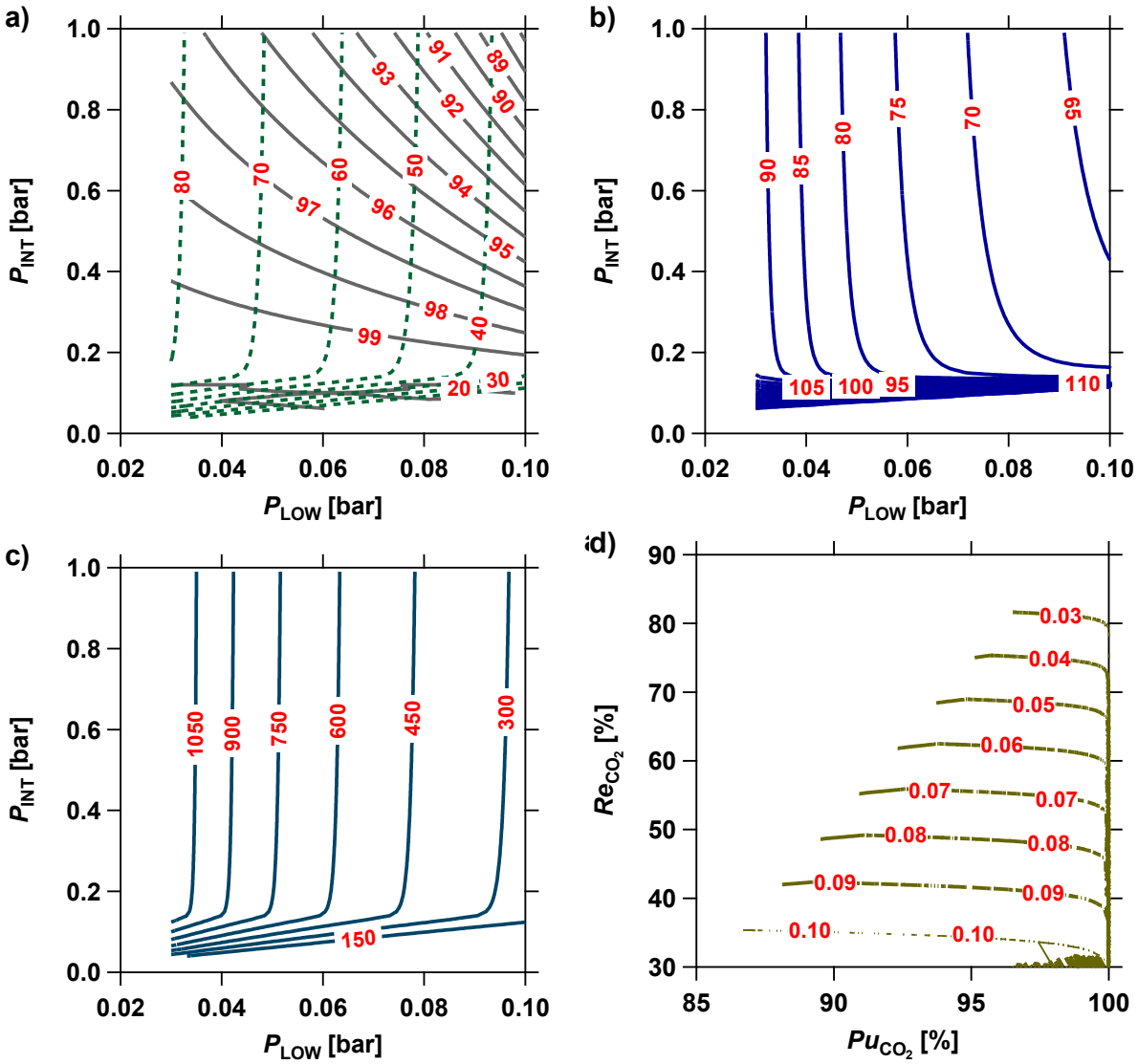

Figure 2.5: Contour plots of process indicators for Zeolite 13X calculated from the BAAM a) $Pu_{\mathrm{CO_2}}$ (solid lines) and $Re_{\mathrm{CO_2}}$ (dashed lines); b) Energy consumption in $\mathrm{kWh_e}$/tonne $\mathrm{CO_2}$ cap. c)Working capacity in mol $\mathrm{CO_2}$/ $\mathrm{m^3}$. Sub-figure d) shows the purity-recovery Pareto curves for various values of P_{LOW}.

2.4.1 Comparison of BAAM with the Optimized Results from Detailed Model

In order to evaluate various adsorbents, it is important to compare their optimal performance. Figures 2.6 a) and b) shows the purity-recovery Pareto curves for the 4 adsorbents obtained from the BAAM and the optimization of the detailed model, respectively. It is important to note that the values of P_{H}, P_{LOW}, y^{feed} and T^{feed} are identical for both the detailed model and the BAAM. The detailed model considers t_{ADS}, v_{ADS}, t_{BLO} and t_{EVAC} as decision variables.

Comparing Figs. 2.6 a) and b), two observations become evident: 1) the maximum recovery values predicted from the BAAM are lower when compared to their detailed model counterparts; 2) the BAAM predicts a purity of 100% at relatively higher recovery for Mg-MOF-74, Zeolite 13X and UTSA-16. The former observation can be explained by the assumption in the BAAM that requires the column to be completely saturated with the feed in the adsorption step and partly due to the absence of axial concentration and temperature profiles in a perfectly-mixed batch system. As a result, a significant amount of CO_2 is lost during the adsorption step whereas in the detailed model by controlling the position of CO_2 front in the column, it is possible to prevent the loss of CO_2 in the adsorption step. The latter observation can be understood by looking at the simplified process transitions in Fig. 2.3 and also contour plots in Fig. 2.5. When P_{INT} is decreased from 1 to 0.15 bar, the recovery is fairly constant due to the flat blowdown profile for the case of Zeolite 13X but the purity increases significantly until P_{INT} corresponding to $y_{\mathrm{CO_2}} = 1.00$ is reached. At this point, the CO_2 purity equals 100% but the recovery decreases when P_{INT} approaches P_{LOW}.

A closer examination of Fig. 2.6 a) and Fig. 2.6 b) reveals an interesting correlation. Although the absolute values of CO_2 purity and recovery do not match, the BAAM gives a correct ranking of adsorbents as compared with the detailed optimized ranking. Thus, based on maximization of purity-recovery values, the decreasing order of ranking of the adsorbent is UTSA-16 > Zeolite 13X > Mg-MOF-74 > CS-AC.

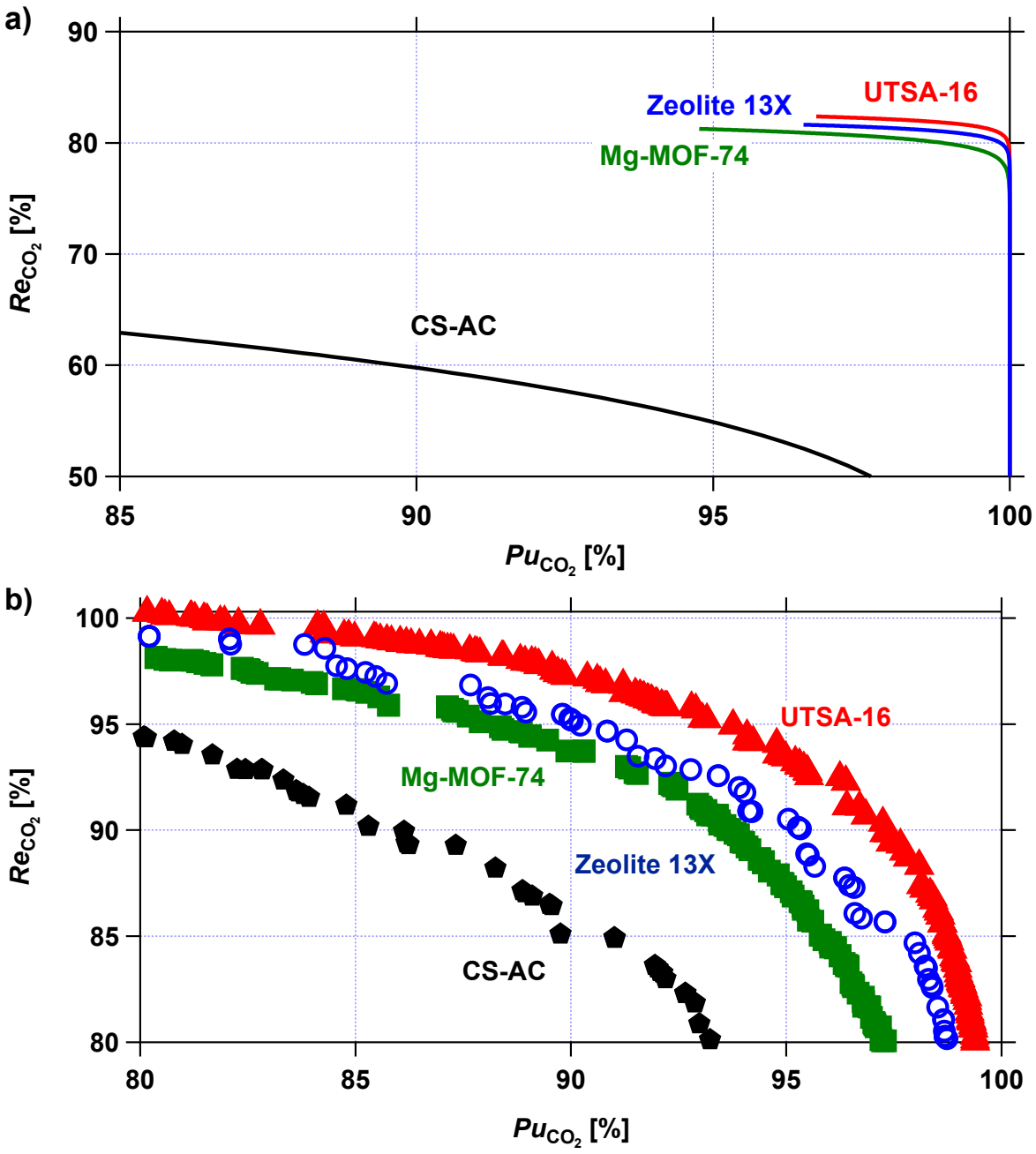

Figure 2.6: Comparison of Pu_{CO_2} and Re_{CO_2} Pareto curves obtained from a) the BAAM b) optimization using the detailed model [2].

2.5 Using the BAAM for Adsorbent Screening

In the previous section, the performance of the BAAM was compared with the detailed model under optimized conditions, and it was observed that the model under-predicts the purity and recovery performance although providing the correct ranking of the adsorbents. While this is helpful, the practical questions that need to be answered are: "Will a particular adsorbent be able to produce $Pu_{CO_2} \geq 95\%$ and $Re_{CO_2} \geq 90\%$? in order to satisfy US-Department of Energy (US-DOE) requirements" and "If so, what is the energy consumption of the process while guaranteeing US-DOE targets". The aim of this section is to develop a classification and energy scaling approach that will help answer these questions.

Khurana and Farooq examined a set of adsorbents for adsorbent screening using the detailed model process optimization [1]. A total of 75 adsorbents, including a wide range of zeolites, zeolitic imidazolate frameworks (ZIFs), cation exchanged zeolites (CEZs), porous polymer networks (PPNs) and metal- organic frameworks (MOFs) containing both real and hypothetical adsorbents were examined. A detailed multi-objective optimization aimed to maximize Pu_{CO_2} and Rec_{CO_2} was performed and those adsorbents that met US-DOE requirements were screened. For those adsorbents that met these requirements, a separate optimization run that aimed to minimize energy while satisfying the Pu_{CO_2} and Rec_{CO_2} constraints was performed. The results of this study are provided in the Appendix D. This group of adsorbents along with the four that have been considered in the previous sections, totalling 79, were used to develop a classification and energy scaling approach for the BAAM. The adsorbents were described by the authors using a DSL model and the fitting parameters are provided in the Appendix D.

2.5.1 Purity - Recovery Classifier

The BAAM was used to generate the purity - recovery Pareto curves for the 79 adsorbents for a low pressure P_{LOW} of 0.03 bar and different intermediate pressures. The purity - recovery Pareto curves obtained from the BAAM are plotted in Fig. 2.7. Two colours are used to plot these curves: green curves are used to represent those adsorbents that were identified by Khurana and Farooq to have met the US-DOE purity-recovery constraints; and red curves were used to represent adsorbents that failed to meet the constraint. It is interesting to note that there is a clear clustering of green curves towards the top-right and the red ones towards the bottom left. This shows the potential of the BAAM to be used as a classifier. In order to reduce the two-dimensional measure (the Pareto curve), to a one-dimensional measure, the maximum Eucledian distance from the origin (denoted as r_{max}) to the Pareto curve is considered as a proxy for the performance of an adsorbent. The mathematical description of r_{max} is given by:

$$r_{\max} = \text{Max}\left(r(Pu_{\text{CO}_2}, Re_{\text{CO}_2})\right) \tag{2.22}$$

where r is the distance of each point on the Pareto curve, which is defined as:

$$r = \sqrt{\left(Pu_{\text{CO}_2}\right)^2 + \left(Re_{\text{CO}_2}\right)^2} \tag{2.23}$$

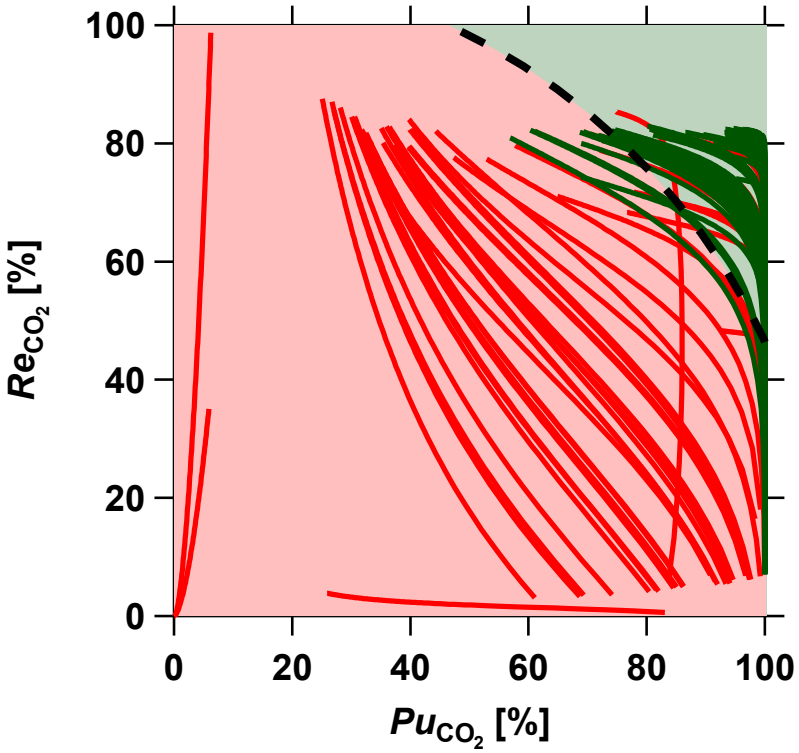

Figure 2.7: Collection of purity-recovery Pareto curves calculated using the BAAM for 79 adsorbents The green curves correspond to the adsorbents that met $Pu_{\text{CO}_2} = 95\%$ and $Re_{\text{CO}_2} = 90\%$ and the red ones correspond to those that did not satisfy based on the detailed model optimization [1]. The black dashed line represents the locus of r_{95-90}. In order to meet the $Pu_{\text{CO}_2} = 95\%$ and $Re_{\text{CO}_2} = 90\%$ requirement, a point on the Pareto curve of an adsorbent obtained from the BAAM should fall above this curve.

Now, the goal is to determine the value of r_{95-90} that provides the best classification for identifying materials that can provide $Pu_{\text{CO}_2} \geq 95\%$ and $Re_{\text{CO}_2} \geq 90\%$. The classification learner toolbox available in MATLAB was used to perform the linear discriminant analysis with 5-fold cross validation with $r_{\max}$ for 79 adsorbents as the input and the Pu_{CO_2}-Re_{CO_2} constraints from the detailed model optimization as the response. The results of the full model were converted into a binary output. A value of "1" was assigned if the purity-recovery constraint was achieved

and a value of "0", otherwise. The analysis resulted in $r_{95-90} = 110.25$ with an accuracy of 87.3 %. In other words, an adsorbent with a $r_{\max} \geq r_{95-90} = 110.25$, is expected to meet US-DOE requirements while an adsorbent with a $r_{\max} < 110.25$ is not expected to meet the targets. The black dashed line, in Fig. 2.7, represents the points for which $r = r_{95-90} = 110.25$. This curve divides the whole plot into two regions one where the Pu_{CO_2}/Re_{CO_2} constraints are satisfied (green shade) and the other where it is not (red shade).

The efficacy of the BAAM to classify a material according to its potentially to satisfy US-DOE purity-recovery targets is compared with a variety of performance metrics that are used in the literature. A list of performance metrics tested and their definitions is given in Table 2.3. The details of these metrics have been discussed in a previous work [2]. For each of the 79 adsorbents the set of performance metrics were calculated based on their isotherms. Each metric was used as an input in MATLAB classification learner toolbox in order to predict the digital output (1 if purity-recovery constraints are met and 0, otherwise). The classification accuracy for each of the adsorbent metric is listed in Table 2.3 and it can be observed that the BAAM significantly outperforms every other metric. The classification accuracy is the ratio of the sum of true positive (TP) and true negative (TN) over the total number of observations. This is misleading at times as a randomly generated metric is shown to have a classification accuracy of 53.16 %. To overcome this, Matthews correlation coefficient is computed which helps us quantify the classification ability of each metric by considering all of true positive (TP), true negative (TN), false positive (FP) and false negative (FN). Ideally, MCC should be closer to one to have a good classification. This comparison highlights the advantage of the BAAM that has a high classification accuracy and higher MCC without any significant increase in the computational time.

Table 2.3: US-DOE purity-recovery classification accuracies of commonly used adsorbent performance metrics based on the 79 adsorbents considered in this study. The equilibrium loadings at adsorption and desorption conditions are $q^*_{ads} = q^*\left(1\text{bar}, 298.15\text{K}, y^{\text{feed}}\right)$ and $q^*_{des} = q^*\left(0.03\text{bar}, 298.15\text{K}, y^{\text{feed}}\right)$, respectively.

Adsorbent Metric	**Definition**	**Classification accuracy** [%]	**MCC** [-]
CO_2 adsorption capacity [mmol g^{-1}]	$q^*_{ads,\text{pure}}\Big\vert_{\text{feed}}$	63.3	0.26
Henry selectivity [-]	$S_{\text{H}} = \frac{H_{\text{CO}_2}}{H_{\text{N}_2}} = \frac{(q_{\text{sb}}b + q_{\text{sd}}d)_{\text{CO}_2}}{(q_{\text{sb}}b + q_{\text{sd}}d)_{\text{N}_2}}$	53.2	0.00
Pure-component selectivity [-]	$S_{\text{pure}} = \left[\left(\frac{q^*_{\text{CO}_2,\text{pure}}}{q^*_{\text{N}_2,\text{pure}}}\right)\frac{y_{\text{N}_2}}{y_{\text{CO}_2}}\right]\Big\vert_{\text{feed}}$	51.9	0.00
Competitive selectivity [-]	$S_{\text{comp}} = \left[\left(\frac{q^*_{\text{CO}_2,\text{comp}}}{q^*_{\text{N}_2,\text{comp}}}\right)\frac{y_{\text{N}_2}}{y_{\text{CO}_2}}\right]\Big\vert_{\text{feed}}$	53.2	0.00
Pure-component working capacity [mmol g^{-1}]	$WC_{\text{pure}_i} = \left(q^*_{ads,\text{pure}} - q^*_{des,\text{pure}}\right)\Big\vert_{\text{feed}}$	65.8	0.31
Competitive working capacity [mmol g^{-1}]	$WC_{\text{comp}_i} = \left(q^*_{ads,\text{comp}} - q^*_{des,\text{comp}}\right)\Big\vert_{\text{feed}}$	68.4	0.34
Notaro's FOM [mol kg^{-1}]	$\gamma_{\text{N}} = WC_{\text{comp}_{\text{CO}_2}}\left(\frac{S^2_{\text{comp}_{ads}}}{S_{\text{comp}_{des}}}\right)$	53.2	0.00
Ackley's FOM [mol kg^{-1}]	$\gamma_{\text{A}} = WC_{\text{comp}_{\text{CO}_2}}\left(\frac{WC_{\text{pure}_{\text{CO}_2}}}{WC_{\text{pure}_{\text{N}_2}}}\right)$	65.8	0.37
Yang's FOM [-]	$\gamma_{\text{Y}} = S_{\text{comp}}\left(\frac{WC_{\text{pure}_{\text{CO}_2}}}{WC_{\text{pure}_{\text{N}_2}}}\right)$	53.2	0.00
Wiersum's FOM [mol^3 J^{-1} kg^{-2}]	$\gamma_{\text{W}} = \frac{(S_{\text{comp}}-1)^{0.5}WC^2_{\text{comp}_{\text{CO}_2}}}{\vert\Delta H_{\text{ads}_{\text{CO}_2}}\vert}$	68.4	0.39
Random metric	-	53.16	0.04
Batch adsorber analogue model	-	87.3	0.77

2.5.2 Calculation of Minimum Energy

In order to compare the performances of different adsorbents, it is important that energy consumption has to be calculated at a specific Pu_{CO_2} and Re_{CO_2}. The energy consumption, for the case of Zeolite 13X, plotted in Fig. 2.5 b) is re-plotted in Fig. 2.8 a) but now as a function of Pu_{CO_2} and Re_{CO_2}. In addition to the contours of energy, the locus of r_{95-90} is plotted as black dashed line. As it can be seen, the values of energy vary as one moves along the dashed line. The energy value decreases, reaches a minimum and then increases. In this case, we choose the minimum energy that coincides with the locus of r_{95-90} as being representative of the minimum energy for this adsorbent. This choice is not based on any physical argument, but is simply suggested as an approach that will allow the development of a consistent methodology.

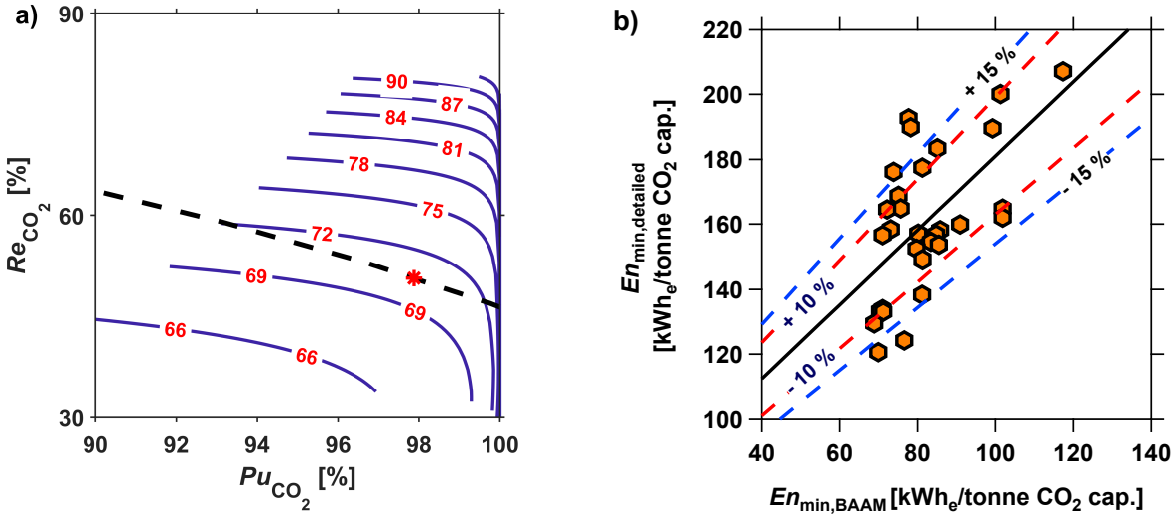

Figure 2.8: Calculation of energy consumption using the BAAM. a) Energy contours as a function of CO_2 Purity and Recovery for the case of Zeolite 13X. The black dashed line represents the locus of r_{95-90} with the minimum energy point being shown as a "*". b) Linear regression relating the minimum energy values computed from the BAAM to that of the optimization of the detailed model.

The minimum energy values thus obtained from the BAAM for each of the adsorbents are compared with the corresponding minimum energy values from the detailed model in Fig. 2.8 b). It is important to note that only 35 of the 79 adsorbents that met the purity-recovery constraints were considered for the energy consumption calculations. A linear regression was performed to find the relationship between minimum energies calculated from the BAAM and that of the detailed model. This relationship is provided by

$$En_{\text{min,scaled}} = 1.1446 En_{\text{min,BAAM}} + 66.53 \tag{2.24}$$

where $En_{\text{min,scaled}}$ is the scaled energy that can be compared with results from a full model. As seen in Fig. 2.8 b), the minimum energies of 53% of the 35 adsorbents were predicted within $\pm 10\%$ and that of 83% was predicted within $\pm 15\%$ of the values from the detailed model. This accuracy seems reasonable considering the number of assumptions that went into developing the BAAM along with a significant reduction in computational time.

2.5.3 Ranking Metric

In order to compare the multiple adsorbents, both the minimum energy and working capacity need to be considered. The minimum energy and the corresponding working capacity for the 35 adsorbents that satisfied $Pu_{\text{CO}_2} - Re_{\text{CO}_2}$ constraints are shown in Fig. 2.9 a). An ideal adsorbent is the one with that has a low minimum energy consumption and corresponding high working capacity. This would form the bottom-right corner of the plot. It is worth noting here that Zeolite 13X, which is commercial and available at a modest cost stands out as one of the materials with the lowest energy consumption. UTSA-16 that has a low N_2 affinity, and a few hypothetical adsorbents, outperform Zeolite 13X. These results are consistent with other reports in the literature [1]. Some of the promising adsorbents are named in Fig. 2.9 a), while the values of the minimum energy calculated from the BAAM for the other adsorbents are provided in the Appendix D.

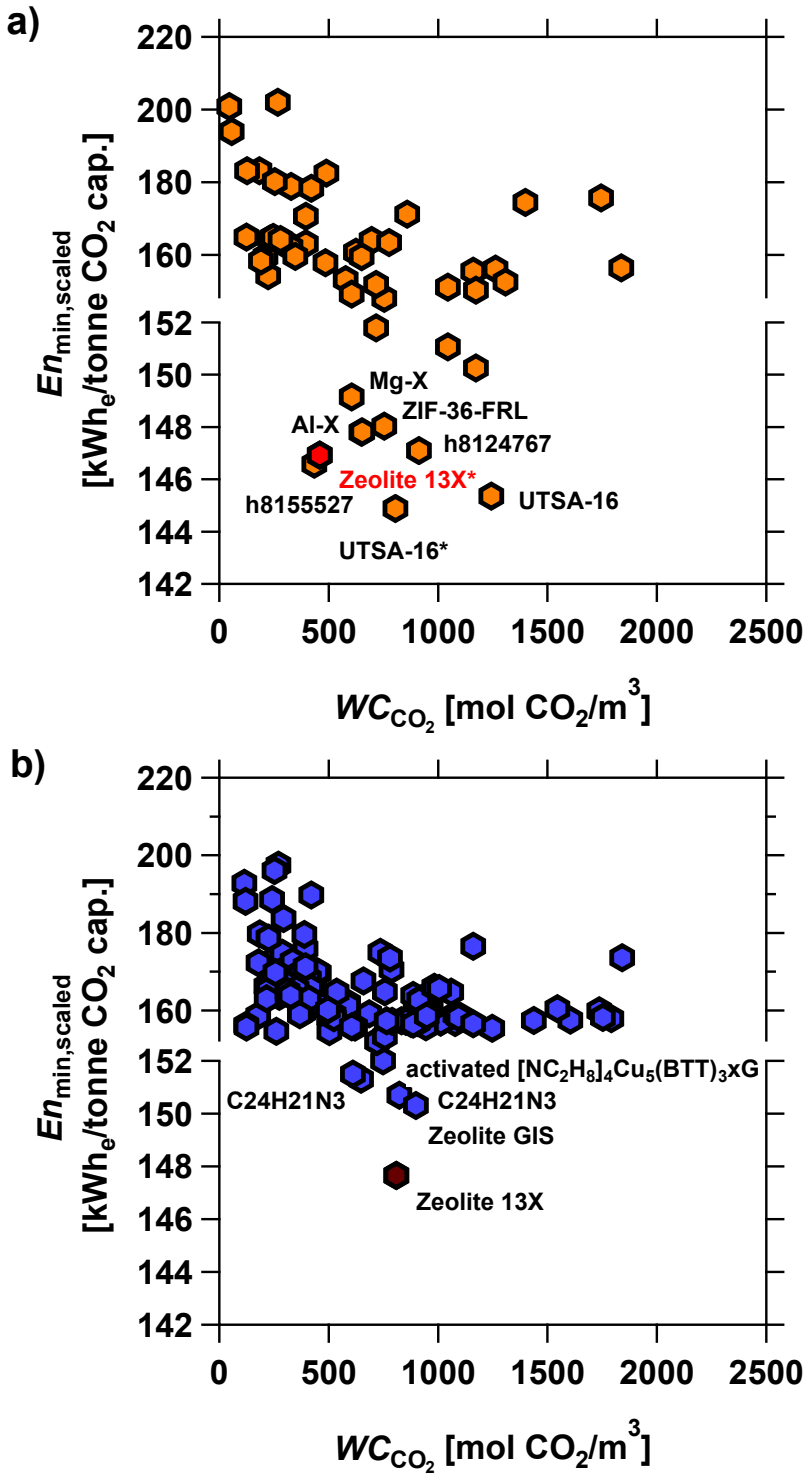

Figure 2.9: Plots of working capacity vs. minimum energy calculated from the BAAM. a) Shows the adsorbents considered by Khurana and Farooq [1] and this work. b) Shows the results from the screening of the NIST/ARPA-E Database.

2.6 Screening of the NIST/ARPA-E Database

The National Institute of Standards and Technology (NIST) maintains a free and publicly accessible NIST/ARPA-E Database of Novel and Emerging Adsorbent Materials reported from the wide range of scientific literature [47]. The database, which is growing at a rapid rate, includes data from published experimental and theoretical studies that are self-reported. In this section, the potential of the BAAM is demonstrated by using it to screen this large publicly available database. The objective is to identify those adsorbents that have the potential to meet US-DOE purity-recovery targets and if so, calculate their parasitic energies.

The database consists of thousands of isotherm datafiles. Hence, it was important to develop a filtering scheme in order to identify those materials for which reliable adsorption isotherm data is available within the range of interest for post-combustion CO_2 capture. The approach which is graphically described in the Appendix E is briefly described here. A query was made through Python API script to retrieve all the adsorption isotherm data for all the adsorbent materials for which CO_2 and N_2 were reported as the adsorbates. The query resulted in 810 Digital Object Identifiers (DOIs), which represents an unique information source. This process also yielded the isotherm data of other adsorbates and competitive isotherm data which were not of interest to the current work. Accordingly, these data points were removed in the first step before analyzing the data. This step identified those data points that contained isotherm information for pure CO_2 **and** N_2 on the material. This filter resulted in 757 DOIs and 1540 unique adsorbents. At this stage, it was important to convert the reported values of pressure, loading and temperature into a common unit. Pressure and temperature units were reported only in bar and K, respectively. These were retained as they are. However, equilibrium loadings were reported in a variety of units and the corresponding conversion factors were applied to convert to a common unit (in this case "mmol/g"). For loadings that were reported on a "per unit volume of the adsorbent", an adsorbent density of 1130 kg/m^3, that corresponding to Zeolite 13X, was chosen to convert to per unit weight of the adsorbent. Materials for which equilibrium loadings were reported on a "per unit-cell" basis were not considered further. This filter results in 743 DOIs and 1486 unique adsorbents. It is important to note here that multiple DOIs could report data on materials that have identical names. For example, data on "Zeolite 13X" was reported by 17 DOIs. In this study, each of this Zeolite is considered as a unique adsorbent. The BAAM requires isotherm information for both CO_2 and N_2 at low pressures, i.e, < 1 bar and at 298 K. Hence, it was important to identify data that included this information. Applying this filter, significantly reduced the search space to only 102 DOIs and 159 unique adsorbents. It was seen that most of the isotherm data for CO_2 were reported at 273 K while N_2 data was reported at 77 K, primarily as a part of the adsorbent characterization experiments. Upon closer inspection of

the data it was found that some DOIs reported multiple CO_2 isotherms for the same adsorbent at 298K. Investigating the primary reference revealed that these could be results of theoretical studies, experimental measurements or even data from other research groups that were merely referenced to. Under these situations, each set of isotherm was assumed to belong to a variant of the same adsorbent. In a similar fashion, some DOIs reported multiple N_2 isotherms. In such a situation, in order to avoid the multifarious combinations of CO_2 and N_2, we just considered the N_2 isotherm that showed the highest loading at 1 bar pressure.

The CO_2 and N_2 isotherm data hence obtained was described by Single Site Langmuir (SSL) model by forcing equal saturation loadings for the two adsorbates thereby ensuring thermodynamic consistency. Note that the SSL is a special form of the DSL in which only one of two Langmuirian terms is retained. The complete list of materials along with the SSL isotherm parameters is provided in Appendix E. The BAAM was then run to identify adsorbents that could meet the US-DOE $Pu_{CO_2} - Re_{CO_2}$ constraints. Of the 197 materials, a total of 120 were found to meet the requirements. The minimum energy and the corresponding working capacity, for these 120 materials were computed and depicted in the Fig. 2.9 b). The process of isotherm fitting and the BAAM calculations was completed in less than two seconds per adsorbent. Zeolite 13X still stands out as the best performing adsorbent in terms of minimum energy consumption from screening the NIST database. A few other zeolites, microporous organic polymers (MOPs) and metal organic frameworks (MOFs), namely Zeolite GIS, C24H21N3 and activated $[NC_2H_8]_4Cu_5(BTT)_3$xG offer low parasitic energies. It is important to acknowledge that is is quite possible that promising adsorbents could have been missed based on the filtering approach that was adopted. This highlights the fact that reporting of equilibrium data for both CO_2 at capture conditions and N_2 is critical in order to perform reliable screening [48]. However, the objective of this exercise, which was to showcase the flexibility and speed of the BAAM that can be adapted to any large database, has been sufficiently demonstrated.

2.7 Conclusions

In this work, a batch adsorber analogue model (BAAM) based on the framework described by Maring and Webley has been developed. It is based on several simplifying assumptions that aims to reduce the computational complexity. Specifically, the adsorber is considered as a mixed system that is isothermal and with the solid reaching instantaneous equilibrium with the fluid phase. This reduces the PDEs to ODEs and eliminates the heat balances and the solid-fluid mass balances. It was shown that the results of the BAAM can be represented on a isotherm plot that requires only the description of the competitive behaviour of CO_2 and N_2. Under certain conditions, a simple graphical solution, which does not require the solution of ODEs,

can be obtained. By comparing the results of the BAAM with those from detailed optimization studies, a classification model was developed that showed a 87.3% accuracy in determining whether an adsorbent can produce a $Pu_{CO_2} \geq 95\%$ and $Re_{CO_2} \geq 9\%$ when implemented in a full-scale process. A simple linear relationship to calculate the minimum energy calculated from the BAAM was developed. It was able to estimate the minimum energy within $\pm 15\%$ for over 83% adsorbents. The ability of the model to screen large number of materials was demonstrated by considering 197 adsorbents from the NIST/ARPA-E database.

In this work the advantages and shortcomings of the BAAM was studied by comparing its result with those from detailed models. The BAAM has three important shortcomings. First, the model is based on several assumptions that are far from reality. Real VSA units work under non-isothermal conditions; mass and heat transfer rates are finite and there is a pressure drop across the column. A real post-combustion flue gas also contains impurities and moisture that can significantly affect adsorbent performance. In fact, as discussed, the ability to control the position of the mass and thermal fronts is the basis of an adsorption process. Second, it has a finite accuracy in being able to either determine purity-recovery classification or to calculate the energy calculation. Hence, it is advisable not to select adsorbents purely on the basis of the BAAM or any other simplified model as suggested in many papers in the literature. Third, the operating conditions obtained from the BAAM can not be translated to an experimental demonstration. A detailed model is required to identify the best operating conditions for a particular adsorbent before proceeding to the experimental stage. The key advantage of the BAAM is the speed with which the purity-recovery classification and minimum energy consumption can be calculated. It takes less than a second to perform these calculations on a standard laptop computer, compared to a few days that is required for detailed process optimization. It was shown that in terms of the accuracy with which the classification can be performed, the BAAM outperforms simple adsorption metrics without any increase in computational time. In conclusion, it is recommended that the BAAM be used to perform a preliminary screening and identify a handful of adsorbents that can be further studied using the detailed model combined with rigorous optimization. This approach could potentially increase the success rates in screening materials while reducing the time for screening. Further, the ability to predict broad trends and to understand them based just on the isotherms still makes this a powerful tool in the suite of models that are available to process engineers.

Chapter 3

Applications of Batch Adsorber Analogue Model for a large-scale adsorbent screening

3.1 Introduction

Zeolites are porous crystalline aluminosilicate structures which consist of SiO_4 and AlO_4 units joined together through shared oxygen atoms to form an open-uniform crystal lattice [18]. Zeolites find its applications in ion exchange, catalysis, environment protection and gas separations [18, 49]. As of 2016, 232 unique zeolite framework structures have been synthesized and categorized by the Structure Commission (SC) of the International Zeolite Association (IZA) (IZA-SC) [50]. Each of the unique frameworks has the three letter word recognized by IUPAC. The database of new-zeolite like materials with more than 2.6 M unique structures, provides the comprehensive list of all predicted zeolite-like materials which are structurally, topologically and geometrically similar to that of zeolites [21,51]. The list of all hypothetical zeolite-like structures can be accessed at `www.hypotheticalzeolites.net/database/deem/`. Zeolite 13X stands out among the family of zeolites and also the current benchmark adsorbent for post-combustion carbon capture [3]. Metal-organic frameworks (MOFs) are relatively a new class of crystalline compounds consisting of inorganic metal clusters coordinately bonded to the organic ligands resulting in highly porous structures. Zeolitic imidazole frameworks (ZIFs) are a special class of MOFs having topology similar to that of aluminosilicate zeolites. ZIFs are neutral frameworks in which metal ion being Zn or Co is linked to ditopic imidazolate [52, 53]. The imidazolate linkers in ZIFs (Im-M-Im) resemble the shared oxygen atoms in zeolites.

Given a large number of adsorbents, as described above, for CO_2 capture application, it is practically impossible to characterize each one of them using experimental techniques. Thanks to the significant advancements in the computation power, high-throughput computational screening becomes vital to screen for the best adsorbents at a faster rate. In the first step of screening, any of the databases with the crystal structure is chosen for the screening for any specific application. Secondly, Grand Canonical Monte Carlo (GCMC) and molecular dynamics (MD) simulations are performed with the crystal structures to compute the pure-component adsorption isotherms and the gas diffusion characteristics respectively. Then, the adsorbents are ranked based on any specific metric which is easier to compute. To incorporate process performances in some cases, the adsorbents are tested with detailed models coupled with optimization studies to choose the best candidates for CO_2 capture. If we look across the literature, this has been the trend with regards to the high throughput-computational screening [35, 54–58]. It is important here to acknowledge the validity of these models in predicting the adsorption isotherms.

In this chapter, BAAM was applied on one such database, the carbon capture materials database (CCMDB), from the University of California, Berkeley, to pick the best candidates with the least energy consumption for a pressure swing adsorption process. The BAAM's predictions were compared with the corresponding optimized results of the detailed model to show the efficacy of the model in predicting the minimum energy. Then, a parametric study was performed using BAAM to look for the ideal characteristics of the adsorbents with the least energy penalty. And, the chapter concludes with the closing remarks and the proposed future work.

3.2 Carbon Capture Materials Database (CCMDB)

Lin et al. screened nearly a hundred thousand zeolites and ZIFs for their feasibility of deployment in the carbon capture applications using a hybrid pressure and temperature swing adsorption cycle [35]. Zeolites, considered in that study, included all experimental zeolite crystal structures [59], and the predicted zeolite crystal structures which were derived from a comprehensive database of zeolite-like materials [51, 60]. The Henry coefficients, heats of adsorption, and saturation loadings for each of the materials with CO_2 and N_2 as adsorbates were computed using molecular simulations assuming that pure component isotherms could be described using dual- or single site Langmuir isotherm models on a graphics processing unit (GPU). The resulting adsorption isotherms were validated by the GCMC simulated competitive isotherms for a set of 50 structures [35]. The results of this work led to the creation of CCMDB which is accessible at `www.carboncapturematerials.org`. CCMDB is created and maintained by the Berkeley Lab's Computational Research Division as well as the Energy Frontier Research Center for Gas Separations Relevant to Clean Air Technologies. The database consists of details of geometri-

cal parameters, adsorption data and performance indicators such as parasitic energy, purity at minimum energy and working capacity of different zeolites and MOFs. In our study, we took the isotherm data of predicted zeolite structures from CCMDB and screened them using BAAM for their potential in the vacuum swing adsorption (VSA) process as opposed to their hybrid cycle. There were a total of 118,149 predicted-zeolites and the particle density, the single-site Langmuir (SSL) fitting parameters at 300 K of the same were provided.

As BAAM was developed and configured to run at 298.15 K, at first, using relevant conversion factors, the corresponding fitting parameters of all the adsorbents at 298.15 K were estimated. The histogram plot representing the probability distribution of each of the fitting parameters are given in Fig. 3.1. Henry constants of CO_2 and N_2 span a wide range of values as shown in Fig. 3.1 a) and b). The distribution of heat of adsorption of CO_2 stands out with considerable number of the adsorbents having the values in the range -32.7 to -33 kJ/mol. Most of the adsorbents have heat of adsorption of N_2 between -20 to -7 kJ/mol. The saturation loadings span between 0 to 15 mol/kg with densities varying from 1000 to 2500 kg/m^3. With the relevant fitting parameters, the CO_2-N_2 competition could be described using the extension of the SSL model as follows.

$$q^*_{\mathrm{CO_2}} = \frac{q_{\mathrm{sb,CO_2}} b_{\mathrm{CO_2}} C_{\mathrm{CO_2}}}{1 + b_{\mathrm{CO_2}} C_{\mathrm{CO_2}} + b_{\mathrm{N_2}} C_{\mathrm{N_2}}} \tag{3.1}$$

$$q^*_{\mathrm{N_2}} = \frac{q_{\mathrm{sb,N_2}} b_{\mathrm{N_2}} C_{\mathrm{N_2}}}{1 + b_{\mathrm{CO_2}} C_{\mathrm{CO_2}} + b_{\mathrm{N_2}} C_{\mathrm{N_2}}} \tag{3.2}$$

where,

$$b_{\mathrm{CO_2}} = b_{0,\mathrm{CO_2}} e^{-\Delta U_{\mathrm{b,CO_2}}/\mathrm{R_g}T} \tag{3.3}$$

$$b_{\mathrm{N_2}} = b_{0,\mathrm{N_2}} e^{-\Delta U_{\mathrm{b,N_2}}/\mathrm{R_g}T} \tag{3.4}$$

In the equations described above, $q^*_{\mathrm{CO_2}}$ and $q^*_{\mathrm{N_2}}$ are the equilibrium solid phase loadings corresponding to the fluid-phase concentrations of $C_{\mathrm{CO_2}}$ and $C_{\mathrm{N_2}}$, respectively. The constants $q_{\mathrm{sb,CO_2}}$, $q_{\mathrm{sb,CO_2}}$, $b_{\mathrm{CO_2}}$ and $b_{\mathrm{N_2}}$ are the equilibrium saturation solid phase loadings and affinity parameters, respectively. The constants $b_{0,\mathrm{CO_2}}$ and $b_{0,\mathrm{N_2}}$ are the pre-exponential factors, $\Delta U_{\mathrm{b_C O_2}}$ and $\Delta U_{\mathrm{b_{N2}}}$ are the internal energies. For thermodynamic consistencies, the saturation loadings are assumed to be equal, i. e., $q^*_{\mathrm{CO_2}} = q^*_{\mathrm{N_2}}$. Before proceeding further, it is important to define the Henry selectivity (α_{H}) and competitive selectivity (α_{C}) as below.

$$\text{Henry Selectivity}, \alpha_{\mathrm{H}} = \frac{q_{\mathrm{sb,CO_2}} b_{\mathrm{CO_2}}}{q_{\mathrm{sb,N_2}} b_{\mathrm{N_2}}} = \frac{b_{\mathrm{CO_2}}}{b_{\mathrm{N_2}}} \tag{3.5}$$

$$\text{Competitive Selectivity}, \alpha_{\mathrm{C}} = \frac{q^*_{\mathrm{CO_2}} C_{\mathrm{N_2}}}{q^*_{\mathrm{N_2}} C_{\mathrm{CO_2}}} = \frac{b_{\mathrm{CO_2}}}{b_{\mathrm{N_2}}} \tag{3.6}$$

As evident from the Eqs. 3.5 and 3.6, for a SSL model, $\alpha_{\mathrm{H}} = \alpha_{\mathrm{C}}$. The effects of selectivity on the process performance is discussed in detailed in the subsections coming below.

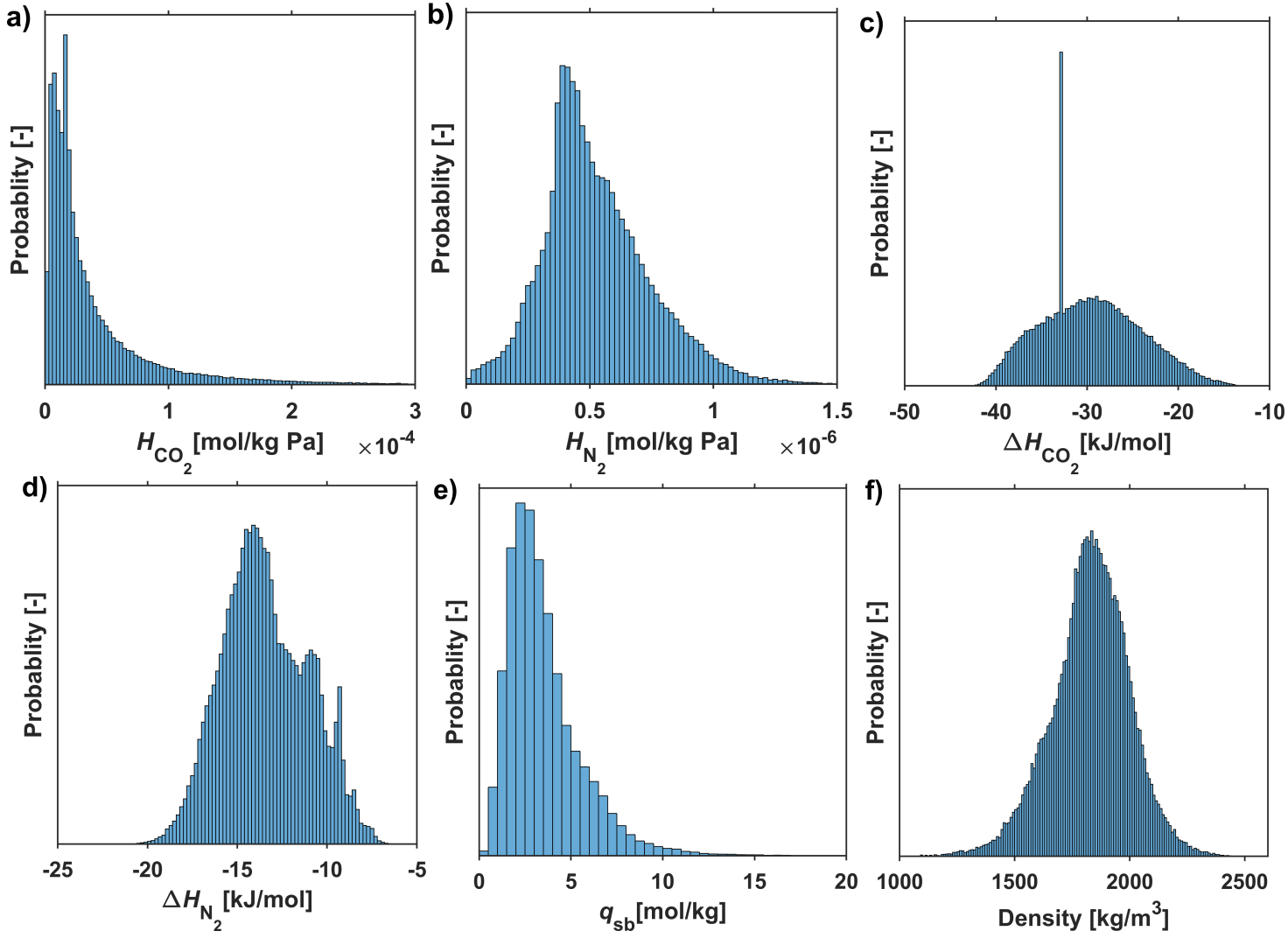

Figure 3.1: Histogram plots showing the probability distribution of a) Henry coefficient of CO_2 (H_{CO_2}), b) Henry coefficient of N_2 (H_{CO_2}), c) Heat of adsorption of CO_2 (ΔH_{CO_2}), d) Heat of adsorption of N_2 (ΔH_{N_2}), e) CO_2/N_2 saturation loading (q_{sb}), and f) particle density of the predicted zeolite structures in CCMDB.

3.2.1 Screening of CCMDB using BAAM

BAAM was run on these hypothetical zeolites (h-ZEOs) from CCMDB, firstly, to identify those which satisfy U.S.-DOE $Pu_{CO_2} - Re_{CO_2}$ constraints and secondly, to compute the parasitic minimum energies for those which satisfy the targets. As done previously, the low pressure, P_{LOW} and high pressure, P_H were fixed at 0.03 bar and 1 bar, respectively. P_{INT} was varied between $P_{LOW} + 0.01 \leq P_{INT}$ [bar] $\leq P_H - 0.01$. The temperature of the flue gas stream is taken to be 298.15 K. The MATLAB simulations were performed in a desktop workstation with two 12-core INTEL Xeon 2.5GHz processors and 128 GB RAM. It took less than a second to screen each of the materials and the entire screening process was completed in 97 minutes after parallelization on the 24-core workstation.

The large number of adsorbents with wide-ranging isotherm parameters makes the process of visualizing the BAAM's results complex. Any marker in Fig. 3.2 refers to a distinct adsorbent with a unique combination of H_{CO_2} and H_{N_2}. The slope of any line passing through the origin with positive slope in each of the plots in Fig. 3.2 is given by the Henry selectivity (α_H). Accordingly, all the adsorbents on the line passing through the origin will have the same selectivity. Different shades of lines in Fig. 3.2 corresponds to a unique selective given by the legend. A total of 107,225 of 118,149 adsorbents considered for screening, i.e., 90.8 % of the sample, were found to have $r_{max} \geq 110.25$, i.e., capable of meeting US-DOE purity/recovery requirements. Fig. 3.2 a) shows the scatter plot of those materials that show $r_{max} \geq 110.25$ (shown as green markers) and those that do not (shown as red markers). From Fig. 3.2 a), it is clear that there is a clear clustering of green and red markers. In order to find a value of selectivity which separates these two regions with the best possible accuracy, a linear discriminant analysis was performed. This resulted in the value of $\alpha_H = 13$ and it is shown in thick black dashed line in Fig. 3.2 a). Also as seen in Fig. 3.2 a), the bulk of the markers which have been tagged as red have Henry selectivities less than 13. The value of $\alpha_H = 13$ compares well with the observation made by Khurana and Farooq that the minimum selectivity for an adsorbent to provide 95 % purity and 90 % recovery is ≈ 10 [1]. The scatter plot of r_{max} as a function of H_{CO_2} and H_{N_2} are plotted and shown in Fig. 3.2 b). Overall it can be seen that r_{max} increases with the increasing selectivity. While this is a general trend, this observation has to be considered with caution. Figure. 3.2 c) and d) show the trends of $En_{min,scaled}$ and WC_{CO_2} respectively on a plot of H_{CO_2} vs H_{N_2}. The black markers refer to the top performing adsorbents which had $En_{min,scaled} \leq 145$ kWh$_e$/tonne. The low values of energy tend to occur at higher selectivities. For a clear colour gradient in Fig. 3.2 c), only adsorbents which had $En_{min,scaled} \leq 180$ kWh$_e$/tonne are plotted and the corresponding WC_{CO_2} are shown in Fig. 3.2 d).

In the next two subsections, the effects of two key adsorbent characteristics viz., the selectivity

and heat of adsorption are compared with the performance indicators predicted from the BAAM. This is done to understand the key material properties affecting the process performance and also to bridge the gap between the material and process properties.

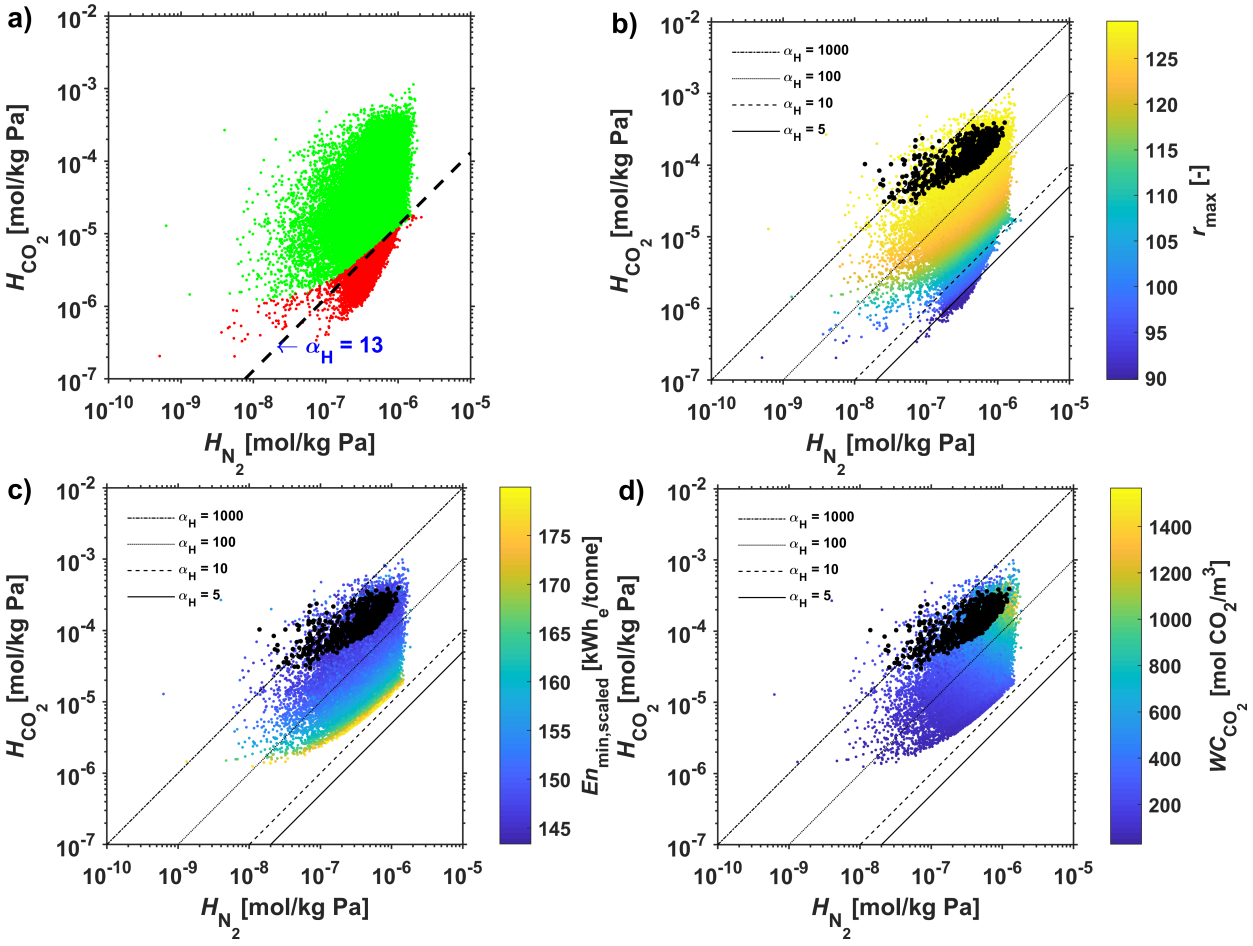

Figure 3.2: Plots showing the distribution of hZEOs. a) Green markers correspond to the adsorbents that met $Pu_{CO_2} - Re_{CO_2}$ constraints and the red markers correspond to those that did not satisfy based on the BAAM's predictions. Black dashed line denotes the locus of constant selectivity line of 13 that provides the best classification of the materials that achieve the target purity and recovery. Plots b), c) and d) provide the trends of r_{max}, $En_{min,scaled}$ and WC_{CO2}, respectively. The black markers represent the adsorbent with $En_{min,scaled} \leq 145$ kWh$_e$/tonne.

3.2.2 Effects of selectivity on the process performance

The selectivity has been arguably the most widely used screening metric to assess the adsorbent performance [34]. In this study, the Henry selectivities of the adsorbents are compared with the BAAM's performance indicators to understand the relationships between them. In the

previous section, the Henry selectivity of 13 was shown to be distinguishing metric in finding an adsorbent satisfying purity-recovery constraints. The Henry selectivity of each of the adsorbents was calculated based on Eq. 3.5 at 298.15 K. For irregularly shaped distributions as with our case, box plots provide useful means to compare the characteristics of the performance indicators over different ranges of selectivities. In each of the box plots in Fig. 3.3, the bottom edge, the central red mark and the top edge in any box correspond to 25th, 50th and 75th percentiles, respectively. The whiskers extend to the most extreme data points in either direction with '+' symbol indicating if it is an outlier.

It has been shown in the literature that the adsorbent with selectivity less than 10 is considered to be the worst performing material [1]. The first key observation from Fig. 3.3 a) is that all the adsorbents with $\alpha_{\mathrm{H}} \leq 10$ have $r_{\max} \leq 110.25$ hence proving that $r_{\max}$ metric is in-line with that what is shown in the literature. With the increase in selectivity above 10, there is a marked increase in the median value of $r_{\max}$ until a selectivity of 500 and $r_{\max}$ becomes almost constant for values more than 500 as illustrated in Fig. 3.3 a). In fact, there is a huge jump in $r_{\max}$ values moving from 0-10 selectivity range to 10-25, highlighting the effect of increase in selectivity on CO_2 purity and recovery values in the lower ranges of selectivities. For the case of $En_{\mathrm{min,scaled}}$, with increasing selectivity, the average $En_{min,scaled}$ decreases upto a selectivity of 500 and then as with the case of $r_{\max}$, it becomes constant. For selectivities more than 1000, as indicated by the box plot, the maximum value is around 153 $\mathrm{kWh_e}$/tonne which is higher than the minimum value of 147.2 $\mathrm{kWh_e}$/tonne in the selectivity range of 75-100. This again proves that selectivity is not a good predictor of the optimized performance. However, the pronounced effect of selectivity on the performance indicators is seen until a selectivity of 500. It is important to note here that there are no $En_{min,scaled}$ and $WC_{\mathrm{CO_2}}$ values in 0 to 10 selectivity range as $r_{\max} \leq 110.25$. There is a clear trend with respect to $WC_{\mathrm{CO_2}}$ as seen in Fig. 3.3 c), it increases with increase in selectivity up to 500 and decreases moving from 500 to 1000. $WC_{\mathrm{CO_2}}$ goes through a maxima in the 250-500 range as the selectivity varies from 10 to 1000. The analysis with respect to $WC_{\mathrm{CO_2}}$ should be treated with caution as it is not a direct predictor of productivity. To conclude, there is not a clear relationship between the selectivity and the minimum energy for higher values of the selectivities. To further illustrate this, the values of $En_{min,scaled}$ for all the adsorbents that met the purity-recovery constraints are plotted in Fig. 3.4. It is rather evident that the selectivities of the top performing adsorbents, as shown by the positions of black markers, range from ≈ 180 to 1000. This indicates clearly that beyond a certain value of selectivity, the ability of this metric to predict the energy consumption is poor.

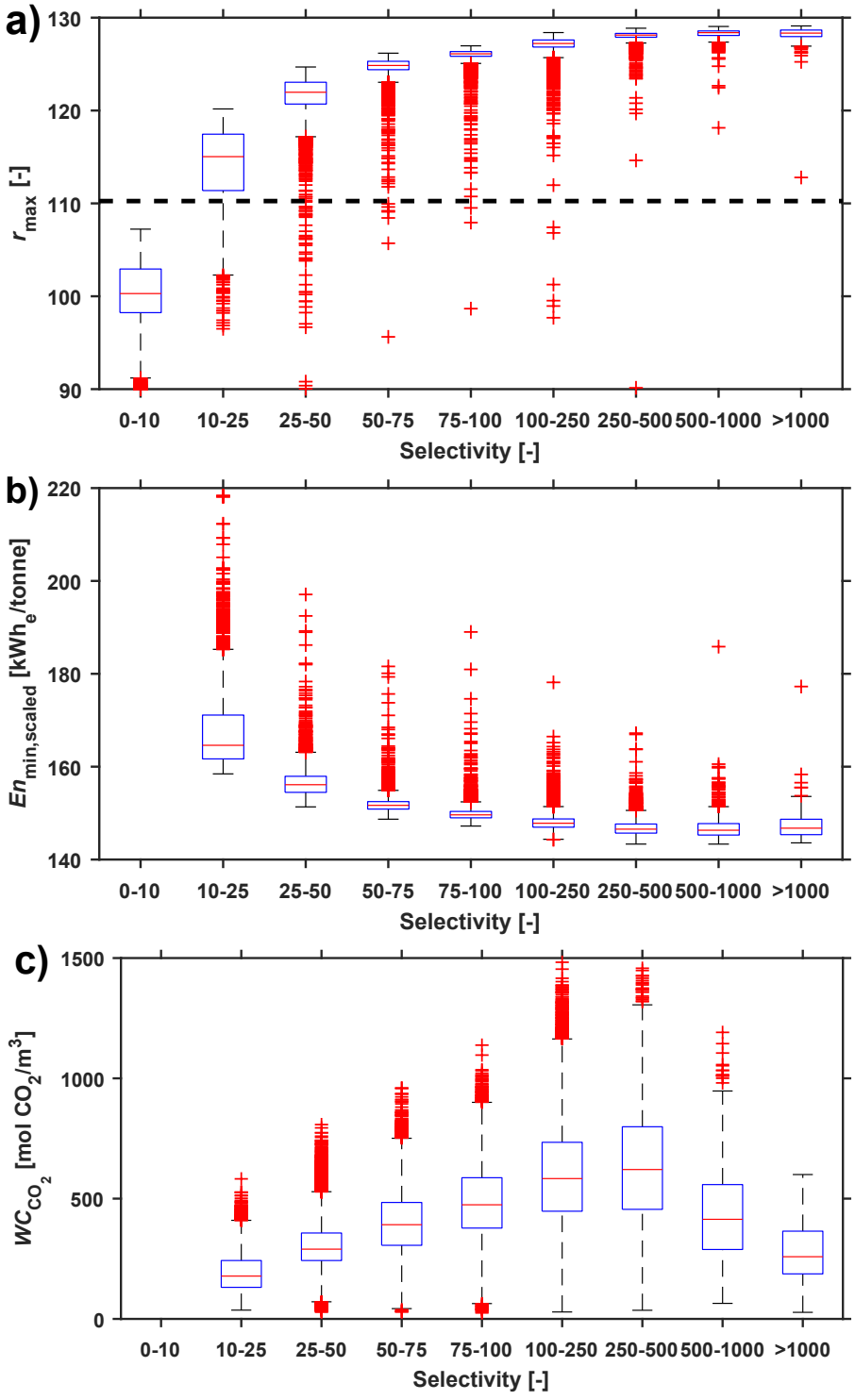

Figure 3.3: Box plots showing the effects of the Henry selectivity on a) $r_{\max}$, b) $En_{\min,\text{scaled}}$, and c) WC_{CO_2}.

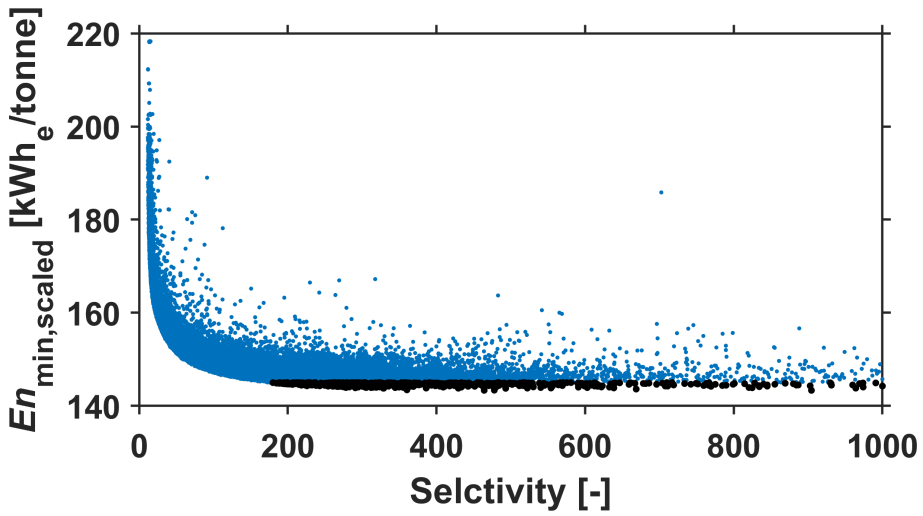

Figure 3.4: Relationship between the selectivity and the energy penalty.

3.2.3 Effects of heat of adsorption on the process performance

In this sub-section, the relationship between the heats of adsorption of CO_2 and N_2 with the process performance indicators are analysed. Fig. 3.5 shows the scatter plots of r_{max}, $En_{min,scaled}$ and WC_{CO_2} as a function of the heats of adsorption of CO_2 and N_2. It is evident that the adsorbents explored in the CCMDB fall with in a clear boundary of ΔH_{CO_2} and ΔH_{N_2}. From Fig. 3.5, it is clear that there is no clear relationship between ΔH_{N_2} and any of the performance indicators. However, there is a clear gradient in the case of ΔH_{CO_2} as shown in Fig. 3.5 b). The plot also shows that a minimum CO_2 heat of adsorption of 20 kJ/mol is required to meet the purity/recovery limits. Higher CO_2 purities and recoveries are achieved for higher heat of adsorption of CO_2 as seen in Fig. 3.5 a). This is also evident from the positions of the black markers in Fig. 3.5. The lowest energy consumption corresponds to ΔH_{CO_2} in the range of $\approx$ 32 to 42 kJ/mol and $\Delta H_{N_2} < 17$ kJ/mol. These observations are in line with the Maring and Webley [23].

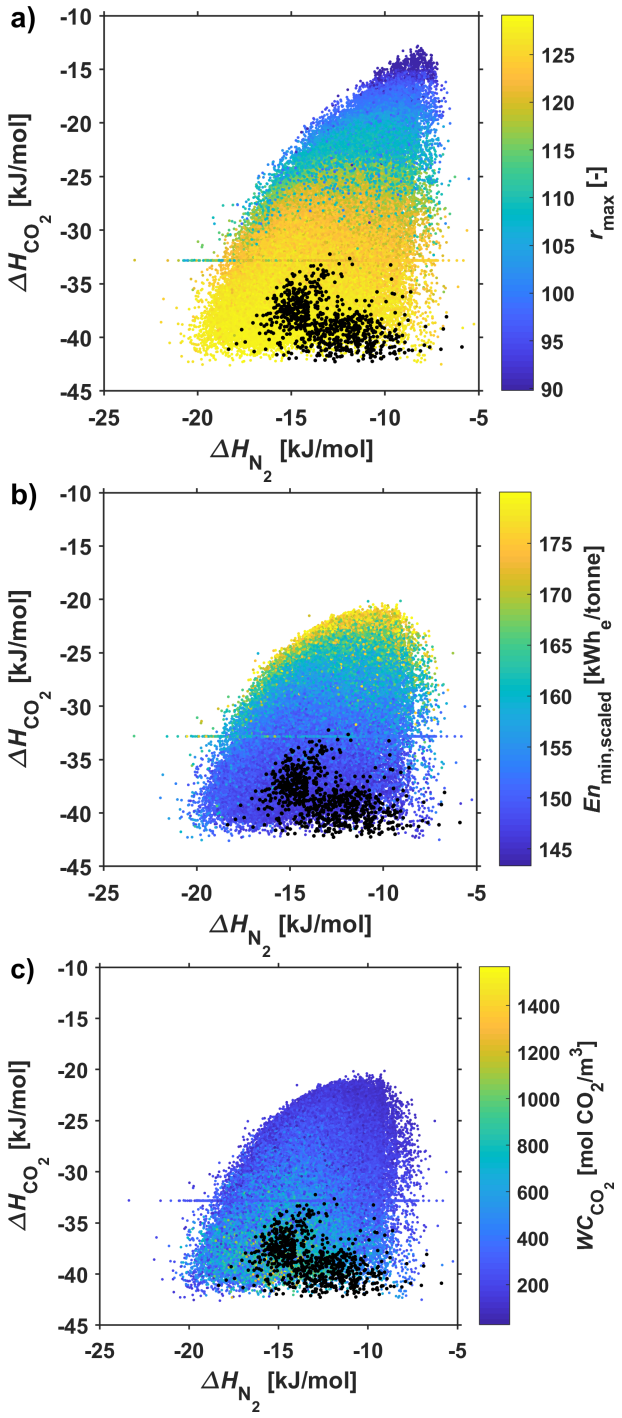

Figure 3.5: Scatter plots of $\Delta H_{\mathrm{CO_2}}$ vs $\Delta H_{\mathrm{N_2}}$ giving the trends of a) $r_{\max}$, b) $En_{\mathrm{min,scaled}}$, and c) $WC_{\mathrm{CO_2}}$.

3.3 Validation of BAAM using detailed model

The screening of the CCMDB has now been performed using the BAAM. It is very important to note that this dataset, in its entirety, can be considered as a test set since the BAAM has not seen it during the calibration. Hence, it is important to verify the predictions of the BAAM using the detailed model. This is the key focus of this section.

The cumulative distribution of the minimum energies of the hMOFs which had $r_{\max} \geq 110.25$ are given in Fig. 3.6 a). The shaded portion on either side of the distribution indicates the $\pm$ 15 % uncertainty of the BAAM. As observed from the plot of cumulative distribution, $\approx$ 50 % of the adsorbents screened have $En_{\text{min,scaled}}$ less than 153 kWh_e/tonne. To put this in perspective, $En_{\text{min,scaled}}$ values of UTSA-16 and Zeolite 13X, examples of two important adsorbents as described in Chapter 2, were plotted along with the cumulative distribution plot and shown in Fig. 3.6 b).

A total of 0.55 % of total materials which translates to nearly 653 adsorbents of total materials considered were found to have $En_{\text{min,scaled}}$ less than that of UTSA-16 (144.88 kWh_e/tonne). Nearly 9500 materials were found to have $En_{\text{min,scaled}}$ less than that of commercialized Zeolite 13X (146.93 kWh_e/tonne). These results are indeed promising as it provides a set of materials that can potentially outperform the current benchmark adsorbents. However, it is also important to exercise caution as the practicality of the synthesis of these materials has not been demonstrated. Nonetheless this analysis gives us great insights about the some of the key isotherm characteristics and helps us validate BAAM with the detailed optimization studies. The adsorbent h8297545 was found to have the lowest $En_{\text{min,scaled}}$ of 143.32 kWh_e/tonne with the corresponding working capacity, WC_{CO_2} of 1057.11mol CO_2/m^3. The single component isotherms of CO_2 and N_2 of the top three adsorbents are shown in Fig. 3.7 along with those of Zeolite 13X and UTSA-16 for comparison. The SSL fitting parameters of these adsorbents are provided in the Table F.1. It is evident from the isotherm plots that h8297545 has lowest CO_2 and N_2 capacities of the five adsorbents illustrated in Fig. 3.7 in the pressure range of 0 to 1 bar. h8297545 has similar CO_2 isotherm as that of UTSA-16 but lower N_2 capacity. All the top three adsorbents have N_2 capacities lower than that of UTSA-16. This leads us to important conclusions about the ideal CO_2 and N_2 isotherms that an adsorbent with minimum energy consumption should possess. h8297545 has the lowest N_2 adsorption capacity which reinforces the need for accounting for the effect of N_2 adsorption during adsorbent screening [2, 23]. The current trend of improving the CO_2 capacity alone while synthesizing an adsorbent doesn't prove to be helpful in an actual VSA process. Further efforts have to be put in reducing the N_2 adsorption.

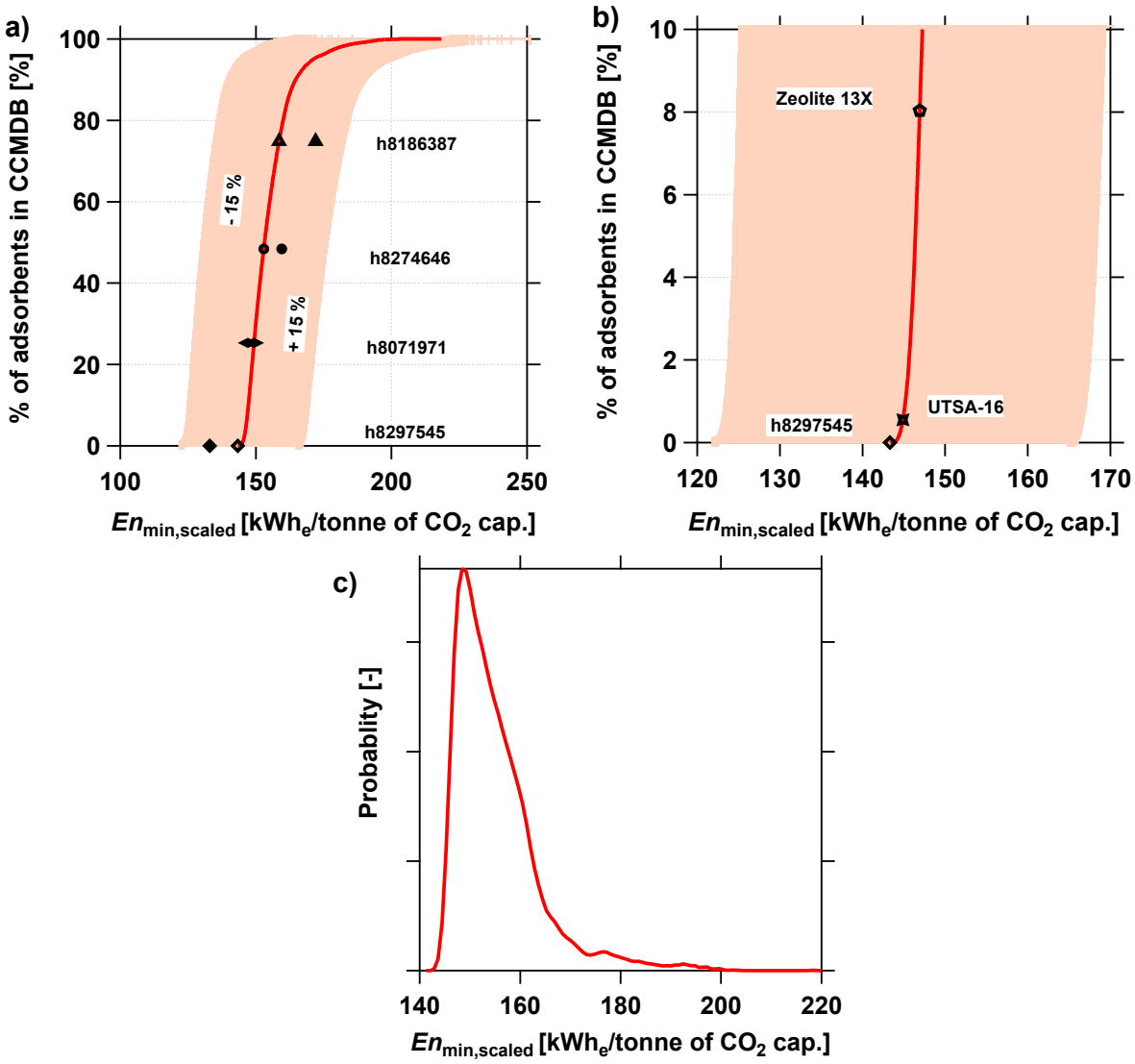

Figure 3.6: Distribution plots of minimum energies of the predicted zeolites which satisfied $Pu_{CO_2} - Re_{CO_2}$ constraints. a) cumulative distribution plot of the % of adsorbents against the energy consumption. The open and closed markers represent the detailed model optimizations and BAAM predictions, respectively. b) Magnified version of the cumulative distribution showing the locations of Zeolite 13X and UTSA-16. c) Probability density function of the minimum energies.

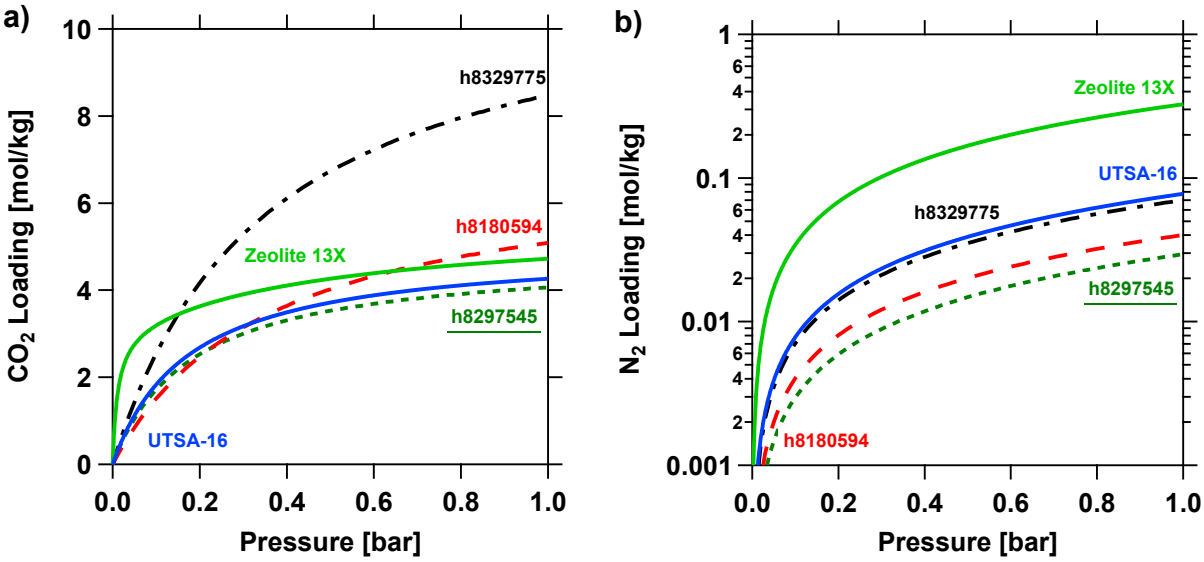

Figure 3.7: Pure-component isotherms of a) CO_2 and b) N_2 at 298.15 K for the top three adsorbents with lowest $En_{\text{min,scaled}}$ values plotted along with UTSA-16 and Zeolite 13X.

To test the effectiveness of BAAM in predicting the minimum energy values, adsorbents close to each of 0 %, 25 %, 50 %, 75 % and 100 % on the cumulative distribution curve as shown in the Fig. 3.6 a) were chosen. The adsorbents that were chosen for the study are depicted as open markers in Fig. 3.6 a) and the isotherm parameters of these adsorbents are provided in the Appendix F. The detailed energy - productivity optimization was performed to compute the minimum energy values of these adsorbents under the optimized conditions. Genetic algorithm (GA) was employed to run the rigorous optimizations with the detailed models to minimize the energy consumption and maximize productivity under the constraints of CO_2 purity and recovery of 95 % and 90 %, respectively. A detailed description of the detailed model is given in Chapter 2 and Appendix C. Three step times, low and intermediate pressures and feed velocity were the six decision variables of the detailed model. The bounds for each of the decision variables are as follows: $20 \leq t_{\text{ADS}}$ [s] ≤ 200, $20 \leq t_{\text{BLO}}$ [s] ≤ 200, $20 \leq t_{\text{EVAC}}$ [s] ≤ 200, $0.04 \leq P_{\text{INT}}$ [bar] ≤ 0.45, $0.03 \leq P_{\text{LOW}}$ [bar] ≤ 0.3, $0.1 \leq v_{\text{feed}}$ [m/s] ≤ 2. The parameters used in the detailed model for the process simulations are given in the Table A.3. The GA was run for 25 generations and the population size of 144 was chosen. In order to avoid GA getting stuck on a local minima, first the operating regions were divided into 8 sub-regions and the samples obtained after 10 generations were used to seed the GA.

The summary of the predicted minimum energies after the detailed model optimizations are given along with the BAAM's predictions for the 7 adsorbents that were chosen for the study in Table 3.1. As observed from the Table 3.1, the BAAM was able to predict the minimum energy values of 6 out of 7 adsorbents under 8 % accuracy. For the cases of h8180594 and h8071971, the

Table 3.1: Results of detailed model optimizations along with the BAAM's predictions.

FrameWork Name	CDF	r_{max} [-]	$En_{min,scaled}$ [BAAM] [kWh_e/tonne CO_2 cap.]	En_{min} [Detailed Model] [kWh_e/tonne CO_2 cap.]	% diff.	WC_{CO_2} [mol CO_2/m^3]
h8297545	0.001	129.05	143.32	133.02	7.75	1057.11
h8329775	0.002	128.86	143.33	135.11	6.08	1370.62
h8180594	0.003	128.84	143.37	145.19	1.26	1131.31
h8071971	25.286	126.56	149.31	147.08	1.52	426.39
h8274646*	48.425	123.52	152.88	159.54	4.17	288.12
h8186387	74.835	120.38	158.53	172.02	7.84	291.32
h8081405	97.774	111.89	180.02	NA	NA	89.43

differences were as low as under 2%. It is important to note here again that we are comparing the BAAM's result which was obtained less than a second to the detailed optimization result which took more than a day to converge. The predicted minimum energy values from the detailed model were plotted in Fig. 3.6 a) as the closed markers. Importantly, h8186387 was shown to satisfy 95-90 requirement and the predicted minimum energy was within 8%. The validation exercise discussed here demonstrates the ability of BAAM to be an excellent tool to minimize the workload of the detailed process optimizers. The ability to predict the energy consumption within 8 % of detailed model calculations is indeed encouraging. Appendix G provides the summary of the performance indicators along with the selectivites of top 50 h-ZEOs from the screening of CCMDB.

3.4 In pursuit of the ideal adsorbent

As summarized in the previous section, the lowest $En_{\text{min,scaled}}$ from screening close to hundred thousand materials turned out to be 143.32 kWh_e/tonne. This leads us naturally to wonder what would be the CO_2-N_2 isotherms of an ideal adsorbent with the least possible PSA energy consumption. To answer this question and also to understand the trends of r_{max} and $En_{\text{min,scaled}}$ for a diverse range of adsorbents, a parametric study was performed using BAAM on the hypothetical adsorbents generated from the non-linearity plot (NLP). Rajagopalan et al. constructed the NLP to elucidate the effect of N_2 adsorption on the vacuum swing adsorption (VSA) process [61]. For the purpose of illustration of the NLP, consider any of the plots in Fig. 3.2, the x-axis and y-axis correspond to N_2 and CO_2 equilibrium constants with reference to that of corresponding equilibrium constants of Zeolite 13X at 298.15 K. The distinctive feature of the NLP allows us to generate hypothetical adsorbents by varying the non-linearities of CO_2 and N_2 isotherm, as given by the b values, with reference to Zeolite 13X. The density of all the adsorbents in this study are taken to that of Zeolite 13X pellet density. $q_{\text{sb,CO}_2}$ and $q_{\text{sb,N}_2}$ of all the hypothetical adsorbents were taken to be that of the saturation ladings of Zeolite 13X.

The x and y-axes of the NLP, each varying from 0 to 5, were discretized into 50 subintervals of equal length of 0.1 which resulted in a total of 2601 adsorbents for the analysis. BAAM was run on these materials with the same operating conditions as described previously. r_{max} and $En_{\text{min,scaled}}$ outputs of the BAAM are plotted as contours in Figs. 3.8 a) and b). Figures 3.8 c) and d) provide the respective zoomed in versions in the region of 0 to 1 for which a finer grid step size of 0.01 was used for clarity. It is important to note that $En_{\text{min,scaled}}$ values are plotted only for the adsorbents with $r_{\text{max}} \geq 110.25$. For a fixed CO_2 affinity, lower the N_2 affinity, higher the r_{max} (Figs. 3.8 a) and c) and lower the $En_{\text{min,scaled}}$ (Figs. 3.8 b) and d)). This can be attributed to the the additional energy that needs to be spent to remove N_2 for higher N_2 adsorption which also results in lower product purity resulting in lower r_{max}. And, for a fixed N_2 affinity, increase in CO_2 affinity increases r_{max} drastically for lower values of CO_2 affinities and flattens out after reaching a certain value of CO_2 affinity which is different for different values of N_2 affinities as clearly evident in Figs. 3.8 a) and c). For the case of $En_{\text{min,scaled}}$, for a fixed value of b_{N_2}, the energy decreases rapidly as CO_2 affinity increases at lower values of b_{CO_2}. Then it reaches a minimum and the energy values increase beyond a certain value. This is very interesting observation as in indicates that increasing CO_2 adsorption beyond a certain value can infact be detrimental. Following two interesting observations clearly standout in Figs. 3.8 b) and d): a) The lowest $En_{\text{min,scaled}}$ is when $b_{N_2} = 0$, and b) At $b_{N_2} = 0$, the energy goes through a minimum which shows that an increase in the affinity or the non-linearity of CO_2 becomes detrimental to the process beyond a certain value. So, if we were to synthesize an

adsorbent with zero N_2 adsorption, there exists a unique value of CO_2 affinity which gives the best possible minimum energy. This is due to the fact that higher CO_2 affinity would mean higher energy required to remove the adsorbate from the adsorbent.

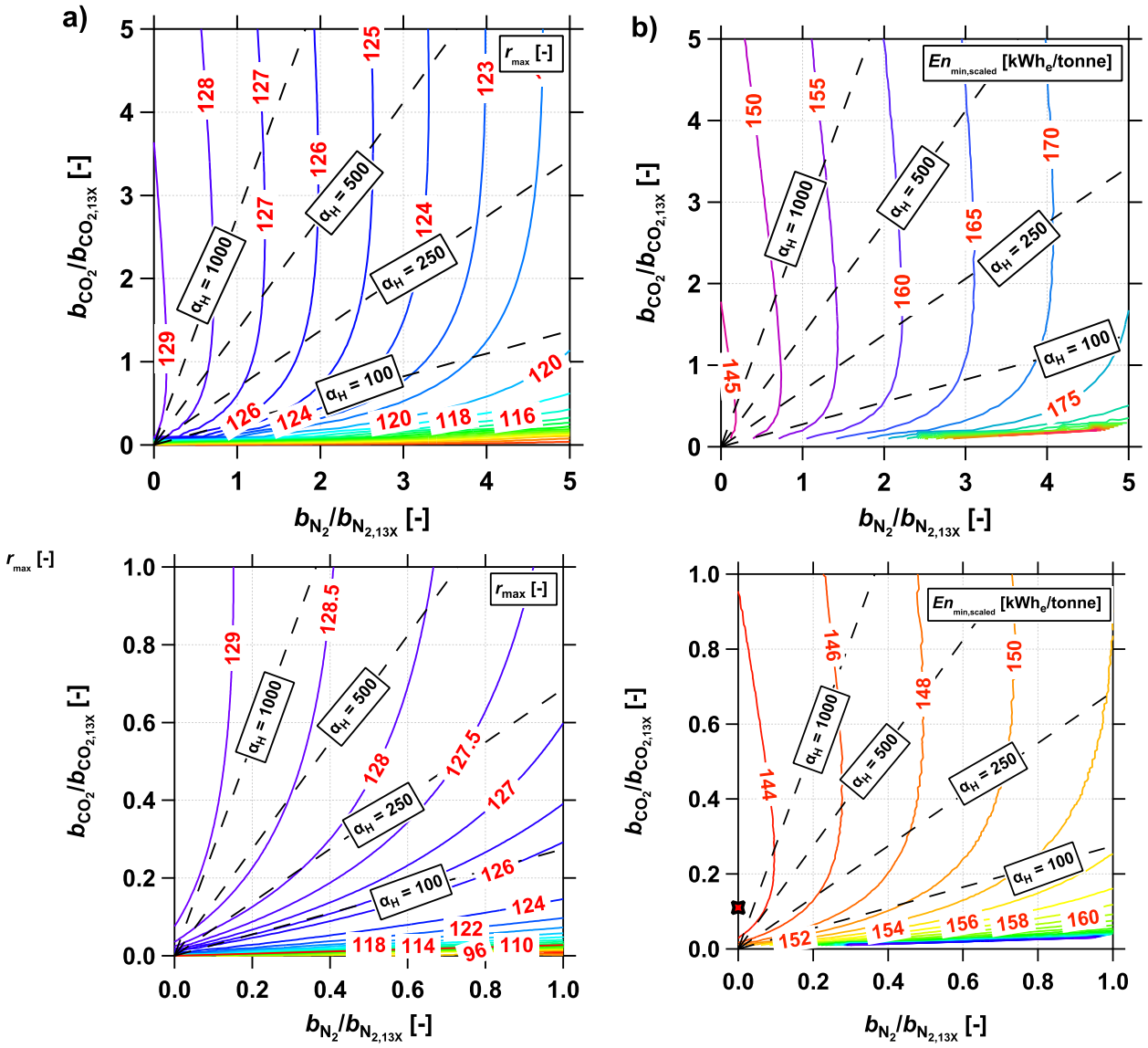

Figure 3.8: Contours of a) $r_{\max}$ and b) $En_{\min,\text{scaled}}$ of the hypothetical adsorbents generated from the NLP using BAAM. c) and d) provide the magnified versions of respective contours in the range of 0 to 1.

Now that zero N_2 adsorption case was shown to have the least energy consumption in a P/VSA process. A parametric study was again performed but this time by varying $b_{CO_2}/b_{CO_2,13X}$ and q_{sb,CO_2}. In this case, q_{sb,CO_2} was varied from 0.5 to 10 in steps of 0.5 resulting in 20 distinct points. As previously, $b_{CO_2}/b_{CO_2,13X}$ was varied from 0 to 5 in steps of 0.1. This grid resulted

in a total of 1020 adsorbents. And, BAAM was run again on these set of adsorbents to plot the contours of $En_{\text{min,scaled}}$ as a function of $b_{CO_2}/b_{CO_2,13X}$ and q_{sb,CO_2} as shown in Fig. 3.9 a). As expected, lowest $En_{\text{min,scaled}}$ is when q_{sb,CO_2} is high and lower b_{CO_2} indicating a linear CO_2 isotherm. The lowest $En_{\text{min,scaled}}$ is also around 142 kWh_e/tonne which is also possibly the best an adsorbent described by the Type 1 isotherm can do for the fixed 4-Step LPP cycle as predicted by BAAM. The predicted minimum energy from this parametric study is only 1 to 2 kWh_e/tonne lower than that of what we saw in the CCMDB analysis. This opens up the opportunity to look into other shapes of the isotherms not restricting only to Langmuirain. In this regard, S-shaped isotherms have shown good potential in delivering higher CO_2 purities and recoveries at lower energy consumption [62]. The modeling of the isotherms get complex and in such scenarios, the potential of discrete data should be looked into and studied in detail [63].

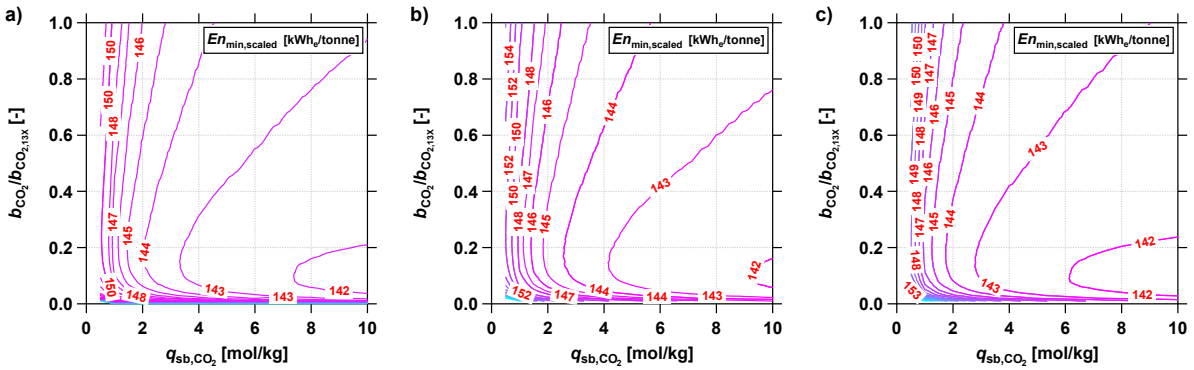

Figure 3.9: $En_{\text{min,scaled}}$ contours for the case of zero N_2 adsorption with the particle density a) ρ =1130 kg/m^3, b) ρ =904 kg/m^3 (20% lower) and c) ρ =1356 kg/m^3 (20% higher).

All the simulations, as described above, were done for a fixed solid particle density ρ. It is also important to understand the effect of density on the process performance. The same parametric study was then repeated for 20 % lower and higher solid density and the respective resulting contours are shown in Figs. 3.9 b) and c). There is a slight improvement in the energy penalty for higher ρ for a fixed q_{sb,CO_2} as seen in Fig. 3.9 c).

3.5 Conclusion

In this chapter, BAAM's potential to screen the CCMDB of 118,149 adsorbents was illustrated and it was found that 107,225 of them have the ability to satisfy CO_2 purity and recovery constraints when employed in a P/VSA process. The screening time per adsorbent was almost instantaneous and the whole process was completed in 97 minutes on a 24 core workstation. This ability to screen the adsorbents with an accuracy of 87 % has been the best feature which makes

BAAM to stand out from the other existing screening metrics which require similar computation efforts and time. Then, the detailed model optimization studies were performed for a set of 7 adsorbents and it was observed that the BAAM's predictions of minimum energy values were within 10 % bound as that of corresponding minimum energy values from the detailed model. A total of 653 predicted zeolites were found in this study which could deliver higher CO_2 purities and recoveries with the lower energy consumption as that of UTSA-16 and these need to be studied in detail with the detailed process optimization. The effects of selectivity and the heat of adsorption of CO_2 and N_2 were discussed in detail. It was found that before resorting to any of the screening techniques, if an adsorbent has Henry selectivity of less than 10, it could be outright removed from further analysis. There were no correlations between the heat of adsorption of N_2 with the performance indicators. A higher heat of adsorption of CO_2 favor higher CO_2 purity and recovery with the least energy consumption. A parametric study using BAAM was performed in this study to look for ideal characteristics of an adsorbent with the least energy consumption. An adsorbent with zero N_2 adsorption was shown to be the one delivering higher purities and recoveries with the least energy consumption. In this regard, there exists a finite CO_2 isotherm above which it becomes detrimental to the process.

Chapter 4

Concluding Remarks

4.1 Conclusions

The thesis dealt with modeling, analysis and applications of BAAM, a simplified proxy model, for rapid and efficient screening of high performing adsorbents for post-combustion CO_2 capture. The first part of the thesis provided a thorough analysis of BAAM and the development of simplified metrics for computing key performance indicators. The second part of the thesis presented its potential to screen CCMDB, an exhaustive database of hundreds and thousands of zeolites and ZIFs, created and maintained by the University of California, Berkley.

Chapter 2 detailed on the mathematical modeling and analysis of BAAM for a 4-step VSA cycle with LPP. BAAM's modeling framework was adopted from the works of Maring and Webley [23] and extended to a more complex process configuration in this study. The modeling equations were based on a "well-mixed" isothermal - batch adsorber system which simplified the overall design of the adsorption process. The results of BAAM allowed us to visualize the transitions of different steps of the 4-step cycle with LPP on CO_2 and N_2 isotherm plots by just solving ODEs as opposed to the numerically intensive stiff PDEs. Then, the BAAM's results were validated by performing parametric study with the detailed model. It was concluded that BAAM could replicate the detailed model only under specific operating conditions, i.e., when the column is completely saturated with the feed conditions and other key assumptions of BAAM were enforced upon. BAAM was initially tested upon using a set of four adsorbents which Rajagopalan et.al considered in his study [2] and an observation was made showing the potential of BAAM in using as a screening tool. Using the optimized results a total of 75 adsorbents [1], a purity - recovery classifier based on BAAM was built. In doing so, the Euclidean maximum distance from the origin to the Pareto curve, $r_{\max}$, was taken as a proxy to the combined CO_2 purity - recovery. A linear discriminant analysis was performed which resulted in $r_{95-90} = 110.25$

as the classification metric with an accuracy of 87.3 %. Then, a linear relationship relating the minimum energy predicted by the BAAM to that of detailed model was developed. It is given by $En_{\text{min,scaled}} = 1.1446En_{\text{min,BAAM}} + 66.53$. It was seen that minimum energies of 53 % of the 35 adsorbents were predicted within 10 % and that of 83 % was predicted within 15% of the values from the detailed model. Then, the high performing adsorbents were ranked based on low minimum energy and high working capacity. BAAM was then applied on an experimental NIST database to show the efficacy of BAAM in screening a large database. A total of 757 DOIs and 1540 unique adsorbents were screened for the best candidates. UTSA-16 and Zeolite 13X stood out as the best adsorbents with the minimum energies 144.88 kWh_e/tonne and 146.93 kWh_e/tonne, respectively. The chapter concluded with BAAM's merits and demerits.

Chapter 3 illustrated the applications of BAAM for a large scale adsorbent screening. A total of 118,149 computationally predicted zeolites were screened from CCMDB of which 107,225 were predicted to satisfy the purity-recovery constraints when employed in a 4-step VSA with LPP for the post-combustion CO_2 capture. The trends of $r_{\max}$, $En_{\text{min,scaled}}$ and WC_{CO_2} were explored as a function of the Henry constants of CO_2 and N_2 for all the predicted zeolite structures. A selectivity of 13 was found to be classifying metric which distinguishes if a material could meet the purity-recovery targets. Then, the effects of selectivity and heat of adsorption to predict the process performance were studied. The former analysis indicated that beyond a certain value of selectivity, the ability of the selectivity metric to predict the energy consumption should be treated with care. With the latter analysis indicating that the lowest energy consumption corresponds to ΔH_{CO_2} in the range of $\approx$ 32 to 42 kJ/mol and $\Delta H_{N_2} < 17$ kJ/mol. Then, the results of BAAM were further validated by detailed model process optimization studies for a set of 7 adsorbents and the predictions were within 8 % accuracy for 6 out of 7 adsorbents. Then, a parametric study was performed using NLP to look for the characteristics of an ideal adsorbent. It was found that a material with zero N_2 was found to have the minimum energy. For the case of zero N_2 adsorption, it was observed that increasing the CO_2 affinity beyond a certain value could be detrimental to the process performance. The minimum energy was evaluated at 142.58 kWh_e/tonne.

4.2 Outlook

Over the course of the thesis work, 119,768 adsorbents [1,2,35,47] consisting of a mix of zeolites, ZIFs, MOFs and activated carbons were screened for their potential for a VSA based post-combustion CO_2 capture process. If the screening processes were carried out using the detailed model on a 24 core workstation, it would have taken us close to 119,768 days, assuming the average optimization time per adsorbent is $\approx$ 1 day. On the other hand, BAAM could screen

each of the adsorbents under a second with a reasonable accuracy. BAAM seems to show excellent promise as a potential tool to screen very large databases such as the ones described in this work.

The flexibility that the BAAM provides, makes it appealing for wide-ranging applications. These are some of the future works that we propose to do:

1. **Extension of BAAM to more complex process configurations**: This would help us evaluate adsorbent performance in a different process set-up and study how an adsorbent ranking varies based on the choice of process configuration.
2. **Applications of BAAM for different gas separations**: The framework of selecting an adsorbent using BAAM for CO_2 capture application, as described in this work, could now be extended for other gas separations involved in hydrocarbon refining, pharmaceutical applications and other industrial separations.
3. **Different choice of isotherm model**: Incorporating discrete isotherm and S-shaped isotherm models in BAAM would help us to look for more promising adsorbents with lower energy consumption for a VSA process specific to CO_2 capture application.
4. **Screening of other large databases**: BAAM could now be used to screen other large databases such as Computation-ready, experimental (CoRE) MOF database and hypothetical MOFs database for CO_2 capture applications.

Bibliography

[1] M. Khurana and S. Farooq, "Adsorbent screening for postcombustion CO_2 capture: a method relating equilibrium isotherm characteristics to an optimum vacuum swing adsorption process performance," *Ind. Eng. Chem. Res.*, vol. 55, no. 8, pp. 2447–2460, 2016.

[2] A. K. Rajagopalan, A. M. Avila, and A. Rajendran, "Do adsorbent screening metrics predict process performance? A process optimisation based study for post-combustion capture of CO_2," *Int. J. Greenh. Gas Control*, vol. 46, pp. 76–85, 2016.

[3] R. Haghpanah, A. Majumder, R. Nilam, A. Rajendran, S. Farooq, I. A. Karimi, and M. Amanullah, "Multiobjective optimization of a four-step adsorption process for post-combustion CO_2 capture via finite volume simulation," *Ind. Eng. Chem. Res.*, vol. 52, no. 11, pp. 4249–4265, 2013.

[4] D. M. Etheridge, L. Steele, R. L. Langenfelds, R. Francey, J.-M. Barnola, and V. Morgan, "Natural and anthropogenic changes in atmospheric CO_2 over the last 1000 years from air in antarctic ice and firn," *J Geophys Res Atmos*, vol. 101, no. D2, pp. 4115–4128, 1996.

[5] E. Dlugokencky and P. Tans, *Monthly CO_2 measurements from 1959 to 2017*. NOAA/ESRL, 2017.

[6] C. P. Morice, J. J. Kennedy, N. A. Rayner, and P. D. Jones, "Quantifying uncertainties in global and regional temperature change using an ensemble of observational estimates: The hadcrut4 data set," *J Geophys Res Atmos*, vol. 117, no. D8, 2012.

[7] B. Smit, J. A. Reimer, C. M. Oldenburg, and I. C. Bourg, *Introduction to carbon capture and sequestration*. World Scientific, 2014.

[8] C. W. Team, R. K. Pachauri, and L. Meyer, "IPCC, 2014: climate change 2014: synthesis report. Contribution of Working Groups I," *II and III to the Fifth Assessment Report of the intergovernmental panel on Climate Change. IPCC, Geneva, Switzerland*, vol. 151, 2014.

[9] D. Lüthi, M. Le Floch, B. Bereiter, T. Blunier, J.-M. Barnola, U. Siegenthaler, D. Raynaud, J. Jouzel, H. Fischer, K. Kawamura, *et al.*, "High-resolution carbon dioxide concentration record 650,000–800,000 years before present," *Nature*, vol. 453, no. 7193, p. 379, 2008.

[10] *Global Warming of 1.5 °C (SR15)*. Intergovernmental Panel on Climate Change (IPCC), https://www.ipcc.ch/sr15/, 2018.

[11] *Katowice Climate Change Conference December 2018*. https://unfccc.int/katowice, 2018.

[12] B. Metz, O. Davidson, H. De Coninck, M. Loos, and L. Meyer, "IPCC, 2005: IPCC special report on carbon dioxide capture and storage. Prepared by Working Group III of the Intergovernmental Panel on Climate Change," *Cambridge, United Kingdom and New York, NY, USA*, vol. 442, 2005.

[13] *Tracking Clean Energy Progress*. https://www.iea.org/tcep/, International Energy Agency (IEA), 2018.

[14] *The Global Status of CCS-2018*. Global CCS Institute, 2018.

[15] *BD3 Status Update: March 2018.* https://www.saskpower.com/about-us/our-company/blog/2018/05/bd3-status-update-march-2018, SaskPower, 2018.

[16] *Quest Carbon Capture and Storage.* Shell Canada, https://www.shell.ca/en_ ca/about-us/projects-and-sites/quest-carbon-capture-and-storage-project.html, 2018.

[17] G. T. Rochelle, "Amine scrubbing for CO_2 capture," *Science*, vol. 325, no. 5948, pp. 1652–1654, 2009.

[18] D. Ruthven, *Principles of Adsorption and Adsorption Processes.* Wiley-Interscience publication, Wiley, 1984.

[19] *VeloxoTherm Process.* Inventys, http://inventysinc.com/technology/, 2011.

[20] S. Krishnamurthy, V. R. Rao, S. Guntuka, P. Sharratt, R. Haghpanah, A. Rajendran, M. Amanullah, I. A. Karimi, and S. Farooq, "CO_2 capture from dry flue gas by vacuum swing adsorption: a pilot plant study," *AIChE J.*, vol. 60, no. 5, pp. 1830–1842, 2014.

[21] D. M. D'Alessandro, B. Smit, and J. R. Long, "Carbon dioxide capture: prospects for new materials," *Angew. Chem. Int. Ed.*, vol. 49, no. 35, pp. 6058–6082, 2010.

[22] A. Samanta, A. Zhao, G. K. Shimizu, P. Sarkar, and R. Gupta, "Post-combustion CO_2 capture using solid sorbents: a review," *Ind. Eng. Che. Res.*, vol. 51, no. 4, pp. 1438–1463, 2011.

[23] B. J. Maring and P. A. Webley, "A new simplified pressure/vacuum swing adsorption model for rapid adsorbent screening for CO_2 capture applications," *Int. J. Greenh. Gas Control*, vol. 15, pp. 16–31, 2013.

[24] M. Bui, C. S. Adjiman, A. Bardow, E. J. Anthony, A. Boston, S. Brown, P. S. Fennell, S. Fuss, A. Galindo, L. A. Hackett, *et al.*, "Carbon capture and storage (CCS): the way forward," *Energ. Environ. Sci.*, vol. 11, no. 5, pp. 1062–1176, 2018.

[25] J. Wilcox, *Carbon capture.* Springer Science & Business Media, 2012.

[26] P. A. Webley, "Adsorption technology for CO_2 separation and capture: a perspective," *Adsorption*, vol. 20, no. 2-3, pp. 225–231, 2014.

[27] S. Sircar, "Pressure swing adsorption," *Ind. Eng. Che. Res.*, vol. 41, no. 6, pp. 1389–1392, 2002.

[28] D. Ruthven, S. Farooq, and K. Knaebel, *Pressure swing adsorption.* Wiley, 1993.

[29] S. L. James, "Metal-organic frameworks," *Chem. Soc. Rev.*, vol. 32, no. 5, pp. 276–288, 2003.

[30] S. Choi, J. H. Drese, and C. W. Jones, "Adsorbent materials for carbon dioxide capture from large anthropogenic point sources," *ChemSusChem*, vol. 2, no. 9, pp. 796–854, 2009.

[31] P. J. Harlick and F. H. Tezel, "An experimental adsorbent screening study for CO_2 removal from N_2," *Microporous Mesoporous Mater.*, vol. 76, no. 1-3, pp. 71–79, 2004.

[32] A. O. Yazaydın, R. Q. Snurr, T.-H. Park, K. Koh, J. Liu, M. D. LeVan, A. I. Benin, P. Jakubczak, M. Lanuza, D. B. Galloway, J. J. Low, and R. R. Willis, "Screening of metal-organic frameworks for carbon dioxide capture from flue gas using a combined experimental and modeling approach," *J. Am. Chem. Soc.*, vol. 131, no. 51, pp. 18198–18199, 2009.

[33] R. Krishna and J. M. van Baten, "A comparison of the CO_2 capture characteristics of zeolites and metal–organic frameworks," *Sep. Purif. Technol.*, vol. 87, pp. 120–126, 2012.

[34] R. Krishna, "Screening metal–organic frameworks for mixture separations in fixed-bed adsorbers using a combined selectivity/capacity metric," *RSC Adv.*, vol. 7, no. 57, pp. 35724–35737, 2017.

[35] L.-C. Lin, A. H. Berger, R. L. Martin, J. Kim, J. A. Swisher, K. Jariwala, C. H. Rycroft, A. S. Bhown, M. W. Deem, M. Haranczyk, *et al.*, "In silico screening of carbon-capture materials," *Nat. Mater.*, vol. 11, no. 7, p. 633, 2012.

[36] A. H. Berger and A. S. Bhown, "Optimizing solid sorbents for CO_2 capture," *Energy Procedia*, vol. 37, pp. 25–32, 2013.

[37] R. Haghpanah, A. Rajendran, and S. Farooq, "CO_2 capture from post-combustion flue gas on a carbon molecular sieve," *American Inst. of Chemical Engineers (AIChE) Annual Meeting, Minneapolis USA*, 2011.

[38] M. F. Hasan, E. L. First, and C. A. Floudas, "Cost-effective CO_2 capture based on in silico screening of zeolites and process optimization," *Phys. Chem. Chem. Phys.*, vol. 15, no. 40, pp. 17601–17618, 2013.

[39] N. Casas, J. Schell, R. Blom, and M. Mazzotti, "MOF and UiO-67/MCM-41 adsorbents for pre-combustion CO_2 capture by PSA: Breakthrough experiments and process design," *Sep. Purif. Technol.*, vol. 112, pp. 34–48, 2013.

[40] K. T. Leperi, R. Q. Snurr, and F. You, "Optimization of two-stage pressure/vacuum swing adsorption with variable dehydration level for postcombustion carbon capture," *Ind. Eng. Chem. Res.*, vol. 55, no. 12, pp. 3338–3350, 2015.

[41] G. N. Nikolaidis, E. S. Kikkinides, and M. C. Georgiadis, "An integrated two-stage P/VSA process for postcombustion CO_2 capture using combinations of adsorbents Zeolite 13X and Mg-MOF-74," *Ind. Eng. Che. Res.*, vol. 56, no. 4, pp. 974–988, 2017.

[42] M. Khurana and S. Farooq, "Integrated adsorbent-process optimization for carbon capture and concentration using vacuum swing adsorption cycles," *AIChE J.*, vol. 63, no. 7, pp. 2987–2995, 2017.

[43] R. Zhao, S. Deng, S. Wang, L. Zhao, Y. Zhang, B. Liu, H. Li, and Z. Yu, "Thermodynamic research of adsorbent materials on energy efficiency of vacuum-pressure swing adsorption cycle for CO_2 capture," *Appl. Therm. Eng.*, vol. 128, pp. 818–829, 2018.

[44] R. Haghpanah, R. Nilam, A. Rajendran, S. Farooq, and I. A. Karimi, "Cycle synthesis and optimization of a VSA process for postcombustion CO_2 capture," *AIChE J.*, vol. 59, no. 12, pp. 4735–4748, 2013.

[45] S. A. Hosseinzadeh Hejazi, L. Estupiñan Perez, K. N. Pai, A. Rajendran, and S. M. Kuznicki, "Single-and dual-stage high-purity oxygen production using silver-exchanged titanosilicates (ag-ets-10)," *Ind. Eng. Chem. Res.*, p. In Press, 2018.

[46] S. Krishnamurthy, R. Haghpanah, A. Rajendran, and S. Farooq, "Simulation and optimization of a dual-adsorbent, two-bed vacuum swing adsorption process for CO_2 capture from wet flue gas," *Ind. Eng. Chem. Res.*, vol. 53, no. 37, pp. 14462–14473, 2014.

[47] D. Siderius, V. Shen, R. Johnson III, and R. van Zee, *NIST/ARPA-E Database of Novel and Emerging Adsorbent Materials, NIST Standard Reference Database Number 205.* National Institute of Standards and Technology: Gaithersburg MD, http://adsorbents.nist.gov, [retrieved [August 17, 2018], 2017.

[48] A. K. Rajagopalan and A. Rajendran, "The effect of Nitrogen adsorption on vacuum swing adsorption based post-combustion CO_2 capture," *Int. J. Greenh. Gas Control*, vol. In Press, 2018.

[49] Y. Tao, H. Kanoh, L. Abrams, and K. Kaneko, "Mesopore-modified zeolites: preparation, characterization, and applications," *Chem. Rev.*, vol. 106, no. 3, pp. 896–910, 2006.

[50] *http://www.iza-structure.org/databases/.* International Zeolite Association (IZA), 2017.

[51] R. Pophale, P. A. Cheeseman, and M. W. Deem, "A database of new zeolite-like materials," *Phys. Chem. Chem. Phys.*, vol. 13, no. 27, pp. 12407–12412, 2011.

[52] R. Banerjee, H. Furukawa, D. Britt, C. Knobler, M. OKeeffe, and O. M. Yaghi, "Control of pore size and functionality in isoreticular zeolitic imidazolate frameworks and their carbon dioxide selective capture properties," *J. Am. Chem. Soc.*, vol. 131, no. 11, pp. 3875–3877, 2009.

[53] A. Phan, C. J. Doonan, F. J. Uribe-Romo, C. B. Knobler, M. Okeeffe, and O. M. Yaghi, "Synthesis, structure, and carbon dioxide capture properties of zeolitic imidazolate frameworks," *Acc. Chem. Res*, vol. 43, no. 1, pp. 58–67, 2010.

[54] T. Watanabe and D. S. Sholl, "Accelerating applications of metal–organic frameworks for gas adsorption and separation by computational screening of materials," *Langmuir*, vol. 28, no. 40, pp. 14114–14128, 2012.

[55] Y. G. Chung, J. Camp, M. Haranczyk, B. J. Sikora, W. Bury, V. Krungleviciute, T. Yildirim, O. K. Farha, D. S. Sholl, and R. Q. Snurr, "Computation-ready, experimental metal–organic frameworks: A tool to enable high-throughput screening of nanoporous crystals," *Chem. Mater.*, vol. 26, no. 21, pp. 6185–6192, 2014.

[56] C. E. Wilmer, M. Leaf, C. Y. Lee, O. K. Farha, B. G. Hauser, J. T. Hupp, and R. Q. Snurr, "Large-scale screening of hypothetical metal–organic frameworks," *Nat. Chem.*, vol. 4, no. 2, p. 83, 2012.

[57] C. Altintas, G. Avci, H. Daglar, A. Nemati Vesali Azar, S. Velioglu, I. Erucar, and S. Keskin, "Database for CO_2 separation performances of MOFs based on computational materials screening," *ACS Appl. Mater. Interfaces*, vol. 10, no. 20, pp. 17257–17268, 2018.

[58] H. Fang, A. Kulkarni, P. Kamakoti, R. Awati, P. I. Ravikovitch, and D. S. Sholl, "Identification of high-CO_2-capacity cationic zeolites by accurate computational screening," *Chem. Mater.*, vol. 28, no. 11, pp. 3887–3896, 2016.

[59] *http://www.iza-structure.org/databases.* International Zeolite Association (IZA), 2011.

[60] M. W. Deem, R. Pophale, P. A. Cheeseman, and D. J. Earl, "Computational discovery of new zeolite-like materials," *J. Phys. Chem. C*, vol. 113, no. 51, pp. 21353–21360, 2009.

[61] A. K. Rajagopalan and A. Rajendran, "The effect of nitrogen adsorption on vacuum swing adsorption based post-combustion CO_2 capture," *Int. J. Greenh. Gas Control*, vol. 78, pp. 437–447, 2018.

[62] K. N. Pai, J. D. Baboolal, D. A. Sharp, and A. Rajendran, "Evaluation of diamine-appended metal-organic frameworks for post-combustion CO_2 capture by vacuum swing adsorption," *Sep. Purif. Technol.*, vol. 211, pp. 540–550, 2019.

[63] R. Haghpanah, A. Rajendran, S. Farooq, I. A. Karimi, and M. Amanullah, "Discrete equilibrium data from dynamic column breakthrough experiments," *Ind. Eng. Chem. Res.*, vol. 51, no. 45, pp. 14834–14844, 2012.

Appendix A

Detailed Model

Table A.1: Model equations for predicting the column dynamics in the detailed model [3].

Model equations

Overall mass balance

$$\frac{1}{P}\frac{\partial P}{\partial t} - \frac{1}{T}\frac{\partial T}{\partial t} = -\frac{T}{P}\frac{\partial}{\partial z}\left(\frac{P}{T}v\right) - \frac{RT}{P}\frac{1-\epsilon_\mathrm{B}}{\epsilon_\mathrm{B}}\sum_{i=1}^{n_\mathrm{comp}}\frac{\partial q_\mathrm{i}}{\partial t} \tag{A.1}$$

Component mass balance

$$\frac{\partial y_\mathrm{i}}{\partial t} + \frac{y_\mathrm{i}}{T}\frac{\partial P}{\partial t} - \frac{y_\mathrm{i}}{P}\frac{\partial T}{\partial t} = \frac{T}{P}D_\mathrm{L}\frac{\partial}{\partial z}\left(\frac{P}{T}\frac{\partial y_\mathrm{i}}{\partial z}\right) - \frac{T}{P}\frac{\partial}{\partial z}\left(\frac{y_\mathrm{i}P}{T}v\right) - \frac{RT}{P}\frac{1-\epsilon_\mathrm{B}}{\epsilon_\mathrm{B}}\frac{\partial q_\mathrm{i}}{\partial t} \tag{A.2}$$

Linear driving force model

$$\frac{\partial q_\mathrm{i}}{\partial t} = \alpha_\mathrm{i}(q_\mathrm{i}^* - q_\mathrm{i}) \tag{A.3}$$

Column energy balance

$$\left[\frac{1-\epsilon_\mathrm{B}}{\epsilon_\mathrm{B}}\left(\rho_\mathrm{s}C_\mathrm{p,s} + C_\mathrm{p,a}\sum_{i=1}^{n_\mathrm{comp}}q_\mathrm{i}\right)\right]\frac{\partial T}{\partial t} = \frac{K_\mathrm{z}}{\epsilon_\mathrm{B}}\frac{\partial^2 T}{\partial z^2} - \frac{C_\mathrm{p,g}}{R}\frac{\partial P}{\partial t} - \frac{C_\mathrm{p,g}}{R}\frac{\partial}{\partial z}(vP) \tag{A.4}$$
$$-\frac{1-\epsilon_\mathrm{B}}{\epsilon_\mathrm{B}}C_\mathrm{p,a}T\sum_{i=1}^{n_\mathrm{comp}}\frac{\partial q_\mathrm{i}}{\partial t} + \frac{1-\epsilon_\mathrm{B}}{\epsilon_\mathrm{B}}\sum_{i=1}^{n_\mathrm{comp}}\left(\Big(-\Delta H\Big)\frac{\partial q_\mathrm{i}}{\partial t}\right) - \frac{2h_\mathrm{in}}{\epsilon_\mathrm{B}r_\mathrm{in}}\big(T - T_\mathrm{w}\big)$$

Column wall energy balance

$$\rho_\mathrm{w}C_\mathrm{p,w}\frac{\partial T_\mathrm{w}}{\partial t} = K_\mathrm{w}\frac{\partial^2 T_\mathrm{w}}{\partial z^2} + \frac{2r_\mathrm{in}h_\mathrm{in}}{r_\mathrm{out}^2 - r_\mathrm{in}^2}\big(T - T_\mathrm{w}\big) - \frac{2r_\mathrm{out}h_\mathrm{out}}{r_\mathrm{out}^2 - r_\mathrm{in}^2}\big(T_\mathrm{w} - T_\mathrm{a}\big) \tag{A.5}$$

Pressure drop (Darcy equation)

$$v = \frac{4}{150\mu}\left(\frac{\epsilon_\mathrm{B}}{1-\epsilon_\mathrm{B}}\right)^2 r_\mathrm{p}^2\left(-\frac{\partial P}{\partial z}\right) \tag{A.6}$$

Table A.2: Boundary conditions for the typical steps in a cyclic adsorption process [3].

Step	$z = 0$	$z = L$
OPEN-CLOSED	$P\|_{\mathrm{z=0}} = P_2 + (P_1 - P_2)e^{(-\alpha_p t)}$	$\left.\frac{\partial y_i}{\partial \mathrm{z}}\right\|_{\mathrm{z=L}} = 0$
	$D_{\mathrm{L}} \left.\frac{\partial y_i}{\partial z}\right\|_{\mathrm{z=0}} = -v\|_{\mathrm{z=0}} \left(y_{i,\mathrm{feed}} - y_i\|_{\mathrm{z=0}}\right)$	$\left.\frac{\partial P}{\partial \mathrm{z}}\right\|_{\mathrm{z=L}} = 0$
	$\left.\frac{\partial \mathrm{T}}{\partial \mathrm{z}}\right\|_{\mathrm{z=0}} = -\epsilon\, v\|_{\mathrm{z=0}}\, \rho_g C_{pg}(T_{\mathrm{feed}} - T\|_{\mathrm{z=0}})$	$\left.\frac{\partial \mathrm{T}}{\partial \mathrm{z}}\right\|_{\mathrm{z=L}} = 0$
	$T_{\mathrm{w}}\|_{\mathrm{z=0}} = T_{\mathrm{a}}$	$T_{\mathrm{w}}\|_{\mathrm{z=L}} = T_{\mathrm{a}}$
OPEN-OPEN	$v\|_{\mathrm{z=0}} = v_{\mathrm{feed}}$	$P\|_{\mathrm{z=L}} = P_2$
	$D_{\mathrm{L}} \left.\frac{\partial y_i}{\partial z}\right\|_{\mathrm{z=0}} = -v\|_{\mathrm{z=0}} \left(y_{i,\mathrm{feed}} - y_i\|_{\mathrm{z=0}}\right)$	$\left.\frac{\partial y_i}{\partial z}\right\|_{\mathrm{z=L}} = 0$
	$\left.\frac{\partial,T}{\partial z}\right\|_{\mathrm{z=0}} = -\epsilon\, v\|_{\mathrm{z=0}}\, \rho_g C_{p,\mathrm{g}}(T_{feed} - T\|_{\mathrm{z=0}})$	$\left.\frac{\partial T}{\partial z}\right\|_{\mathrm{z=L}} = 0$
	$T_w\|_{\mathrm{z=0}} = T_a$	$T_w\|_{\mathrm{z=L}} = T_a$
CLOSED-OPEN	$v\|_{\mathrm{z=0}} = 0$	$P\|_{\mathrm{z=L}} = P_1 + (P_2 - P_1)e^{(-\alpha_p t)}$
	$\left.\frac{\partial y_i}{\partial z}\right\|_{\mathrm{z=0}} = 0$	$\left.\frac{\partial y_i}{\partial z}\right\|_{\mathrm{z=L}} = 0$
	$\left.\frac{\partial T}{\partial z}\right\|_{\mathrm{z=0}} = 0$	$\left.\frac{\partial T}{\partial z}\right\|_{\mathrm{z=L}} = 0$
	$\left.\frac{\partial P}{\partial z}\right\|_{\mathrm{z=0}} = 0$	$T_w\|_{\mathrm{z=L}} = T_a$

Table A.3: Detailed model process parameters [3]

Parameter		Value	
Column Length	L	1	[m]
Inner column radius	r_{in}	0.1445	[m]
Outer column radius	r_{out}	0.1620	[m]
Column void fraction	ε	0.37	[-]
Particle voidage	ε_{p}	0.35	[-]
Particle radius	r_{p}	7.50×10^{-04}	[m]
Tortuosity	τ'	3	[-]
Column wall density	ρ_{s}	7800	[kg/m^3]
Specific heat capacity of gas phase	$C_{\text{p,g}}$	30.7	[J mol^{-1} K^{-1}]
Specific heat capacity of adsorbed phase	$C_{\text{p,a}}$	30.7	[J mol^{-1} K^{-1}]
Specific heat capacity of adsorbent phase	$C_{\text{p,s}}$	1070	[J kg^{-1} K^{-1}]
Specific heat capacity of column wall	$C_{\text{p,w}}$	502	[J kg^{-1} K^{-1}]
Fluid viscosity	μ	1.72×10^{-05}	[kg m^{-1} s^{-1}]
Molecular diffusivity	D_{m}	1.30×10^{-05}	[m^2 s^{-1}]
Adiabatic constant	γ	1.4	[-]
Effective gas thermal conductivity	K_{z}	0.09	[J m^{-1} K^{-1} s^{-1}]
Thermal conductivity of column wall	K_{w}	16	[J m^{-1} K^{-1} s^{-1}]
Inside heat transfer coefficient	h_{in}	8.6	[J m^{-2} K^{-1} s^{-1}]
Outside heat transfer coefficient	h_{out}	2.5	[J m^{-2} K^{-1} s^{-1}]
Universal gas constant	R	8.314	[m^3 Pa mol^{-1} K^{-1}]
Ambient Temperature	T_{a}	298.15	[K]

Appendix B

BAAM Transitions for the 4-step cycle with LPP

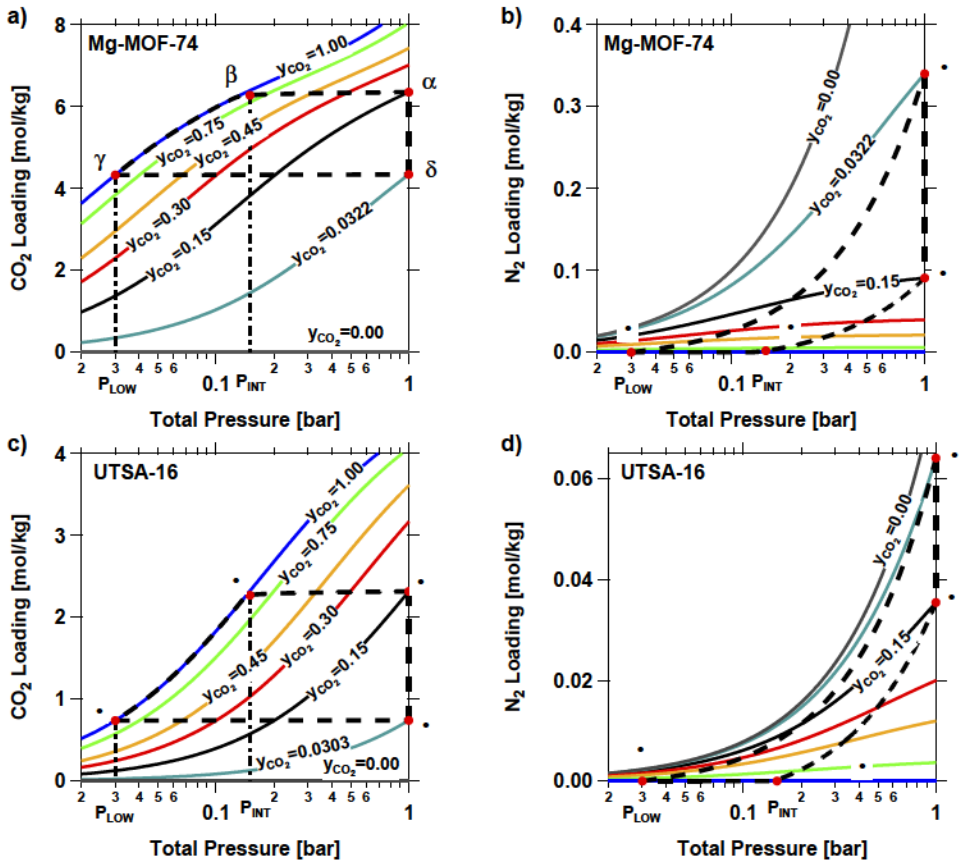

Figure B.1: Batch adsorber analogue model (BAAM) transitions (black dashed lines) of the 4 Step VSA cycle with LPP for Mg-MOF-74 (a) CO_2 isotherm - (b) N_2 isotherm and for UTSA-16 (c) CO_2 isotherm - (d) N_2 isotherm.

Appendix C

Analytical expressions for the performance indicators

As observed from Fig. 2.3, the transitions for the various steps of the 4-step PSA cycle indicate that for materials with high selectivity (an approximate value of $\alpha = \frac{q^*_{\mathrm{CO}_2} y_{\mathrm{N}_2}}{q^*_{\mathrm{N}_2} y_{\mathrm{CO}_2}} \geq 50$) can be suggested), a simple approach can be used to estimate the process performance. The blowdown and evacuation transitions start from state α and move horizontally, i.e., at constant $q^*_{\mathrm{CO}_2}$, until $y_{\mathrm{CO}_2} = 1.00$ is reached and follow $y_{\mathrm{CO}_2} = 1.00$ isotherm until state γ is reached. P_{INT} at which $y^{\beta}_{\mathrm{CO}_2}$ becomes 1.00 can be calculated by solving the non-linear equation given by $q^{*\alpha}_{\mathrm{CO2}} = q^{*\beta}_{\mathrm{CO2}}$. This is shown in Eq. C.1.

$$P_{\mathrm{INT}} = \frac{P_{\mathrm{H}} y^{\mathrm{feed}}_{\mathrm{CO}_2}}{1 + \frac{b_{\mathrm{N}_2}}{\mathrm{R_g}T} P_{\mathrm{H}} (1 - y^{\mathrm{feed}}_{\mathrm{CO}_2})} \tag{C.1}$$

It is important to note here that P_{INT} is a function of b_{N_2} only as this step ensures all N_2 is removed in this step. In the evacuation step, moving from β to γ in the plot, if the gas phase concentration is considered negligible, then the amount of CO_2 coming from this step can be just found by the difference of the CO_2 loading at step β and γ and it is given by the equation below.

$$N^{\beta}_{\mathrm{CO}_2,\mathrm{solid}} - N^{\gamma}_{\mathrm{CO}_2,\mathrm{solid}} = \frac{q_{\mathrm{sb,CO}_2} w \frac{b_{\mathrm{CO}_2}}{\mathrm{R_g}T} \left(P_{\mathrm{H}} y^{\mathrm{feed}}_{\mathrm{CO}_2} - P_{\mathrm{LOW}} - \frac{b_{\mathrm{N}_2}}{\mathrm{R_g}T} P_{\mathrm{H}} P_{\mathrm{LOW}} (1 - y^{\mathrm{feed}}_{\mathrm{CO}_2}) \right)}{\left(1 + \frac{b_{\mathrm{CO}_2}}{\mathrm{R_g}T} P_{\mathrm{LOW}} \right) \left(1 + \frac{b_{\mathrm{CO}_2}}{\mathrm{R_g}T} P_{\mathrm{H}} y^{\mathrm{feed}}_{\mathrm{CO}_2} + \frac{b_{\mathrm{N}_2}}{\mathrm{R_g}T} P_{\mathrm{H}} (1 - y^{\mathrm{feed}}_{\mathrm{CO}_2}) \right)} \tag{C.2}$$

For the LPP step, the value of $y^{\delta}_{\mathrm{CO}_2}$ can be calculated by solving the isotherm expression for $q^{*\gamma}_{\mathrm{CO2}} = q^{*\delta}_{\mathrm{N2}}$.

$$y^{\delta}_{\mathrm{CO}_2} = \frac{P_{\mathrm{LOW}} \left(1 + \frac{b_{\mathrm{N}_2}}{\mathrm{R_g}T} P_{\mathrm{H}} \right)}{P_{\mathrm{H}} \left(1 + \frac{b_{\mathrm{N}_2}}{\mathrm{R_g}T} P_{\mathrm{LOW}} \right)} \tag{C.3}$$

In adsorption step, the same set of equations as that of BAAM was considered. The two no-linear equations were solved for N_{feed} which is given by the expression below.

$$N_{\text{feed}} = \frac{q_{\text{sb,CO}_2} w \frac{b_{\text{CO}_2}}{\text{R}_\text{g}T}(P_\text{H} - P_\text{LOW}) + q_{\text{sb,N}_2} w \frac{b_{\text{N}_2}}{\text{R}_\text{g}T} P_\text{LOW}\left(1 + \frac{b_{\text{CO}_2}}{\text{R}_\text{g}T} P_\text{H}\right)}{\left(1 + \frac{b_{\text{CO}_2}}{\text{R}_\text{g}T} P_\text{LOW}\right)\left(1 + \frac{b_{\text{CO}_2}}{\text{R}_\text{g}T} P_\text{H} y^{\text{feed}}_{\text{CO}_2} + \frac{b_{\text{N}_2}}{\text{R}_\text{g}T} P_\text{H}(1 - y^{\text{feed}}_{\text{CO}_2})\right)} \tag{C.4}$$

where,

With all the four states now identified, the purity, recovery, energy consumption and working capacity can be estimated. This approach is similar to those that have been used in the literature [43].

$$\frac{Pu_{\text{CO}_2}\,[\%]}{100} = 1 \tag{C.5}$$

$$\frac{Re_{\text{CO}_2}\,[\%]}{100} = \frac{q_{\text{sb,CO}_2} w \frac{b_{\text{CO}_2}}{\text{R}_\text{g}T}\left(P_\text{H} y^{\text{feed}}_{\text{CO}_2} - P_\text{LOW} - \frac{b_{\text{N}_2}}{\text{R}_\text{g}T} P_\text{H} P_\text{LOW}(1 - y^{\text{feed}}_{\text{CO}_2})\right)}{\left(q_{\text{sb,CO}_2} w \frac{b_{\text{CO}_2}}{\text{R}_\text{g}T}(P_\text{H} - P_\text{LOW}) + q_{\text{sb,N}_2} w \frac{b_{\text{N}_2}}{\text{R}_\text{g}T} P_\text{LOW}\left(1 + \frac{b_{\text{CO}_2}}{\text{R}_\text{g}T} P_\text{H}\right)\right) y^{\text{feed}}_{\text{CO}_2}} \tag{C.6}$$

$$En\left[\frac{\text{kWh}_\text{e}}{\text{tonne CO}_2\text{ cap.}}\right] = \frac{W_\text{EVAC}}{(N^{\beta}_{\text{CO}_2,\text{total}} - N^{\gamma}_{\text{CO}_2,\text{total}})\text{M}_{\text{CO}_2}} \tag{C.7}$$

$$WC_{\text{CO}_2}\left[\frac{\text{mol CO}_2}{\text{m}^3\text{ of adsorbent}}\right] = \frac{N^{\beta}_{\text{CO}_2,\text{total}} - N^{\gamma}_{\text{CO}_2,\text{total}}}{V(1-\epsilon)} \tag{C.8}$$

Appendix D

Screening of the adsorbents considered by Khurana and Farooq [1]

Table D.1: Dual-site Langmuir isotherm parameters of the adsorbents considered by Khurana and Farooq [1].

Adsorbent	Partilce density	q_{sb,CO_2}	b_{0,CO_2}	$\Delta U_{b,CO_2}$	q_{sd,CO_2}	d_{0,CO_2}	$\Delta U_{d,CO_2}$	q_{sb,N_2}	b_{0,N_2}	$\Delta U_{b,N_2}$	q_{sd,N_2}	d_{0,N_2}	$\Delta U_{d,N_2}$
	[kg/m^3]	[mol/kg]	[m^3/mol]	[kJ/mol]	[mol/kg]	[m^3/mol]	[kJ/mol]	[mol/kg]	[m^3/mol]	[kJ/mol]	[mol/kg]	[m^3/mol]	[kJ/mol]
MOF-177	1130	3.02	2.14×10^{-05}	10.10	3.45	1.36×10^{-05}	10.54	2.44	5.90×10^{-05}	5.26	2.47	3.67×10^{-05}	5.49
MgMOF-74	1130	3.49	1.50×10^{-07}	39.62	4.17	5.28×10^{-07}	25.26	4.31	1.11×10^{-06}	19.90	0.13	1.65×10^{-03}	4.52
UTSA-16	1130	4.4	4.11×10^{-12}	45.54	7.34	6.33×10^{-07}	30.54	9.32	2.87×10^{-06}	9.84	9.32	2.87×10^{-06}	9.84
Activated Carbon	1130	2.3	1.34×10^{-05}	16.62	0.2	2.56×10^{-06}	28.56	0.59	7.24×10^{-13}	20.73	1.67	1.24×10^{-07}	54.44
Na-X	1130	2.4	8.44×10^{-07}	38.70	2.95	1.77×10^{-07}	32.36	0.25	1.39×10^{-05}	16.65	5.1	2.69×10^{-05}	7.51
Mg-X	1130	3.3	2.01×10^{-05}	34.59	3.25	1.56×10^{-07}	33.43	0.29	4.13×10^{-05}	13.67	6.25	1.59×10^{-05}	8.16
Al-X	1130	3.23	6.69×10^{-07}	42.34	3.44	1.22×10^{-08}	40.34	0.39	5.20×10^{-05}	12.47	6.28	1.38×10^{-05}	8.24

Table D.1 continued from previous page

Adsorbent	Particle density [kg/m^3]	q_{sb,CO_2} [mol/kg]	b_{0,CO_2} [m^3/mol]	$\Delta U_{b,CO_2}$ [J/mol]	q_{sd,CO_2} [mol/kg]	d_{0,CO_2} [m^3/mol]	$\Delta U_{d,CO_2}$ [J/mol]	q_{sb,N_2} [mol/kg]	b_{0,N_2} [m^3/mol]	$\Delta U_{b,N_2}$ [J/mol]	q_{sd,N_2} [mol/kg]	d_{0,N_2} [m^3/mol]	$\Delta U_{d,N_2}$ [J/mol]
NAB	1605.25	4.04	5.59×10^{-08}	29.28	1.98	3.17×10^{-05}	11.31	7.37	9.97×10^{-08}	15.49	3.91	2.24×10^{-05}	4.27
h8291835	1881	1.5	5.43×10^{-08}	30.56	1.83	1.32×10^{-05}	14.58	0.71	1.84×10^{-05}	8.22	2.66	3.25×10^{-05}	4.95
h8277919	2370	0.23	1.15×10^{-06}	32.90	1.42	3.76×10^{-08}	55.48	1.06	2.71×10^{-06}	18.13	1.69	4.51×10^{-07}	17.38
h8272272	2060	0.18	1.97×10^{-10}	39.51	2.48	1.85×10^{-06}	36.37	2.82	1.90×10^{-06}	14.72	0.75	2.54×10^{-07}	5.28
h8155527	2044	0.83	3.69×10^{-07}	30.30	1.36	1.13×10^{-07}	31.31	0.83	1.90×10^{-06}	9.28	4.46	5.31×10^{-06}	7.79
h8124767	1771.68	3.09	1.27×10^{-07}	35.45	0.36	1.42×10^{-04}	3.61	1.51	1.13×10^{-08}	16.64	3.7	4.38×10^{-06}	11.21
CaA	1514	3.94	6.61×10^{-10}	56.14	1.6	4.74×10^{-04}	12.01	2.77	4.34×10^{-05}	10.50	2.77	4.34×10^{-05}	10.50
CaX	1426	3.19	1.84×10^{-07}	38.50	3.55	5.11×10^{-07}	28.13	3.37	5.56×10^{-04}	2.54	3.37	5.56×10^{-04}	2.54
MgA	1514	3.58	3.21×10^{-07}	34.20	1.57	1.05×10^{-06}	23.98	2.58	2.10×10^{-07}	22.21	2.58	2.10×10^{-07}	22.21
MgX	1426	3.38	7.44×10^{-08}	38.33	3.3	1.92×10^{-07}	30.06	3.35	1.06×10^{-07}	22.41	3.35	1.06×10^{-07}	22.41
NaA	1514	2.4	4.98×10^{-06}	27.60	1.57	4.84×10^{-07}	27.57	1.99	5.58×10^{-05}	5.82	1.99	5.58×10^{-05}	5.82
NaX	1426	2.5	2.23×10^{-08}	47.59	3.81	1.13×10^{-07}	34.88	3.16	9.57×10^{-06}	12.59	3.16	9.57×10^{-06}	12.59
PS-MFI	1838	1.72	2.08×10^{-06}	23.71	1.72	2.08×10^{-06}	23.71	1.72	5.12×10^{-07}	19.74	1.72	5.12×10^{-07}	19.74
Mg-MOF-74	914.88	6.32	1.01×10^{-06}	34.84	9.08	8.03×10^{-06}	17.29	2.5	8.89×10^{-06}	16.21	2.5	8.89×10^{-06}	16.21
Zn-MOF-74	1219.39	5.11	4.66×10^{-06}	22.50	5.11	4.66×10^{-06}	22.50	5.09	9.72×10^{-06}	10.93	5.09	9.72×10^{-06}	10.93
Co-MOF-74	1180.54	4.33	1.19×10^{-07}	34.02	4.33	1.19×10^{-07}	34.02	4.33	3.82×10^{-05}	9.88	4.33	3.82×10^{-05}	9.88
Ni-MOF-74	1194.09	2.41	1.65×10^{-08}	43.35	6.59	2.23×10^{-05}	18.17	3.33	5.55×10^{-07}	22.80	3.33	5.55×10^{-07}	22.80
MOF-177	426.74	12.5	9.74×10^{-06}	11.19	12.5	9.74×10^{-06}	11.19	2.5	3.32×10^{-05}	8.37	2.5	3.32×10^{-05}	8.37
CuBTC	948.8	8.79	4.30×10^{-07}	24.97	8.79	4.30×10^{-07}	24.97	2.81	7.20×10^{-06}	12.83	2.81	7.20×10^{-06}	12.83
CuBTTri	789	21.3	4.11×10^{-07}	21.74	21.3	4.11×10^{-07}	21.74	2.5	1.51×10^{-03}	-0.60	2.5	1.51×10^{-03}	-0.60
mmen-CuBTTri	1059	2.34	2.97×10^{-10}	50.48	2.34	2.97×10^{-10}	50.48	0.15	1.66×10^{-06}	22.03	0.15	1.66×10^{-06}	22.03
UMCM-1	429	75	5.90×10^{-06}	8.40	75	5.90×10^{-06}	8.40	27.5	2.50×10^{-05}	2.93	27.5	2.50×10^{-05}	2.93

Table D.1 continued from previous page

Adsorbent	Particle density [kg/m^3]	q_{sb,CO_2} [mol/kg]	b_{0,CO_2} [m^3/mol]	$\Delta U_{b,CO_2}$ [J/mol]	q_{sd,CO_2} [mol/kg]	d_{0,CO_2} [m^3/mol]	$\Delta U_{d,CO_2}$ [J/mol]	q_{sb,N_2} [mol/kg]	b_{0,N_2} [m^3/mol]	$\Delta U_{b,N_2}$ [J/mol]	q_{sd,N_2} [mol/kg]	d_{0,N_2} [m^3/mol]	$\Delta U_{d,N_2}$ [J/mol]
SIFSIX-3-Cu	1728	2.4	5.75×10^{-07}	45.00	0.4	8.04×10^{-03}	1.24	1.4	6.46×10^{-05}	8.29	1.4	6.46×10^{-05}	8.29
SIFSIX-3-Zn	1574	2.6	6.40×10^{-07}	38.98	0.29	4.95×10^{-07}	25.35	1.44	5.42×10^{-05}	9.69	1.44	5.42×10^{-05}	9.69
ZIF-8	949	7.1	8.87×10^{-07}	18.44	7.1	8.87×10^{-07}	18.44	61.1	6.92×10^{-06}	10.68	61.1	6.92×10^{-06}	10.68
ZIF-68	900.77	2.92	1.81×10^{-06}	21.47	2.92	1.81×10^{-06}	21.47	2.15	4.10×10^{-06}	12.92	2.15	4.10×10^{-06}	12.92
ZIF-69	998.74	3.12	3.94×10^{-06}	19.69	3.12	3.94×10^{-06}	19.69	2.97	8.36×10^{-06}	10.68	2.97	8.36×10^{-06}	10.68
ZIF-70	747.24	4.24	4.38×10^{-06}	17.36	4.24	4.38×10^{-06}	17.36	0.86	1.78×10^{-05}	11.76	0.86	1.78×10^{-05}	11.76
ZIF-78	1023.9	1.78	3.04×10^{-06}	24.11	1.78	3.04×10^{-06}	24.11	1.68	1.87×10^{-05}	10.78	1.68	1.87×10^{-05}	10.78
ZIF-79	937.03	1.78	1.49×10^{-06}	23.46	1.78	1.49×10^{-06}	23.46	0.94	1.18×10^{-05}	12.33	0.94	1.18×10^{-05}	12.33
ZIF-81	1124.27	1.94	1.88×10^{-06}	23.00	1.94	1.88×10^{-06}	23.00	1.09	1.32×10^{-05}	11.71	1.09	1.32×10^{-05}	11.71
ZIF-82	815.86	2.47	2.87×10^{-06}	22.40	2.47	2.87×10^{-06}	22.40	1.71	1.28×10^{-05}	11.27	1.71	1.28×10^{-05}	11.27
PPN-4	284.1	60	2.30×10^{-06}	11.34	60	2.30×10^{-06}	11.34	4.1	1.83×10^{-04}	4.09	4.1	1.83×10^{-04}	4.09
PPN-6	325	6	1.30×10^{-05}	13.83	6	1.30×10^{-05}	13.83	0.25	2.18×10^{-03}	4.79	0.25	2.18×10^{-03}	4.79
PPN-6-CH2Cl	528	5.2	4.05×10^{-06}	17.53	5.2	4.05×10^{-06}	17.53	0.32	6.40×10^{-04}	6.04	0.32	6.40×10^{-04}	6.04
PPN-6-SO3H	642	3	1.39×10^{-06}	25.30	3	1.39×10^{-06}	25.30	0.2	1.00×10^{-03}	6.75	0.2	1.00×10^{-03}	6.75
PPN-6-SO3Li	666	2.5	9.52×10^{-07}	27.75	2.5	9.52×10^{-07}	27.75	0.2	2.63×10^{-03}	4.61	0.2	2.63×10^{-03}	4.61
PPN-6-CH2DETA	805	2.68	1.12×10^{-06}	42.81	2.68	1.12×10^{-06}	42.81	0.05	4.15×10^{-05}	15.47	0.05	4.15×10^{-05}	15.47
PPN-6-CH2TAEA	982.5	2.41	4.29×10^{-05}	32.49	2.41	4.29×10^{-05}	32.49	0.01	8.64×10^{-04}	12.39	0.01	8.64×10^{-04}	12.39
PPN-6-CH2TETA	883.8	2.38	4.53×10^{-08}	45.71	2.38	4.53×10^{-08}	45.71	0.02	8.41×10^{-05}	15.77	0.02	8.41×10^{-05}	15.77
ZIF-36-CAG	2006.5	0.74	6.93×10^{-08}	49.25	0.74	6.93×10^{-08}	49.25	0.74	1.26×10^{-06}	22.86	0.74	1.26×10^{-06}	22.86
ZIF-36-FRL	1808.87	2.01	5.00×10^{-08}	38.14	1.01	9.10×10^{-07}	21.87	1.51	6.29×10^{-07}	16.23	1.51	6.29×10^{-07}	16.23
ZIF-39-DIA	1009.17	5.17	9.93×10^{-08}	26.36	5.17	9.93×10^{-08}	26.36	5.17	5.45×10^{-07}	13.82	5.17	5.45×10^{-07}	13.82
ZIF-39-ZNI	1497.35	0.64	6.43×10^{-08}	27.95	0.64	6.43×10^{-08}	27.95	0.64	7.22×10^{-07}	19.84	0.64	7.22×10^{-07}	19.84

Table D.1 continued from previous page

Adsorbent	Particle density [kg/m^3]	q_{sb,CO_2} [mol/kg]	b_{0,CO_2} [m^3/mol]	$\Delta U_{b,CO_2}$ [J/mol]	q_{sd,CO_2} [mol/kg]	d_{0,CO_2} [m^3/mol]	$\Delta U_{d,CO_2}$ [J/mol]	q_{sb,N_2} [mol/kg]	b_{0,N_2} [m^3/mol]	$\Delta U_{b,N_2}$ [J/mol]	q_{sd,N_2} [mol/kg]	d_{0,N_2} [m^3/mol]	$\Delta U_{d,N_2}$ [J/mol]
ZIF-40-GIS	1254.51	2.21	1.32×10^{-06}	30.74	3.76	2.29×10^{-03}	1.14	2.98	1.80×10^{-06}	19.62	2.98	1.80×10^{-06}	19.62
ZIF-116-CAG	1353.83	2.14	6.22×10^{-07}	35.29	2.51	1.46×10^{-06}	18.27	2.32	1.43×10^{-06}	21.83	2.32	1.43×10^{-06}	21.83
ZIF-116-MER	850.95	8.28	1.78×10^{-06}	19.52	8.28	1.78×10^{-06}	19.52	8.28	1.02×10^{-05}	8.99	8.28	1.02×10^{-05}	8.99
ZIF-116-SOD	855.31	7.08	4.67×10^{-06}	15.43	7.08	4.67×10^{-06}	15.43	7.08	1.11×10^{-05}	8.75	7.08	1.11×10^{-05}	8.75
HMOF-MOF-5	572.98	13.68	5.57×10^{-06}	12.44	13.68	5.57×10^{-06}	12.44	13.68	2.05×10^{-05}	5.49	13.68	2.05×10^{-05}	5.49
HMOF-16	701.06	15.24	9.29×10^{-07}	20.16	15.24	9.29×10^{-07}	20.16	0.77	2.58×10^{-04}	5.85	0.77	2.58×10^{-04}	5.85
HMOF-27	777.34	26.46	4.05×10^{-06}	10.01	26.46	4.05×10^{-06}	10.01	0.74	2.78×10^{-04}	5.90	0.74	2.78×10^{-04}	5.90
HMOF-96	576.92	69.3	1.12×10^{-06}	11.97	69.3	1.12×10^{-06}	11.97	0.86	2.99×10^{-03}	6.07	0.86	2.99×10^{-03}	6.07
HMOF-163	1000.38	7.53	3.64×10^{-06}	15.11	7.53	3.64×10^{-06}	15.11	0.51	1.26×10^{-04}	9.16	0.51	1.26×10^{-04}	9.16
HMOF-469	873.26	17.16	2.68×10^{-06}	13.04	17.16	2.68×10^{-06}	13.04	7.4	2.09×10^{-05}	5.85	7.4	2.09×10^{-05}	5.85
HMOF-541	905.88	10.25	2.39×10^{-06}	15.47	10.25	2.39×10^{-06}	15.47	0.48	1.64×10^{-04}	8.39	0.48	1.64×10^{-04}	8.39
HMOF-602	905.88	9.88	2.49×10^{-06}	15.47	9.88	2.49×10^{-06}	15.47	0.52	1.53×10^{-04}	8.39	0.52	1.53×10^{-04}	8.39
HMOF-611	648.95	25.54	1.42×10^{-06}	14.59	25.54	1.42×10^{-06}	14.59	0.84	2.03×10^{-04}	6.84	0.84	2.03×10^{-04}	6.84
HMOF-646	245.77	40.79	4.51×10^{-06}	10.07	40.79	4.51×10^{-06}	10.07	40.79	2.51×10^{-05}	2.97	40.79	2.51×10^{-05}	2.97
HMOF-785	639.42	21.75	3.26×10^{-06}	12.72	21.75	3.26×10^{-06}	12.72	0.83	2.33×10^{-04}	6.95	0.83	2.33×10^{-04}	6.95
HMOF-972	670.41	29.46	2.11×10^{-06}	12.23	29.46	2.11×10^{-06}	12.23	0.79	2.07×10^{-04}	6.77	0.79	2.07×10^{-04}	6.77
HMOF-992	624.98	12.2	1.10×10^{-06}	18.79	12.2	1.10×10^{-06}	18.79	12.2	1.58×10^{-05}	5.83	12.2	1.58×10^{-05}	5.83
HMOF-1041	409.13	20.9	5.32×10^{-06}	12.13	20.9	5.32×10^{-06}	12.13	20.9	2.08×10^{-05}	4.93	20.9	2.08×10^{-05}	4.93
HMOF-1055	711.3	13.79	5.22×10^{-06}	13.51	13.79	5.22×10^{-06}	13.51	0.79	1.96×10^{-04}	7.99	0.79	1.96×10^{-04}	7.99
HMOF-1631	834.9	13.81	2.93×10^{-06}	14.63	13.81	2.93×10^{-06}	14.63	0.56	1.89×10^{-04}	8.39	0.56	1.89×10^{-04}	8.39
HMOF-1708	765.19	16.29	3.47×10^{-06}	12.87	16.29	3.47×10^{-06}	12.87	0.69	1.98×10^{-04}	7.48	0.69	1.98×10^{-04}	7.48
HMOF-1927	849.84	16.43	3.65×10^{-06}	12.25	16.43	3.65×10^{-06}	12.25	0.54	2.35×10^{-04}	7.05	0.54	2.35×10^{-04}	7.05

Table D.1 continued from previous page

Adsorbent	Particle density [kg/m^3]	q_{sb,CO_2} [mol/kg]	b_{0,CO_2} [m^3/mol]	$\Delta U_{b,CO_2}$ [J/mol]	q_{sd,CO_2} [mol/kg]	d_{0,CO_2} [m^3/mol]	$\Delta U_{d,CO_2}$ [J/mol]	q_{sb,N_2} [mol/kg]	b_{0,N_2} [m^3/mol]	$\Delta U_{b,N_2}$ [J/mol]	q_{sd,N_2} [mol/kg]	d_{0,N_2} [m^3/mol]	$\Delta U_{d,N_2}$ [J/mol]
HMOF-1996	612.16	30.8	2.61×10^{-06}	12.15	30.8	2.61×10^{-06}	12.15	0.86	2.60×10^{-04}	6.42	0.86	2.60×10^{-04}	6.42
HMOF-2368	226.63	50	4.18×10^{-06}	9.65	50	4.18×10^{-06}	9.65	50	2.35×10^{-05}	2.75	50	2.35×10^{-05}	0.03

Table D.2: Summary of purity - recovery classification and calculation of minimum energy from the BAAM and then comparison with the data from Khurana and Farooq. $*$ represents adsorbent considered in this work. Adsorbent marked with $\times$ was re-optimized

Adsorbent	$Pu_{CO_2} - Re_{CO_2}$ constraints by Khurana and Farooq [1]	r_{max} [-]	$En_{min,BAAM}$ [kWh_e/tonne CO_2 cap.]	$En_{min,detailed}$ [1] [kWh_e/tonne CO_2 cap.]	$En_{min,scaled}$ [kWh_e/tonne CO_2 cap.]	WC_{CO_2} [mol CO_2/m^3]
MOF-177	0	89.89	-	-	-	-
MgMOF-74	1	125.29	82.27	-	160.70	624.95
UTSA-16	1	128.42	68.87	129.53	145.35	1243.68
Activated Carbon	0	115.60	85.90	-	164.84	123.45
Na-X	1	124.60	75.67	164.83	153.14	577.23
Mg-X	1	126.41	72.18	164.47	149.15	604.90
Al-X	1	127.19	71.01	156.53	147.81	649.62
NAB	1	122.64	76.61	124.24	154.21	223.39
h8291835	1	119.50	81.20	138.36	159.47	211.52
h8277919	1	115.79	101.87	162.01	183.12	182.99
h8272272	1	123.20	90.92	159.86	170.59	395.87
h8155527	1	127.50	69.93	120.6	146.57	434.61
h8124767	1	128.03	70.39	133.25	147.10	912.24
CaA	0	120.61	91.43	-	171.18	858.19
CaX	1	125.71	77.72	192.6	155.48	1159.78
MgA	1	125.27	78.25	189.82	156.09	1261.96
MgX	1	127.13	73.15	158.32	150.26	1172.35
NaA	1	127.86	71.20	133.17	148.03	754.13
NaX	1	126.89	73.86	176.16	151.06	1044.16
PS-MFI	1	117.95	85.11	183.4	163.94	695.44

Table D.2 continued from previous page

Adsorbent	$Pu_{CO_2} - Re_{CO_2}$ constraints by Khurana and Farooq [1]	r_{max} [-]	$En_{min,BAAM}$ [kWh_e/tonne CO_2 cap.]	$En_{min,detailed}$ [1] [kWh_e/tonne CO_2 cap.]	$En_{min,scaled}$ [kWh_e/tonne CO_2 cap.]	WC_{CO_2} [mol CO_2/m^3]
Mg-MOF-74	0	120.28	94.23	-	174.38	1399.02
Zn-MOF-74	1	124.80	75.09	168.71	152.47	1308.24
Co-MOF-74	0	124.15	78.48	-	156.36	1837.44
Ni-MOF-74	0	116.92	95.38	-	175.69	1744.61
MOF-177	0	92.17	-	-	-	-
CuBTC	1	120.18	81.22	177.45	159.49	650.52
CuBTTri	0	117.29	84.30	-	163.02	395.07
mmen-CuBTTri	1	123.12	84.61	-	163.37	776.51
UMCM-1	0	97.84	-	-	-	-
SIFSIX-3-Cu$^{\times}$	0	99.69	-	207.41	-	-
SIFSIX-3-Zn	1	118.73	101.29	200.07	182.47	489.05
ZIF-8	0	38.29	-	-	-	-
ZIF-68	1	116.48	85.46	153.6	164.34	233.38
ZIF-69	1	116.85	84.76	156.74	163.54	295.06
ZIF-70	1	108.43	-	-	-	-
ZIF-78	1	122.36	79.73	152.3	157.79	485.19
ZIF-79	1	117.28	85.81	158.07	164.75	246.92
ZIF-81	1	118.98	83.43	154.49	162.02	325.65
ZIF-82	1	120.54	81.27	149.06	159.55	347.57
PPN-4	0	89.70	-	-	-	-
PPN-6	0	91.06	-	-	-	-
PPN-6-CH2Cl	0	104.71	-	-	-	-

Table D.2 continued from previous page

Adsorbent	$Pu_{CO_2} - Re_{CO_2}$ constraints by Khurana and Farooq [1]	r_{max} [-]	$En_{min,BAAM}$ [kWh_e/tonne CO_2 cap.]	$En_{min,detailed}$ [1] [kWh_e/tonne CO_2 cap.]	$En_{min,scaled}$ [kWh_e/tonne CO_2 cap.]	WC_{CO_2} [mol CO_2/m^3]
PPN-6-SO3H	0	116.27	98.07	-	178.78	327.50
PPN-6-SO3Li	0	117.28	97.65	-	178.30	420.05
PPN-6-CH2DETA	0	115.72	111.31	-	193.94	56.75
PPN-6-CH2TAEA	0	83.10	-	-	-	-
PPN-6-CH2TETA	0	110.25	118.31	-	201.94	266.90
ZIF-36-CAG	1	114.77	117.33	207.07	200.82	45.80
ZIF-36-FRL	1	127.88	71.01	133.95	147.81	653.56
ZIF-39-DIA	1	119.85	80.16	157.02	158.28	189.77
ZIF-39-ZNI	0	91.06	-	-	-	-
ZIF-40-GIS	0	109.14	-	-	-	-
ZIF-116-CAG	0	102.11	-	-	-	-
ZIF-116-MER	1	111.71	99.28	189.53	180.17	253.59
ZIF-116-SOD	0	99.48	-	-	-	-
HMOF-MOF-5	0	93.60	-	-	-	-
HMOF-16	1	117.88	85.31	-	164.17	279.59
HMOF-27	0	89.71	-	-	-	-
HMOF-96	0	98.95	-	-	-	-
HMOF-163	0	94.19	-	-	-	-
HMOF-469	0	97.61	-	-	-	-
HMOF-541	0	96.97	-	-	-	-
HMOF-602	0	97.12	-	-	-	-
HMOF-611	0	94.85	-	-	-	-

Table D.2 continued from previous page

Adsorbent	$Pu_{CO_2} - Re_{CO_2}$ constraints by Khurana and Farooq [1]	r_{max} [-]	$En_{min,BAAM}$ [kWh_e/tonne CO_2 cap.]	$En_{min,detailed}$ [1] [kWh_e/tonne CO_2 cap.]	$En_{min,scaled}$ [kWh_e/tonne CO_2 cap.]	WC_{CO_2} [mol CO_2/m^3]
HMOF-646	0	90.54	-	-	-	-
HMOF-785	0	88.00	-	-	-	-
HMOF-972	0	88.53	-	-	-	-
HMOF-992	1	111.28	101.87	164.79	183.13	127.04
HMOF-1041	0	94.28	-	-	-	-
HMOF-1055	0	91.83	-	-	-	-
HMOF-1631	0	94.19	-	-	-	-
HMOF-1708	0	87.92	-	-	-	-
HMOF-1927	0	87.90	-	-	-	-
HMOF-1996	0	88.24	-	-	-	-
HMOF-2368	0	91.03	-	-	-	-
Mg-MOF-74*	1	127.27	74.49	-	151.79	717.33
Zeolite 13X*	1	128.05	70.24	-	146.93	458.81
UTSA-16*	1	128.58	68.45	-	144.88	804.69
CS-AC*	0	109.88	-	-	-	-

Appendix E

Screening of the NIST/ARPA-E Database

Table E.1: Single-site Langmuir isotherm parameters and performance indicators obtained from the BAAM of the adsorbents considered from the NIST/ARPA-E database. $*$ represents adsorbent with multiple N_2 isotherms at 298 K.

DOI	Adsorbent	q_{sb,CO_2} [mol/kg]	$b_{CO_2,298}$ [m^3/mol]	q_{sb,N_2} [mol/kg]	$b_{N_2,298}$ [m^3/mol]	r_{max} [-]	$En_{min,BAAM}$ [kWh_e/tonne CO_2 cap.]	$En_{min,scaled}$ [kWh_e/tonne CO_2 cap.]	WC_{CO_2} [mol CO_2/m^3]
10.1002/anie.201105966	Cu-TDPAT	9.78	0.0321	9.78	0.0010	122.25	78.93	156.87	1077.71
10.1002/chem.201303086	SNU-151'*	11.02	0.0101	11.02	0.0004	120.35	80.13	158.24	502.19
10.1002/cssc.201000080	Bio-MOF-11*	6.37	0.0415	6.37	0.0012	122.31	79.37	157.37	832.21
10.1002/cssc.201000080	Bio-MOF-11*	5.94	0.0500	5.94	0.0013	122.91	78.74	156.66	877.12
10.1002/macp.201200195	C24H21N3*	4.31	0.1387	4.31	0.0012	126.61	73.54	150.70	822.30
10.1002/macp.201200195	C24H21N3*	3.70	0.1390	3.70	0.0014	126.12	74.69	152.02	721.06
10.1002/macp.201200195	C24H21N3*	3.26	0.3167	3.26	0.0016	127.06	74.07	151.31	647.43
10.1002/macp.201200195	C24H21N3*	5.36	0.0182	5.36	0.0010	117.07	85.30	164.16	435.61

Table E.1 continued from previous page

DOI	Adsorbent	q_{sb,CO_2} [mol/kg]	$b_{CO_2,298}$ [m^3/mol]	q_{sb,N_2} [mol/kg]	$b_{N_2,298}$ [m^3/mol]	r_{max} [-]	$En_{min,BAAM}$ [kWh_e/tonne CO_2 cap.]	$En_{min,scaled}$ [kWh_e/tonne CO_2 cap.]	WC_{CO_2} [mol CO_2/m^3]
10.1002/macp.201200195	C24H21N3*	2.85	0.0422	2.85	0.0018	118.48	85.32	164.19	443.98
10.1002/macp.201200195	C24H21N3*	2.58	0.0488	2.58	0.0020	118.74	85.44	164.32	453.79
10.1002/macp.201200195	C24H21N3*	0.58	0.5275	0.58	0.0092	117.76	98.92	179.75	184.05
10.1002/macp.201200195	C24H21N3*	1.18	0.1438	1.18	0.0045	118.96	89.77	169.28	340.65
10.1002/macp.201200195	C24H21N3*	2.09	0.0551	2.09	0.0025	117.48	87.80	167.02	393.79
10.1016/j.cattod.2011.08.019	Co-MOF-74(M)	8.19	0.0953	8.19	0.0025	122.38	81.63	159.96	1736.80
10.1016/j.ces.2015.03.016	Bio-MOF-11	6.48	0.0549	6.48	0.0015	122.85	79.06	157.02	1012.20
10.1016/j.ces.2015.03.016	Bio-MOF-11	6.48	0.0549	6.48	0.0015	122.85	79.06	157.02	1012.20
10.1016/j.ces.2015.03.016	Bio-MOF-12	7.34	0.0235	7.34	0.0009	120.56	80.91	159.14	684.30
10.1016/j.ces.2015.03.016	bio-MOF-13 (Configuration I)	3.58	0.0500	3.58	0.0010	123.91	76.93	154.58	502.88
10.1016/j.ces.2015.03.016	bio-MOF-13 (Configuration II)	2.48	0.0571	2.48	0.0022	119.24	85.19	164.04	462.38
10.1016/j.fuel.2012.06.016	Amino-MIL-53(Al)	2.65	0.0495	2.65	0.0027	115.99	90.14	169.70	455.46
10.1016/j.fuel.2012.06.016	Amino-MIL-53(Al)	2.69	0.0474	2.69	0.0026	115.73	90.45	170.06	447.04
10.1016/j.ijggc.2013.01.009	Mg-MOF-74	8.13	0.8525	8.13	0.0031	126.51	77.63	155.39	1247.74
10.1016/j.ijggc.2013.01.009	Zeolite 13X	4.45	0.2309	4.45	0.0009	127.96	70.88	147.66	808.97
10.1016/j.ijggc.2013.08.013	Carbon Composite C1-30	4.97	0.0446	4.97	0.0029	114.18	94.78	175.02	736.07
10.1016/j.ijhydene.2013.02.074	CAU-1	5.94	0.0095	5.94	0.0005	116.69	84.85	163.65	274.64
10.1016/j.jcis.2014.05.021	Cu-MOF*	1.06	0.0884	1.06	0.0034	117.79	89.34	168.79	260.41
10.1016/j.jcis.2014.05.021	Cu-MOF*	1.07	0.0872	1.07	0.0034	117.75	89.30	168.74	270.28
10.1016/j.micromeso.2013.06.023	Mg-MOF-74 (3)	8.13	0.7023	8.13	0.0037	125.82	79.39	157.40	1437.35
10.1016/j.micromeso.2013.06.023	Mg-MOF-74 (4)	9.41	0.7076	9.41	0.0037	125.80	79.51	157.53	1604.31
10.1016/j.micromeso.2013.06.023	Ni-MOF-74 (1)	4.18	0.1442	4.18	0.0064	116.02	96.15	176.58	1160.85

Table E.1 continued from previous page

DOI	Adsorbent	q_{sb,CO_2} [mol/kg]	$b_{CO_2,298}$ [m^3/mol]	q_{sb,N_2} [mol/kg]	$b_{N_2,298}$ [m^3/mol]	r_{max} [-]	$En_{min,BAAM}$ [kWh_e/tonne CO_2 cap.]	$En_{min,scaled}$ [kWh_e/tonne CO_2 cap.]	WC_{CO_2} [mol CO_2/m^3]
10.1016/j.micromeso.2013.06.023	Ni-MOF-74 (2)	6.00	0.1610	6.00	0.0061	117.47	93.53	173.59	1841.25
10.1021/Cm303072n	Carbon KNC-A-HCI	6.10	0.0440	6.10	0.0016	120.82	81.93	160.30	897.80
10.1021/Cm303072n	Carbon KNC-A-K	4.61	0.1191	4.61	0.0020	124.49	78.01	155.82	944.33
10.1021/Cm303072n	Carbon SBA-C	2.46	0.0369	2.46	0.0027	112.19	102.36	183.69	293.64
10.1021/Cm303072n	Carbon SBA-C-A-HCI	3.48	0.0307	3.48	0.0021	113.32	95.56	175.90	393.49
10.1021/Cm303072n	Carbon SBA-NC	2.97	0.0824	2.97	0.0021	122.32	81.14	159.40	581.56
10.1021/Es9032309	Zeolite 5A	4.82	0.5695	4.82	0.0034	125.81	78.98	156.93	906.71
10.1021/Ja407135k	[Fe(btzx)3](ClO4)2	2.01	0.0224	2.01	0.0007	120.65	80.52	158.70	177.88
10.1021/Ja809459e	ZIF-78	3.29	0.0519	3.29	0.0016	121.50	81.20	159.47	514.87
10.1021/Ja903411w	H3[(Cu4Cl)3(BTTri)8]	15.95	0.0073	15.95	0.0004	117.55	83.32	161.90	588.79
10.1021/Jp101531m	ZIF-68	4.68	0.0128	4.68	0.0007	116.64	85.43	164.31	278.88
10.1021/Jp101531m	ZIF-69	6.53	0.0090	6.53	0.0006	115.07	87.88	167.12	277.87
10.1021/Jp3046356	Cu-TDPAT*	2.85	0.0564	2.85	0.0039	112.36	107.65	189.74	420.00
10.1021/Jp3046356	Cu-TDPAT*	5.04	0.0500	5.04	0.0021	119.09	85.09	163.92	885.54
10.1021/Jp3046356	Cu-TDPAT*	8.77	0.0289	8.77	0.0012	120.06	82.08	160.47	966.29
10.1021/Jp3046356	Cu-TDPAT*	5.22	0.0690	5.22	0.0020	121.78	81.61	159.94	949.87
10.1021/Jp3099768	Zeolite CHA*	9.20	0.0076	9.20	0.0006	113.33	92.61	172.53	316.07
10.1021/Jp3099768	Zeolite DDR*	2.93	0.0212	2.93	0.0014	113.93	93.02	173.00	249.14
10.1021/Jp3099768	Zeolite EDI*	4.87	0.0162	4.87	0.0014	110.42	114.38	197.45	269.77
10.1021/Jp3099768	Zeolite ERI*	5.02	0.0130	5.02	0.0011	111.17	106.66	188.61	241.66
10.1021/Jp3099768	Zeolite GIS*	4.68	0.1395	4.68	0.0012	126.76	73.20	150.31	899.01
10.1021/Jp3099768	Zeolite GIS*	5.20	0.0576	5.20	0.0010	124.70	75.80	153.29	757.15

Table E.1 continued from previous page

DOI	Adsorbent	q_{sb,CO_2} [mol/kg]	$b_{CO_2,298}$ [m^3/mol]	q_{sb,N_2} [mol/kg]	$b_{N_2,298}$ [m^3/mol]	r_{max} [-]	$En_{min,BAAM}$ [kWh_e/tonne CO_2 cap.]	$En_{min,scaled}$ [kWh_e/tonne CO_2 cap.]	WC_{CO_2} [mol CO_2/m^3]
10.1021/Jp3099768	Zeolite GME*	3.46	0.0369	3.46	0.0015	119.70	83.15	161.70	479.28
10.1021/Jp3099768	Zeolite GME*	2.56	0.0300	2.56	0.0020	113.56	94.56	174.76	288.41
10.1021/Jp3099768	Zeolite MER*	4.09	0.0357	4.09	0.0012	121.39	80.51	158.68	519.50
10.1021/Jp3099768	Zeolite MER*	4.11	0.0176	4.11	0.0012	114.38	91.14	170.84	303.89
10.1021/Jp3099768	Zeolite MOR*	3.29	0.0313	3.29	0.0018	115.82	88.77	168.14	409.29
10.1021/Jp3099768	Zeolite MTT*	1.99	0.0411	1.99	0.0019	117.69	86.34	165.36	311.18
10.1021/Jp3099768	Zeolite MWW*	3.68	0.0226	3.68	0.0015	113.84	92.73	172.67	334.37
10.1021/Jp3099768	Zeolite RHO*	9.66	0.0091	9.66	0.0006	115.75	86.50	165.54	422.07
10.1021/Jp9103068	CPL-2	23.28	0.0018	23.28	0.0001	114.99	87.12	166.24	214.88
10.1021/Jp9103068	CPL-2	14.57	0.0031	14.57	0.0002	115.56	86.06	165.03	225.92
10.1021/Jp9103068	CPL-2	14.84	0.0030	14.84	0.0002	115.46	86.27	165.27	223.13
10.1021/Jp9103068	CPL-2	7.21	0.0053	7.21	0.0004	113.28	92.38	172.26	179.11
10.1021/La302537d	Cu-TDPAT*	10.35	0.0285	10.35	0.0010	121.20	80.33	158.48	1102.73
10.1021/La302537d	Cu-TDPAT*	10.99	0.0189	10.99	0.0010	118.17	83.81	162.45	937.48
10.1021/La302537d	Cu-TDPAT*	15.45	0.0129	15.45	0.0007	118.03	83.35	161.94	944.16
10.1021/La302537d	Cu-TDPAT*	7.70	0.0288	7.70	0.0014	118.38	84.46	163.20	927.86
10.1021/La302537d	Cu-TDPAT*	14.59	0.0176	14.59	0.0007	120.39	80.70	158.89	1079.67
10.1021/La302537d	Cu-TDPAT*	7.53	0.0312	7.53	0.0014	118.89	83.96	162.63	913.14
10.1021/La302537d	Cu-TDPAT*	15.24	0.0177	15.24	0.0007	120.83	80.11	158.22	1092.37
10.1021/jp3046356	Cu-TDPAT	8.20	0.0470	8.20	0.0013	122.89	78.65	156.55	1160.14
10.1021/jp8046467	Carbon	53.61	0.0784	53.61	0.0028	120.44	84.54	163.29	11132.30
10.1039/C0cc05199c	SNU-21H	10.18	0.0067	10.18	0.0006	110.67	113.17	196.06	252.26

Table E.1 continued from previous page

DOI	Adsorbent	q_{sb,CO_2} [mol/kg]	$b_{CO_2,298}$ [m^3/mol]	q_{sb,N_2} [mol/kg]	$b_{N_2,298}$ [m^3/mol]	r_{max} [-]	$En_{min,BAAM}$ [kWh_e/tonne CO_2 cap.]	$En_{min,scaled}$ [kWh_e/tonne CO_2 cap.]	WC_{CO_2} [mol CO_2/m^3]
10.1039/C0cc05199c	SNU-21S	11.21	0.0071	11.21	0.0005	114.09	90.14	169.70	371.81
10.1039/C1cc10899a	[Co(HL)]*2H2O	2.40	0.0532	2.40	0.0016	121.51	81.21	159.48	383.48
10.1039/C1sc00354b	Cu-BTTri	23.31	0.0048	23.31	0.0003	117.60	83.03	161.56	571.05
10.1039/C1sc00354b	Cu-BTTri	14.37	0.0082	14.37	0.0004	118.01	82.85	161.36	588.38
10.1039/C2cc35691k	ZIF-95*	2.75	0.0115	2.75	0.0009	111.26	110.29	192.76	114.69
10.1039/C2cc35691k	ZIF-95*	2.29	0.0138	2.29	0.0010	110.94	106.25	188.15	119.77
10.1039/C2cp23839j	UiO-66*	6.15	0.0086	6.15	0.0007	112.08	97.98	178.68	224.42
10.1039/C2cp23839j	UiO-66*	4.41	0.0157	4.41	0.0009	115.59	87.57	166.77	311.48
10.1039/C2cp23839j	UiO-66-Br*	3.99	0.0235	3.99	0.0013	116.26	87.11	166.23	401.23
10.1039/C2cp23839j	UiO-66-Br*	3.35	0.0306	3.35	0.0016	116.95	86.68	165.75	419.57
10.1039/C2cp23839j	UiO-66-NH2*	5.50	0.0199	5.50	0.0009	119.06	82.67	161.16	470.06
10.1039/C2cp23839j	UiO-66-NH2*	4.67	0.0297	4.67	0.0010	120.94	80.75	158.95	521.70
10.1039/C2cp23839j	UiO-66-NO2*	3.74	0.0358	3.74	0.0017	117.80	85.82	164.76	536.42
10.1039/C2cp23839j	UiO-66-NO2*	4.45	0.0220	4.45	0.0014	114.44	91.51	171.28	394.78
10.1039/C2cp44436d	Activated Carbon-700-0.5*	5.69	0.0567	5.69	0.0024	118.94	85.80	164.73	1059.29
10.1039/C2cp44436d	Activated Carbon-750-0.5	7.02	0.0356	7.02	0.0019	117.16	86.89	165.98	982.33
10.1039/C2cp44436d	Activated Carbon-750-0.5	2.69	0.1711	2.69	0.0055	118.91	90.93	170.60	786.62
10.1039/C2cp44436d	Activated Carbon-750-0.5	6.82	0.0379	6.82	0.0020	117.44	86.66	165.72	1004.05
10.1039/C2cp44436d	Activated Carbon-800-0.5	7.66	0.0263	7.66	0.0019	113.80	93.46	173.50	779.84
10.1039/C3cc43299h	CdSDB	1.11	0.0660	1.11	0.0020	119.95	84.33	163.05	216.98
10.1039/C3ce26800d	[Co(atz)(bdc)0.5]	3.86	0.0175	3.86	0.0004	122.88	77.00	154.66	261.05
10.1039/C3dt50896j	Zn3(TCPB)2(H2O)2	1.04	0.0327	1.04	0.0005	122.39	78.33	156.19	122.68

Table E.1 continued from previous page

DOI	Adsorbent	q_{sb,CO_2} [mol/kg]	$b_{CO_2,298}$ [m^3/mol]	q_{sb,N_2} [mol/kg]	$b_{N_2,298}$ [m^3/mol]	r_{max} [-]	$En_{min,BAAM}$ [kWh_e/tonne CO_2 cap.]	$En_{min,scaled}$ [kWh_e/tonne CO_2 cap.]	WC_{CO_2} [mol CO_2/m^3]
10.1039/C3dt50896j	Zn3(TCPB)2(H2O)2	1.03	0.0348	1.03	0.0005	122.68	77.97	155.77	123.98
10.1039/C3ee42394h	Mg2(dobdc)	7.04	0.5365	7.04	0.0044	124.68	82.09	160.49	1544.59
10.1039/C3sc51319j	CPO-27-Co	8.53	0.1136	8.53	0.0024	123.56	79.85	157.92	1791.58
10.1039/C3sc51319j	CPO-27-Co	8.24	0.1186	8.24	0.0024	123.52	80.10	158.21	1752.47
10.1039/C4cc00375f	[Cu3(TDPAH)(H2O)3] 13H2O 8DMA	12.14	0.0179	12.14	0.0006	121.48	79.21	157.19	852.72
10.1039/C4cc00375f	[Cu3(TDPAH)(H2O)3] 13H2O 8DMA	10.67	0.0224	10.67	0.0007	122.07	78.62	156.51	885.50
10.1039/C4ce00279b	ROD-8a*	4.05	0.0200	4.05	0.0011	116.50	86.49	165.52	353.28
10.1039/C4ce00279b	ROD-8a*	3.28	0.0310	3.28	0.0014	118.58	84.27	162.98	409.07
10.1039/C4dt00230j	Cd (II)-MOF [Cd(L)(DMF)]	2.28	0.0566	2.28	0.0037	113.11	98.80	179.62	388.95
10.1039/C4ee01009d	ZIF-8	4.02	0.0170	4.02	0.0009	116.51	85.95	164.91	311.63
10.1039/C4ee01009d	ZIF-8	3.95	0.0147	3.95	0.0009	114.40	90.19	169.76	256.25
10.1039/C4ee01009d	ZIF-8	4.74	0.0147	4.74	0.0008	116.87	85.09	163.93	325.74
10.1039/c2ee23337a	Ca-A*	4.73	2.6689	4.73	0.0039	126.08	80.70	158.90	368.45
10.1039/c2ee23337a	Ca-A*	4.77	1.6195	4.77	0.0039	126.06	80.07	158.18	523.93
10.1039/c2ee23337a	Ca-A*	5.09	0.8858	5.09	0.0036	126.02	79.25	157.24	789.21
10.1039/c3cc46492j	Carbon	2.99	0.1313	2.99	0.0037	120.81	85.87	164.81	756.15
10.1039/c4cc10002f	activated [NC2H8]4Cu5(BTT)3xG*	4.93	0.0676	4.93	0.0010	125.45	74.67	152.00	748.00
10.1039/c4cc10002f	activated [NC2H8]4Cu5(BTT)3xG*	4.29	0.0304	4.29	0.0012	120.26	81.83	160.20	495.67
10.1039/c4cc10002f	activated [NC2H8]4Cu5(BTT)3xG*	3.04	0.3427	3.04	0.0017	127.06	74.24	151.50	610.67
10.1039/c5dt00909j	[Cd3Na6(BTC)4(H2O)12]H2O	2.75	0.2639	2.75	0.0025	125.48	77.92	155.71	619.71
10.1039/c5dt00909j	[Cd3Na6(BTC)4(H2O)12]H2O	2.76	0.2567	2.76	0.0025	125.43	77.99	155.80	604.58
10.1080/08927022.2011.583648	ZIF-79*	5.44	0.0624	5.44	0.0018	122.27	80.47	158.63	948.44

Table E.1 continued from previous page

DOI	Adsorbent	q_{sb,CO_2} [mol/kg]	$b_{CO_2,298}$ [m^3/mol]	q_{sb,N_2} [mol/kg]	$b_{N_2,298}$ [m^3/mol]	r_{max} [-]	$En_{min,BAAM}$ [kWh_e/tonne CO_2 cap.]	$En_{min,scaled}$ [kWh_e/tonne CO_2 cap.]	WC_{CO_2} [mol CO_2/m^3]
10.1080/08927022.2011.583648	ZIF-79*	4.81	0.0353	4.81	0.0020	116.26	88.35	167.65	658.09
10.3390/en81011531	Bio-MOF-11	18.70	0.0092	18.70	0.0004	120.85	79.38	157.38	764.32
10.1002/Cjce.20700	IRMOF-1*	347.65	0.0001	347.65	0.0000	98.76	-	-	-
10.1002/Cjce.20700	IRMOF-1*	175.86	0.0001	175.86	0.0000	98.45	-	-	-
10.1002/chem.201002818	Zn(bdc)(ted)0.5	5322.31	0.0000	5322.31	0.0000	101.67	-	-	-
10.1002/chem.201103687	[Co3(ndc)-(HCOO)3(mu3-OH)(H2O)]n*	12.14	0.0084	12.14	0.0902	14.39	-	-	-
10.1002/chem.201303086	SNU-150'*	4440.73	0.0000	4440.73	0.0000	101.40	-	-	-
10.1002/cplu.201500104	C50H22Cu3O15*	54.10	0.0015	54.10	0.0011	95.14	-	-	-
10.1016/j.ces.2011.09.009	ZIF-8	1089.60	0.0000	1089.60	0.0000	103.40	-	-	-
10.1016/j.fuel.2012.06.016	MIL-53C	2.35	0.0396	2.35	0.0045	103.93	-	-	-
10.1016/j.fuel.2012.06.016	MIL-53C	2.43	0.0371	2.43	0.0044	103.48	-	-	-
10.1016/j.fuel.2012.06.016	MIL-53S	3.99	0.0403	3.99	0.0047	103.81	-	-	-
10.1016/j.fuel.2012.06.016	MIL-53S	4.24	0.0354	4.24	0.0044	102.89	-	-	-
10.1016/j.inoche.2013.10.022	[Cu(L)DMF]*2H2O	5405.13	0.0000	5405.13	0.0000	101.69	-	-	-
10.1016/j.jiec.2014.12.021	UiO-66	9.98	0.0069	9.98	0.0069	15.01	-	-	-
10.1016/j.micromeso.2013.03.024	CPM-5	5.84	0.0137	5.84	0.0022	99.49	-	-	-
10.1016/j.micromeso.2013.03.024	CPM-5	6.57	0.0112	6.57	0.0020	98.99	-	-	-
10.1016/j.micromeso.2013.03.024	CPM-5	7.14	0.0091	7.14	0.0018	97.67	-	-	-
10.1016/j.micromeso.2013.03.024	CPM-5	10.18	0.0068	10.18	0.0012	98.72	-	-	-
10.1016/j.micromeso.2013.09.006	Ag3[Ag5(mu3-3-5-Ph2tz)6](NO3)2n	1.80	0.0057	1.80	0.0006	102.73	-	-	-
10.1016/j.micromeso.2013.09.006	Ag3[Ag5(mu3-3-5-tBu2tz)6](BF4)2n	1.26	0.0094	1.26	0.0007	107.57	-	-	-
10.1016/j.micromeso.2013.09.006	Ag3[Ag5(mu3-3-5-tBu2tz)6](BF4)2n	0.50	0.0194	0.50	0.0017	102.73	-	-	-

Table E.1 continued from previous page

DOI	Adsorbent	q_{sb,CO_2} [mol/kg]	$b_{CO_2,298}$ [m^3/mol]	q_{sb,N_2} [mol/kg]	$b_{N_2,298}$ [m^3/mol]	r_{max} [-]	$En_{min,BAAM}$ [kWh_e/tonne CO_2 cap.]	$En_{min,scaled}$ [kWh_e/tonne CO_2 cap.]	WC_{CO_2} [mol CO_2/m^3]
10.1021/Es9032309	IRMOF-1	1.78	0.0193	1.78	0.0016	109.14	-	-	-
10.1021/Es9032309	MOF-177	39.79	0.0010	39.79	0.0001	108.65	-	-	-
10.1021/Jp3099768	Zeolite BEA*	20.15	0.0017	20.15	0.0002	103.45	-	-	-
10.1021/Jp3099768	Zeolite BEA*	18.92	0.0009	18.92	0.0002	90.50	-	-	-
10.1021/Jp3099768	Zeolite BEA*	4.91	0.0007	4.91	0.0009	98.50	-	-	-
10.1021/Jp3099768	Zeolite CHA*	14.37	0.0023	14.37	0.0004	100.20	-	-	-
10.1021/Jp3099768	Zeolite CHA*	248.67	0.0000	248.67	0.0000	96.28	-	-	-
10.1021/Jp3099768	Zeolite DDR*	2.37	0.0144	2.37	0.0017	103.38	-	-	-
10.1021/Jp3099768	Zeolite DDR*	1.46	0.0046	1.46	0.0029	94.07	-	-	-
10.1021/Jp3099768	Zeolite EDI*	5.34	0.0071	5.34	0.0013	98.62	-	-	-
10.1021/Jp3099768	Zeolite EDI*	3.04	0.0025	3.04	0.0023	96.96	-	-	-
10.1021/Jp3099768	Zeolite ERI*	5.37	0.0058	5.37	0.0010	99.01	-	-	-
10.1021/Jp3099768	Zeolite ERI*	43.80	0.0001	43.80	0.0001	97.02	-	-	-
10.1021/Jp3099768	Zeolite FAU*	2149.36	0.0000	2149.36	0.0000	98.67	-	-	-
10.1021/Jp3099768	Zeolite FAU*	203.78	0.0000	203.78	0.0000	91.24	-	-	-
10.1021/Jp3099768	Zeolite FAU*	1.60	0.0014	1.60	0.0016	98.10	-	-	-
10.1021/Jp3099768	Zeolite FER*	2.59	0.0223	2.59	0.0027	103.27	-	-	-
10.1021/Jp3099768	Zeolite FER*	1.79	0.0063	1.79	0.0041	94.04	-	-	-
10.1021/Jp3099768	Zeolite GIS*	80.47	0.0005	80.47	0.0001	103.21	-	-	-
10.1021/Jp3099768	Zeolite GME*	1.85	0.0088	1.85	0.0028	88.98	-	-	-
10.1021/Jp3099768	Zeolite ISV*	29.40	0.0010	29.40	0.0001	103.25	-	-	-
10.1021/Jp3099768	Zeolite ISV*	15.55	0.0010	15.55	0.0002	90.54	-	-	-

Table E.1 continued from previous page

DOI	Adsorbent	q_{sb,CO_2} [mol/kg]	$b_{CO_2,298}$ [m^3/mol]	q_{sb,N_2} [mol/kg]	$b_{N_2,298}$ [m^3/mol]	r_{max} [-]	$En_{min,BAAM}$ [kWh_e/tonne CO_2 cap.]	$En_{min,scaled}$ [kWh_e/tonne CO_2 cap.]	WC_{CO_2} [mol CO_2/m^3]
10.1021/Jp3099768	Zeolite ISV*	104.17	0.0000	104.17	0.0000	98.49	-	-	-
10.1021/Jp3099768	Zeolite LTA*	663.24	0.0000	663.24	0.0000	92.62	-	-	-
10.1021/Jp3099768	Zeolite LTA*	116.20	0.0000	116.20	0.0000	98.47	-	-	-
10.1021/Jp3099768	Zeolite LTL*	6.98	0.0032	6.98	0.0003	107.00	-	-	-
10.1021/Jp3099768	Zeolite LTL*	4.93	0.0023	4.93	0.0004	96.34	-	-	-
10.1021/Jp3099768	Zeolite LTL*	0.79	0.0031	0.79	0.0030	97.03	-	-	-
10.1021/Jp3099768	Zeolite MER*	2.56	0.0058	2.56	0.0019	89.40	-	-	-
10.1021/Jp3099768	Zeolite MFI*	3.34	0.0133	3.34	0.0014	106.07	-	-	-
10.1021/Jp3099768	Zeolite MFI*	2.24	0.0038	2.24	0.0022	93.33	-	-	-
10.1021/Jp3099768	Zeolite MOR*	2.92	0.0182	2.92	0.0020	105.16	-	-	-
10.1021/Jp3099768	Zeolite MOR*	1.76	0.0062	1.76	0.0035	92.96	-	-	-
10.1021/Jp3099768	Zeolite MTT*	1.93	0.0207	1.93	0.0019	107.81	-	-	-
10.1021/Jp3099768	Zeolite MTT*	1.11	0.0073	1.11	0.0035	91.65	-	-	-
10.1021/Jp3099768	Zeolite MWW*	3.35	0.0124	3.35	0.0017	101.71	-	-	-
10.1021/Jp3099768	Zeolite MWW*	4.55	0.0017	4.55	0.0012	95.57	-	-	-
10.1021/Jp3099768	Zeolite RHO*	10.17	0.0043	10.17	0.0005	103.89	-	-	-
10.1021/Jp3099768	Zeolite RHO*	461.19	0.0000	461.19	0.0000	94.96	-	-	-
10.1021/La302537d	Cu-TDPAT*	5.87	0.0215	5.87	0.0019	110.57	-	-	-
10.1021/La302537d	Cu-TDPAT*	8.95	0.0127	8.95	0.0012	109.60	-	-	-
10.1021/La302537d	Cu-TDPAT*	2.91	0.0424	2.91	0.0040	107.82	-	-	-
10.1021/La302537d	Cu-TDPAT*	3.30	0.0332	3.30	0.0035	106.33	-	-	-
10.1021/La302537d	Cu-TDPAT*	6.53	0.0181	6.53	0.0017	109.75	-	-	-

Table E.1 continued from previous page

DOI	Adsorbent	q_{sb,CO_2} [mol/kg]	$b_{CO_2,298}$ [m^3/mol]	q_{sb,N_2} [mol/kg]	$b_{N_2,298}$ [m^3/mol]	r_{max} [-]	$En_{min,BAAM}$ [kWh_e/tonne CO_2 cap.]	$En_{min,scaled}$ [kWh_e/tonne CO_2 cap.]	WC_{CO_2} [mol CO_2/m^3]
10.1021/La302537d	Cu-TDPAT*	1.98	0.0438	1.98	0.0062	99.62	-	-	-
10.1021/La302537d	Cu-TDPAT*	3.53	0.0291	3.53	0.0032	105.45	-	-	-
10.1021/La302537d	Cu-TDPAT*	16.10	0.0054	16.10	0.0007	105.22	-	-	-
10.1039/C2cc35691k	ZIF-95*	2.68	0.0058	2.68	0.0009	99.27	-	-	-
10.1039/C3ra44250k	CuBTC	6.36	0.4448	6.36	0.0260	101.78	-	-	-
10.1039/C4dt02300e	MOF-205	21.87	0.0008	21.87	0.0002	94.55	-	-	-
10.1039/C4dt02300e	MOF-205-OBn	612.98	0.0000	612.98	0.0000	98.50	-	-	-
10.1039/C4ee01009d	ZIF-8	1088.79	0.0000	1088.79	0.0000	97.94	-	-	-
10.1039/C4ee01009d	ZIF-8	15.16	0.0012	15.16	0.0002	96.77	-	-	-
10.1039/C4ee01009d	ZIF-8	6.54	0.0035	6.54	0.0006	99.41	-	-	-
10.1039/C4ee01009d	ZIF-8	4.15	0.0076	4.15	0.0009	104.20	-	-	-
10.1039/C4ee01009d	ZIF-8	4.12	0.0087	4.12	0.0009	106.44	-	-	-
10.1080/08927022.2011.583648	ZIF-79*	4.63	0.0202	4.63	0.0021	107.32	-	-	-

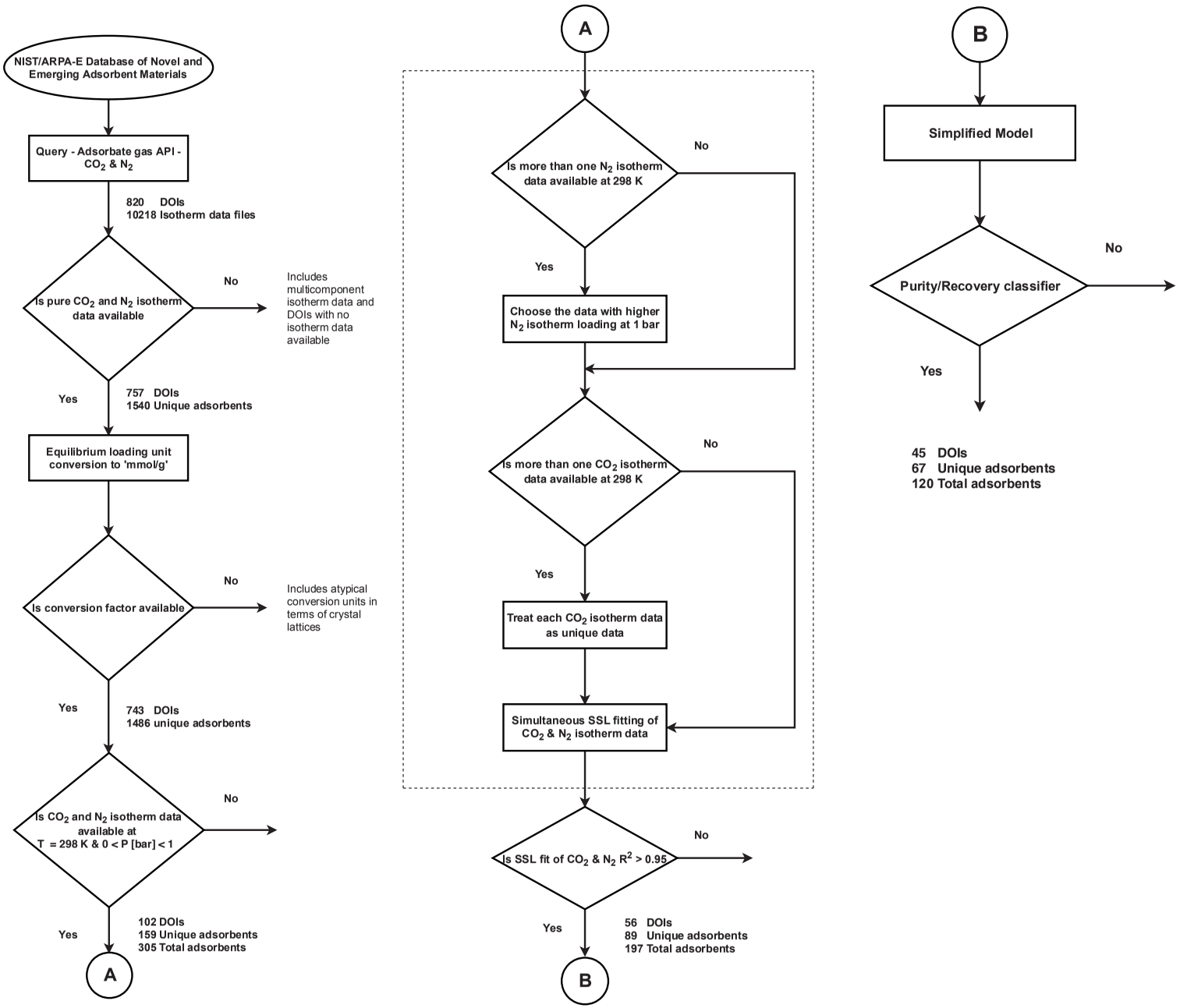

Figure E.1: Flowchart for filtering adsorbents from NIS/ARPA-E database of novel and emerging adsorbent materials.

Appendix F

Fitting parameters - CCMDB

Table F.1: Pure component single-site Langmuir (SSL) fitting parameters of the hMOFs chosen for the detailed model optimization studies.

FrameWork Name	Particle density [kg/m^3]	q_{sb,CO_2} [mol/kg]	b_{0,CO_2} [m^3/mol]	$\Delta U_{b,CO_2}$ [kJ/mol]	q_{sb,N_2} [mol/kg]	b_{0,N_2} [m^3/mol]	$\Delta U_{b,N_2}$ [kJ/mol]
h8297545	1620.84	4.79	2.31×10^{-08}	38.69	4.79	1.24×10^{-05}	8.74
h8329775	1091.98	1.14	1.35×10^{-08}	38.37	11.43	6.92×10^{-06}	7.68
h8180594	1512.96	6.91	1.04×10^{-08}	38.93	6.91	1.07×10^{-05}	6.45
h8071971	1850.19	1.83	3.33×10^{-07}	30.31	1.83	3.90×10^{-06}	12.56
h8274646	1372.10	8.98	3.08×10^{-08}	30.33	8.98	8.36×10^{-06}	6.99
h8186387	2129.10	2.47	1.07×10^{-06}	23.57	2.47	6.87×10^{-06}	10.71
h8081405	1625.26	6.21	5.31×10^{-07}	20.71	6.21	9.26×10^{-06}	6.90

Appendix G

Top 50 materials from Screening of the CCMDB

Table G.1: List of top 50 materials from screening of CCMDB along with their selectivities and performance indicators from BAAM.

h-ZEO	Selectivity [-]	$r_{\max}$ [-]	$En_{\min,\text{scaled}}$ [kWh_e/tonne CO_2 cap.]	WC_{CO_2} [mol CO_2/m^3]
h8297545	904.54	129.05	143.32	1057.11
h8329775	464.25	128.86	143.33	1370.62
h8180594	477.84	128.84	143.37	1131.31
h8116694	360.28	128.67	143.43	1002.03
h8061849	1797.53	129.01	143.59	572.62
h8326012	668.75	128.78	143.60	621.81
h8210285	493.16	128.78	143.76	917.78
h8287207	328.55	128.65	143.78	1305.53
h8325732	429.47	128.78	143.78	1294.35
h8327293	329.08	128.64	143.78	1281.41
h8177168	2291.24	128.97	143.79	484.24
h8052324	964.14	128.78	143.80	487.96
h8313216	522.33	128.70	143.80	659.94
h8316044	386.14	128.73	143.81	1294.58
h8048587	1231.51	128.88	143.81	525.94
h8214739	554.10	128.87	143.83	1144.29
h8301782	638.66	128.91	143.84	1105.17
h8066467	1154.02	128.94	143.84	600.09
h8297227	290.86	128.53	143.86	1046.04
h8292301	429.09	128.73	143.86	1012.71

Table G.1 continued from previous page

h-ZEO	Selectivity [-]	$r_{\max}$ [-]	$En_{\min,\text{scaled}}$ [kWh_e/tonne CO_2 cap.]	WC_{CO_2} [mol CO_2/m^3]
h8264123	824.82	128.58	143.88	401.42
h8126966	3141.31	129.11	143.88	570.46
h8170702	1129.50	128.69	143.89	411.10
h8044927	3200.46	128.96	143.89	441.98
h8210664	344.48	128.59	143.91	916.03
h8167200	602.85	128.70	143.91	581.31
h8301801	312.11	128.56	143.92	1018.32
h8330331	278.18	128.47	143.92	963.34
h8210793	540.31	128.83	143.93	1010.07
h8297090	820.44	128.94	143.93	838.02
h8269713	361.54	128.68	143.94	1239.23
h8278741	305.59	128.51	143.94	901.44
h8266001	304.70	128.49	143.95	845.26
h8288649	355.19	128.60	143.95	913.26
h8320223	314.34	128.47	143.96	757.22
h8307769	318.91	128.57	143.97	1023.79
h8301774	290.39	128.48	143.97	921.28
h8181466	1041.08	128.76	143.98	463.41
h8319074	305.63	128.55	143.98	1092.13
h8190460	2378.21	128.74	143.99	354.05
h8288827	409.21	128.65	144.01	840.28
h8306748	590.94	128.85	144.01	1012.71
h8314044	349.70	128.66	144.01	1293.07
h8293319	433.48	128.73	144.01	1042.92
h8251761	632.74	128.87	144.02	947.43
h8116643	1445.27	128.98	144.03	584.32
h8256586	294.78	128.51	144.03	1042.65
h8059476	974.09	128.86	144.03	572.80
h8274216	349.61	128.61	144.03	1024.35
h8299419	278.76	128.47	144.03	1015.47